Composition engineering of lead-free double perovskite nanocrystals for self-powered photodiodes

(セルフパワーフォトダイオード創製を指向した非鉛系ダブルペロブスカイトナノ粒子の化学組成工学)

Xiaoyu HUANG
Graduate School of Chemical Sciences and Engineering
Hokkaido University

2023

Content

Abstract

Lead-free double perovskite nanocrystals (LDP NCs) are promising materials as an alternative to lead-based perovskite nanocrystals to solve the problem of toxicity and instability. Specifically, replacing two Pb^{2+} ions with a combination of monovalent and trivalent cations could be a solution for forming three-dimensional (3D) perovskite structures, whose chemical formula is $A_2B(I)B(III)X_6$, which is called double-perovskite structure. LDP NCs have excellent properties such as good stability, long carrier lifetime, long photoluminescence lifetimes, high photoluminescence quantum yield and solution-processability. Therefore, LDP NCs are considered to be promising materials for optoelectronic applications including photodetector, photocatalysts, light-emitting diodes and solar cells.

$Cs_2AgB'X_6$ (B' = In or Bi, X = Cl or Br) has the potential to be applied in optoelectronic devices. While it owns a high absorption coefficient, good stability and low toxicity, there is still a challenge in improving its performance to reach or exceed that of lead-based perovskites. For example, the defects introduced by indium can create trap states in the bandgap of $Cs_2AgInCl_6$ thus affecting the material properties. Therefore, the thesis focuses on the composition tuning of LDP NCs for photodiode application by B-site doping strategies as well as the bandgap engineering by X-site anion composition tuning in LDP NCs to realize efficient wavelength-selective photodiodes.

In Chapter 1, a general background about lead-free double perovskites and a simple overview of ultraviolet photodiodes are introduced. In particular, the process and purpose of the research which lead to the conception of the research topic were clarified.

In Chapter 2, Na-alloyment and Bi-doping were employed in improving the optical properties of $Cs_2AgInCl_6$ NCs. We synthesized $Cs_2Ag_{0.65}Na_{0.35}InCl_6$ NCs doped with bismuth (Bi^{3+}) ions and investigated their photophysical properties to reveal the role of the dopant on the enhanced photoemission properties. Specifically, it was found that the

photoluminescence quantum yield (PL QY) increased up to 33.2% by 2% Bi-doping. The optical bandgap of the NCs decreased from 3.47 eV to 3.41 eV as the amount of the dopant increased from 2% to 15%. To find out the effect of Bi-doping, the temperature-dependent PL properties of the undoped and doped NCs were investigated by utilizing steady-state and time-resolved PL spectroscopy. With increasing the temperature from 20 K to 300 K, the PL intensities of the doped NCs decreased slower than the undoped ones. The correlated average PL lifetimes of both the bismuth-doped and undoped NCs decreased with increasing temperature. The experimental results revealed that all the NC samples showed thermal quenching with the temperature increasing, and the PL quenching was suppressed in bismuth-doped NCs.

In Chapter 3, we first demonstrated the highly responsive lead-free perovskite photodiode based on $Cs_2Ag_{0.35}Na_{0.65}InCl_6$ nanocrystals. The composition tuning strategy is introduced to enhance the device performance of photodiodes. Employed with a device structure composed of ZnO: Al electron-transport layer and Poly[(9,9-dioctylfluorenyl-2,7-diyl)-co-(4,4'-(N-(4-sec-butylphenyl)diphenylamine)] (TFB) hole transport layer, lead-free perovskite nanocrystal photodiodes exhibit a high responsivity of 3.03 A/W and specific detectivity of 1.29 X 10^{11} Jones under the illumination of a 340 nm light source. Moreover, the ultraviolet (UV) photodiodes show good performance under the self-powered mode, which exhibits a responsivity of 0.07 A/W and specific detectivity of 5.04 x 10^{10} Jones. Our work verifies the great potential of the $Cs_2Ag_{0.35}Na_{0.65}InCl_6$ nanocrystals in the application of environmentally friendly and high-performance UV photodiodes.

In Chapter 4, we studied on Cs_2AgBiX_6 (X = Cl or Br) NCs, which replaces In^{3+} by Bi^{3+} to avoid the generation of indium-caused defects and obtain strong absorption for the photodiode application. The band gap engineering was conducted through the composition tuning from $Cs_2AgBiCl_6$ to $Cs_2AgBiBr_6$. We fabricated lead-free double perovskite photodiodes with wavelength-selective properties response to UV-Visible range. Specifically, the $Cs_2AgBiBr_6$-based photodiode exhibits a characteristic detection

peak at 340 nm with a responsivity of 3.21 mA/W, a specific detectivity up to 8.91 X 10^{10} Jones and a fast response speed with rise/fall time of 30/35 ms. The excellent performance of self-driven photodiodes lights up the prospect of lead-free double perovskite nanocrystals in highly efficient optoelectronic devices without external power sources.

In Chapter 5, we clarify the conclusions and propose the outlook on the efficacy and future potential of the lead-free double perovskite nanocrystals.

Chapter 1 Introduction

1.1 Ultraviolet (UV) photodetectors

With the rapid development of the Internet of Things, it has become increasingly important to develop smart, highly sensitive, sustainable, environmental-friendly, energy-saving, and ultra-small and multifunctional optoelectronic devices and sensors.[1–5] Photodetector, as an essential type among various sensors, is used to convert incident light signals into electrical signals and has been widely concerned owing to its wide range of applications. In general, different types of photodetectors are used for sensing optic signals at wavelengths in the ultraviolet (UV), visible, and infrared (IR) regions.

Among the full spectrum band, UV radiation, as a key component of electromagnetic radiation, has a profound impact on both organic life and the existence of inorganic matter.[6–8] In addition to the natural source of solar radiation, UV radiation can be artificially produced in a variety of ways, including phototherapy, plasma torches, UV light-emitting diodes, welding arcs, and xenon-mercury arc lamps. The ISO standard designates the UV band as the spectral region between 10 nm and 400 nm. It can be divided into three primary categories: UVC (100~280 nm), UVB (280~320 nm), and UVA (315~400 nm), as shown in Figure 1.1.[9–13]

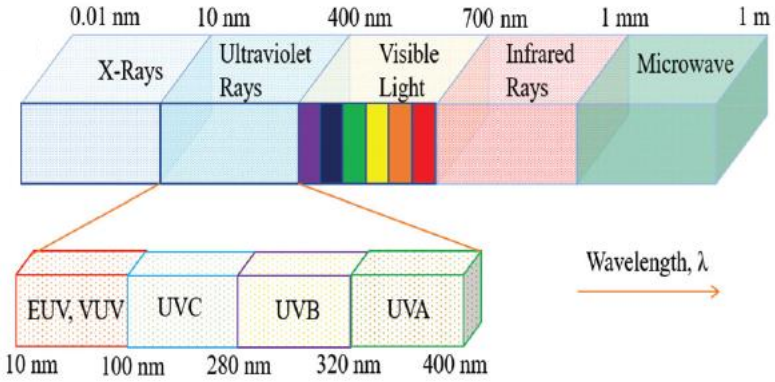

Figure 1.1 Spectral distribution with the classification of UV region.[14]

Depending on the level of exposure, UV radiation can either be beneficial to human

survival and development or have catastrophic effects. For example, the synthesis of vitamin D, which promotes bone growth and prevents rickets, requires reasonable exposure of human skin to UV light, whether from natural or artificial sources. On the other hand, excessive exposure to UV radiation can speed up the aging process and can lead to deadly skin cancer.[8] The ozone layer in the stratosphere acts as a filter to block dangerous UV radiation from the sun, protecting life on earth from potentially harmful exposure. Tragically, changes in the stratospheric ozone layer over the past four decades have affected the solar UV radiation regime at the earth's surface, which has negatively impacted ecosystem services, food and water security, and human health. [15] The harmful effects of changes in UV exposure caused by ongoing climate change will soon become apparent.

Hence, monitoring of UV radiation is necessary and desirable, which can be achieved by using high-performance UV photodetectors to convert the light signal into a measurable electrical quantity. As shown in Figure 1.2, ozone layer monitoring, secure satellite communication, oil spill monitoring, hydrogen flame detection, and missile early warning are just a few of the numerous other uses for UV photodetectors.[16,17] UV photodetectors also have imaging array, wildfire prevention and many other functional uses.[18–22]

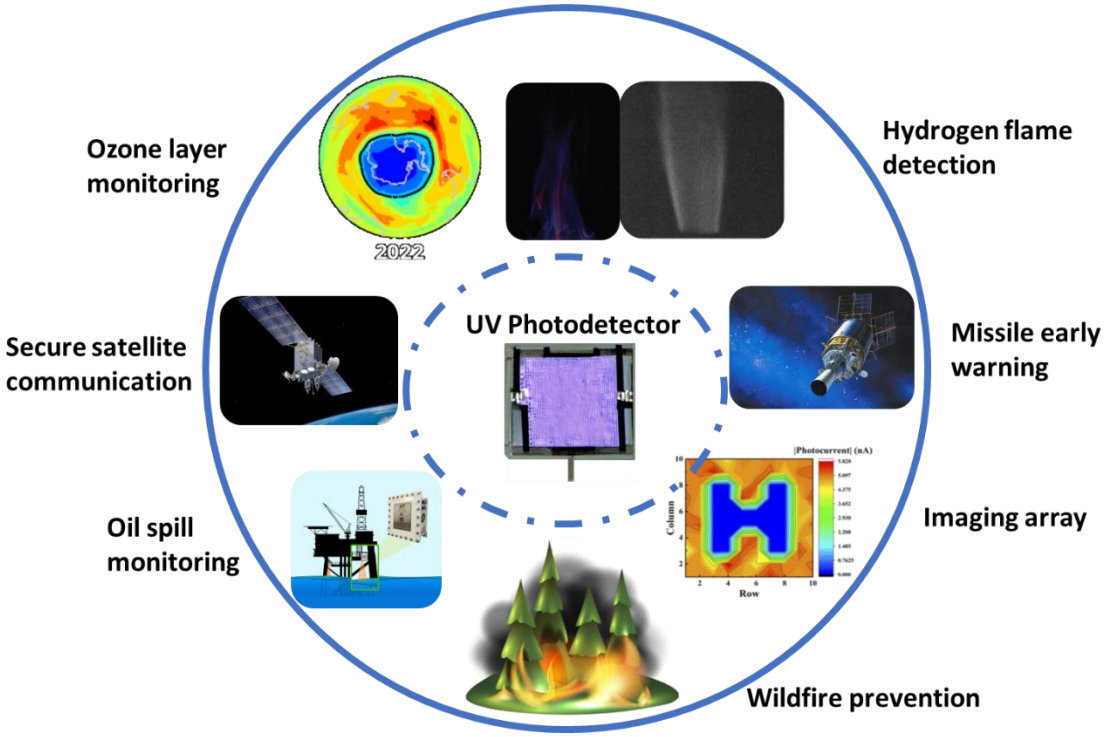

Figure 1.2 The applications of UV photodetectors.

1.1.1 The categories of photodetectors

Generally, photodetectors are categorized into three primary types, photoconductors, phototransistors and photodiodes based on their device architectures, as shown in Figure 1.3.[23] In the case of photoconductors, as shown in Figure 1.3(a), the photo-active layer acts as the channel between two metal electrodes, constructing a simple photon-electron conversion system that works by modulating the conductivity of active material under the illumination of the light source. In another word, the working mechanism of the photoconductor is the photoconductive effect, in which the photo-generated carriers are separated within the active layer, transported between two electrodes, and collected by the electrodes under the additional bias voltage.[24,25] As Figure 1.3(b) depicted, phototransistor is three-terminal device, compared to photoconductor, the gate electrode and dielectric layer are added to reduce the noise current, which amplify the photocurrent signal and enhance the detective performance. In this case, the performance of phototransistor can be improved not only by adjusting the source-drain voltage and light

irradiation intensity, but also by changing the gate voltage.[23,26] The working principle of photodiode is similar to that of solar cell.[27,28] Photodiodes detect light by increasing a reverse current under a reverse operating voltage. Because of the short carrier transport distance, the response time does not rely on carrier compounds, which is beneficial to generate faster response than photoconductor.[29] On the other hand, photodiode is largely dependent on the built-in potential in various type of photo-junction, which is beneficial to extract photo-generated carriers. Generally, additional reverse bias is applied to improve the charge collection efficiency.[30] Compared with photoconductors and phototransistors, photodiodes exhibit low driving voltage, low dark current, fast response and high carrier separation efficiency under illumination, which is highly potential for the application of self-powered photodetector.

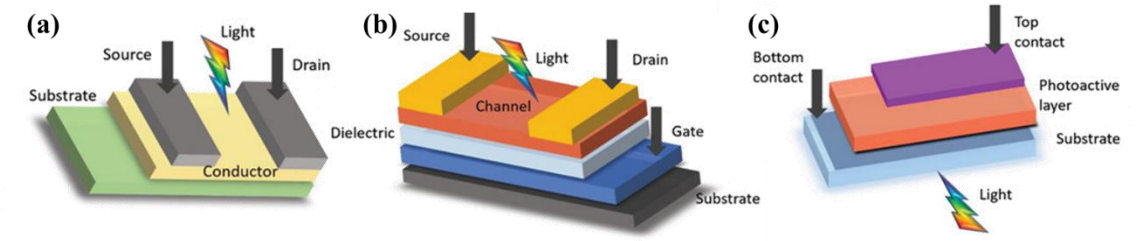

Figure 1.3 Schematic of photodetectors with different structures. They represent (a) photoconductors, (b) phototransistors, and (c) photodiodes.[23] Copyright 2021, Wiley-VCH.

1.1.2 Self-powered UV Photodiodes (PDs)

Conventional UV photodiodes (PDs) often require an external bias to be supplied for the separation of photogenerated charge carriers (electron-hole pairs), which consumes energy and increases the device size, limiting both downsizing and long-term stand-alone deployment in large-scale arrays.[22,31,32] Monitoring, changing, and recycling batteries would be a difficult and occasionally impossible task for the numerous batteries that are dispersed over the planet to power the sensors, each of which has a finite lifespan.[33] Also, the external source's (the battery's) materials could pose risks to the environment and public health.[8]

Therefore, it is strongly advised that PDs be self-powered in order to avoid the need for an external battery. This not only improves adaptability, even under harsh circumstances, but also greatly decreases size and weight. Based on the photovoltaic effect that results from the charge separation features at the interface, self-powered UV PDs can be categorized into three groups: p-n junctions (homojunction or heterojunction), Schottky junctions, and photoelectrochemical (PEC) cells. Figure 1.4 depicts typical device structure and working mechanism of self-powered PDs.

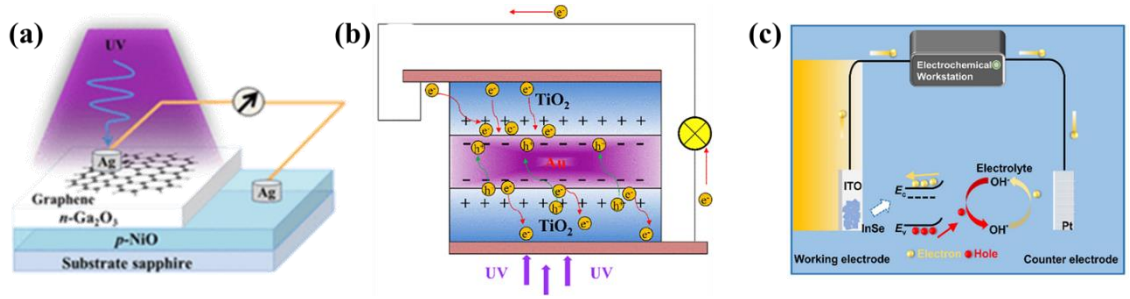

Figure 1.4 Typical device of different type of self-powered UV PDs. (a) p-n junction (or p-i-n junction, n-i-p junction),[34] (b) Schottky junction,[35] and (c) photoelectrochemical cells.[36]

Figure 1.4(a) displays the device architecture of the p-n junction photodetector,[34] where the generated built-in electric field at the semiconductor/semiconductor interface boost the overall photoconductivity through the separation of photo-generated electron-hole pairs. In the case of p-n junction, the photo-generated electrons are driven to the n-type region, while holes transport to the p-type region under the driven of built-in electric field.[37] Take the device depicted in Figure 1.4(b) as an example, Schottky junctions have two opposite directional inner electric fields. The electron-hole pairs are generated in the bottom depletion zone when light irradiated from the bottom electrode, then the carriers transport from central metal to semiconductor. Holes accumulate in the upper region of TiO_2 at the interface with Au, resulting in an electropositive region that easily attracts electrons. Then, electrons move from bottom to top through an external circuit and then injected into the TiO_2 on the top side of the device. Finally, these electrons will transfer to the upper depletion region to neutralize the positive holes.[35] PEC photodetectors have

become popular recently due to the simple fabrication processes and low driving voltage.[38] And they could realize self-powered function via the interfacial electric field between active material and electrolyte.[9] As shown in Figure 1.4(c), the difference between work function and the redox potential of electrolyte contribute to the built-in electric field at the interface.[36] Among various type of photodiodes, the separation process of electron-hole pairs is fast in heterojunctions (p-i-n or n-i-p) and thus heterojunction-type photodiode has a great advantage in terms of high-speed response.

1.2 Metal halide perovskites act as photoactive layer in photodiode

1.2.1 Perovskites

Perovskite originates from a calcium titanium oxide mineral $CaTiO_3$, which was discovered by a German mineralogist Gustav Rose in 1839 and named after Russian mineralogist Count Lev Alekseyevich von Perovski. As with many minerals, perovskite has given its name to a family of compounds that have a general formula of ABX_3 called perovskites, and their crystal structures are as shown in Figure 1.5.

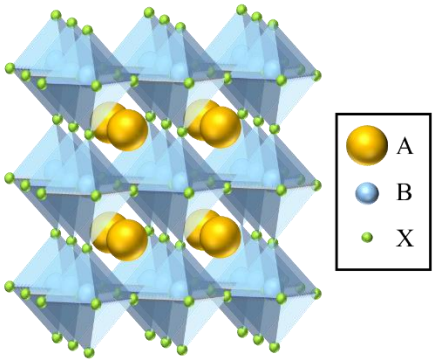

Figure 1.5 Crystal structure of perovskite

Normally, perovskites satisfy the following three requirements: (a). the molar ratio of the three elements A, B, and X is 1:1:3; (b) BX6 composed of B ions and X ions is octahedral or twisted octahedral; (c) The [BX6] octahedra share the common corner forming three-dimensional network structure. Regarding the element for different sites, A site is usually alkali metal ions which has a large ionic radius, playing the role of fixing

the perovskite structure; B site is the transition metal ions which has a small ionic radius and various valent state and decide the main properties of perovskite materials.[39] With the development of perovskites, those structures derived from perovskite are called perovskite-variants. The perovskite structure has two main characteristics, one is high symmetry, The cubic phase with high symmetry is the basis of its excellent properties. Due to the excellent properties of perovskite materials such as tunable optical bandgap, high carrier mobility, high absorption coefficient, long carrier lifetime, and long diffusion length, they have the potential in solar cells, light-emitting diodes, laser, and photocatalytic applications.

1.2.2 The development of lead halide perovskite materials

Lead halide perovskite (LHP) has been widely concentrated because of the excellent optoelectronic properties.[40] The power conversion efficiency (PCE) of solar cells based on LHP has been shot up from 3.8% in 2009 to 25.8% in 2021.[41] On the luminescent properties, LHP is certified of high photoluminescence quantum yield (PLQY), narrow full width of half maximum (FWHM), tunable spectrum and easily synthesized.[42] Recently, organic and inorganic LHP quantum dots (QDs) are partially commercialized in display technology, such as smartphone based on organic light-emitting diodes (OLED) and television based on quantum dot light-emitting diodes (QLED). LHP QDs are also promising in single-photon sources.[43]

1.2.3 A simple synthetic nanocrystal

LHP has a relatively low ionic charge and large atom distance, which results in the obvious tendency of thermal decomposition, and the melting point of LHP is lower than that of oxide perovskites.[44] The melting point of both $FAPbX_3$ and $MAPbX_3$ is lower than 300 ºC, while the melting point of $CsPbX_3$ is around 400-500 ºC. Compared with metal sulfide, $APbX_3$ has stronger covalent bond and crystal lattice.[45] It is applicable for preparation, synthesis, processing and surface treatment of $APbX_3$ NCs. The synthetic

temperature of traditional II-VI compound is often high, and also the reaction time is long; while the LHP is able to form within several seconds even though at room temperature.[42,46] Hot-injection method and anti-solvent method are the common methods for the synthesis of $APbX_3$ NCs.[47] Assisted hot-injection and ligand-assisted anti-solvent reprecipitate are applicable for the synthesis of $CsPbX_3$ NCs. In the ligand-assisted reprecipitate synthesis of $MAPbX_3$ and $FAPbX_3$ NCs, A^+, Pb^{2+} and X^- ions in polar solvent rapidly induce the crystal precipitate by mixing the non-polar solvents.[46] The shape of $APbX_3$ is controlled by adjusting the parameters of two synthetic methods, all of the cubic nanocrystals, quantum dots, nanowires and nanosheets could be obtained.[48–51]

However, the obstacle of $APbX_3$ is instability. No matter which method used for synthesis, or which morphology it is, long-term stability is hard to achieve. The encapsulation technique has been studied to enhance the stability of $APbX_3$ NCs, but the improvement is not satisfactory.[52] The inorganic passivation layer used for covering the surface of LHP NCS has been studied, such as SiO_2, TiO_2, and Al_2O_3, although the stability of $APbX_3$ NCs has been enhanced to some extent, the morphology changing and decomposition are still not stopping.[53–55]

1.2.4 Defect tolerance

The popular LHP materials is owing to their unique optical properties. The electronic properties of LHP making a high defect tolerance of it, for example, even though the LHP has high density of point defects, the photovoltaic device based on LHP with high efficiency is still easily fabricated. The high defect tolerance makes LHP quite different from other traditional semiconductor materials such as Si, CdTe and GaAs.

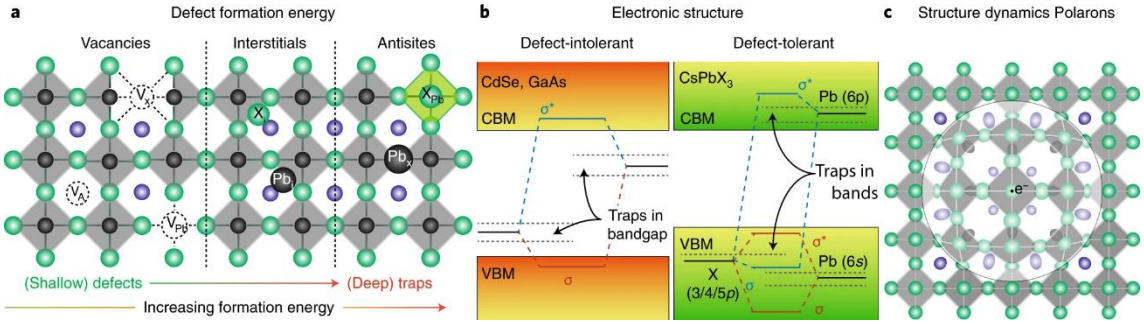

Figure 1.6 Defect tolerance mechanism in LHPs.[56] (a) The relationship between various defect types and defect formation energy in LHPs. (b) The electronic band structure of traditional semiconductors and LHPs. σ and σ* represent bonding and antibonding orbitals, respectively. (c) Local structural deformation of Pb-Br framework and the polaron formation.

Firstly, among the point defects, the formation energy of vacancies is relatively low, therefore, only vacancy is observed in LHPs.[56] As shown in Figure 1.6, because of the energy of ions in perovskite crystals is hard to mismatched, the interstitials and the antisites are difficult to form, therefore there is almost impossible to form interstitials and antisites at deep trap state.[57,58] Secondly, vacancies in LHPs have their unique irrelativity, which is anti-bonding property. As Figure 1.6 shows, the band gap of LHPs forms at two anti-bonding orbitals, while the shallow trap formed by point defect is completely confined in the valence band and conduction band, therefore the vacancies have no influence in the radiative recombination and other optical properties of LHPs. It can also explain the reason why LHP QDs perform very high PLQY without any surface passivation and modification.[59] Thirdly, the crystal state of LHPs is similar with liquid because of the soft lattice, and this characteristic protects LHPs from trapping and dispersion.[60] Furthermore, the strong structural dynamics of the PbX lattice at room temperature led to the coupling of electron and hole and the accompanying displacement of ions, implying the promotion of polaron formation. These polarons can shield the Coulomb potential and reduce trap and carrier scattering, while also reducing the interaction between defects and optical phonons.[56]

1.2.5 Unstable structure and corresponding solutions

How to keep the structural and optical stabilities is the first challenge for LHPs. As we mentioned before, LHP NCs are easily prepared, which means they are also easy to decompose. Therefore, keeping the integrity of the LHPs crystal structure during the centrifugation, the purification and treatment process is a crucial problem. At present, then main synthetic method for LHP NCs is dependent on the ligand-assisted process,

which achieve the combination of nanocrystals by attaching single anchor groups or long alkyl chain ligands on the carboxylic acid or phosphate ligands on the surface of metal atoms.[61,62] The basic coordination process in NCs is that amino groups replace surface A-site cations, while carboxyl groups play the role of surface anions.[62] These ligands usually undergo desorption and absorption rapidly. That results in loosen combination between ligands, also the structure of quantum dots is fragile, and will cause the difficulty of separation and purification in quantum dots. The surface ligands have a lot of anchor groups, which introduces other ions or molecules. Each molecule might have influence on NCs which surrounding by large number of groups and long-chain molecule ligands. The low ionic bonding makes LHP soluble in almost all organic polar solvents, which actually illustrates on the other hand that exposure of LHP to polar solvents leads to its decomposition. [56] The reason for the instability of LHP material is that polar molecules such as oxygen and water molecules cause the material to decompose.

The instability of LHP NCs is always an obstacle which is difficult to overcome. One of the widely committed solutions is that covering LHP NCs inside lazy shell, such as SiO_2, TiO_2 or Al_2O_3 which can protect LHP from those materials owning polarity and solubility.[52–55] SiO_2 is a typical shell, which improves the stability of LHP NCs in water. Recently, melting process was studied for enhancing the luminous stability of LHP crystals by growing in glass. This nanocrystal is covered by amorphous glass and it is chemical stable, and is also protected from water and oxygen. The product can be applied in lightening or phosphors.[63]

1.2.6 The toxicity of lead element and the exploration in lead-free perovskites

The existence of lead in LHP raises an obvious concern about the introduction of lead in consumer electronic devices. The use of heavy metal materials is limited by EU RoHS.[56] The exploration of environmentally friendly candidates which have extraordinary chemical properties is our concern. Basically, defect-tolerant

semiconductors are those semiconductors whose valence bands and conduction bands are formed by the hybridization of s and p orbitals. According to this principle, perovskites based on Sn^{2+} and Ge^{2+} which are closely similar to LHPs do perform bright emission, however, they are quite unstable, even though a trace amount of oxygen could result in the PL quenching. On the other hand, LHPs analogs based on Tin are not an ideal candidate because of their toxicity.[64] The researchers in the solar cells area make a huge effort in exploring lead-free LHP materials, especially replacing Pb^{2+} by Bi^{3+}.[65] However, the ternary halides have a big difference with LHPs in structure. For example, $Cs_3B_2X_9$ ($B=Sb^{3+}$, Bi^{3+}, In^{3+}) has indirect bandgap and form 0D or 2D net structure.[66] So far, these 2D phases or 0D phase doesn't show highly efficient PL at room temperature. To keep the 3D inter-connection between octahedrons, $A_2B^+B^{3+}X_6$ double perovskites were studied, such as $Cs_2AgBiCl_6$ and $Cs_2AgBiBr_6$.[67,68] These compounds haven't perform the comparative photophysical properties with LHPs, and they usually have indirect bandgap, therefore are inappropriate for light-emitting materials.

1.3 The design and crystal structure of lead-free halide perovskites

There are two common pathways to realize the lead-free halide perovskite structures:[69] (a) Replace Pb^{2+} by one divalent cation, such as Ge^{2+}, Sn^{2+} in 14 group, alkaline earth metal elements (Mg^{2+}, Ca^{2+}, Sr^{2+}, Ba^{2+}) or transition metal elements (Mn^{2+}, Fe^{2+}, Ni^{2+}, Pd^{2+}, Cu^{2+}, Cd^{2+}); (b) Transition metal (Au^{2+}), main group element (Tl^{3+}, Sb^{3+}, Bi^{3+}, Te^{3+}), lanthanides (La, Ce, Pr, Nd, Sm, Eu, Gd, Dy, Er, Tm, Lu) and actinides (Pu, Am, Bk) hybrid with non-covalent metal cations used for replacing Pb^{2+}. These cations don't show charge neutral in the ABX_3 structure, therefore, charge balance is usually achieved by mixing valence substitution. The possible way is $A_3B_2X_9$ ($B= Sb^{3+}$, Bi^{3+}, In^{3+}),[70,71] which means the mixture of high valence metal cations and vacancy makes the charge neutral, with the structure change. Another solution is $A_2BB''X_6$ double perovskite structure, one Pb^{2+} is replaced by a monovalent element and a trivalent element.[67,68] Owing to the variety of elements in the periodic table, various lead-free halide perovskites

is produced, as shown in Figure 1.7.[72]

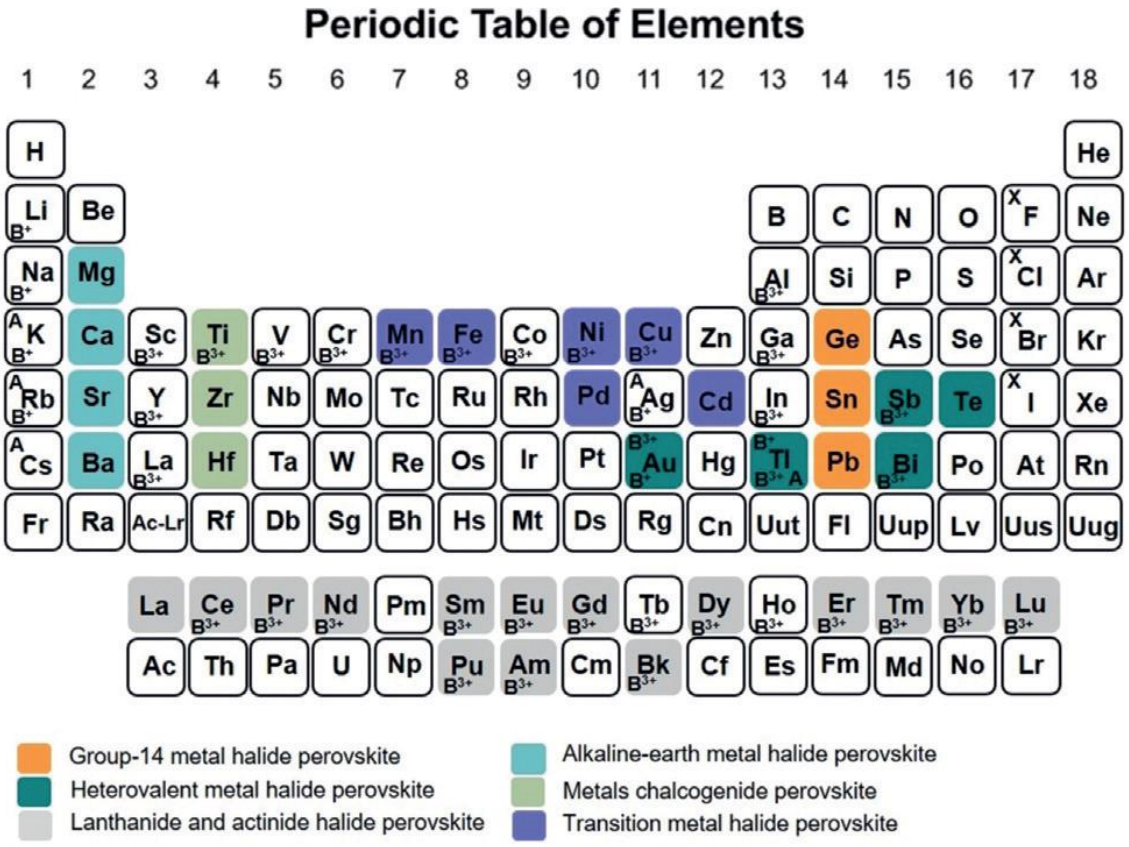

Figure 1.7 Candidates to replace lead in perovskite-type compounds. Reproduced with permission.[65] Candidates for double perovskite $A_2B^+B^{3+}X_6$ have been marked separately. Reproduced with permission.[69]

1.3.1 Lead-free halide double perovskites

As mentioned above, among the candidates of LHPs, on the one hand, ABX_3 (B= Sn^{2+}, Ge^{2+}) has the problem of instability: Sn^{2+} could be easily oxided to Sn^{4+};[72] $CsGeCl_3$ and $CeGeBr_3$ has phase change at room temperature.[73] On the other hand, $A_3B_2X_9$ (B=Sb^{3+}, Bi^{3+}) structure reduces the energy band dispersion compared with LHPs, and increases the effective mass of charge carriers, reducing the carrier mobility.[74]

Three-dimensional structure is important to improve optoelectronic properties. $A_2BB'X_6$ structure is explored which has a standard cubic perovskite structure.[67] So far, Cs_2AgBiX_6 is one of the widely studied double perovskites, the structure is as below,

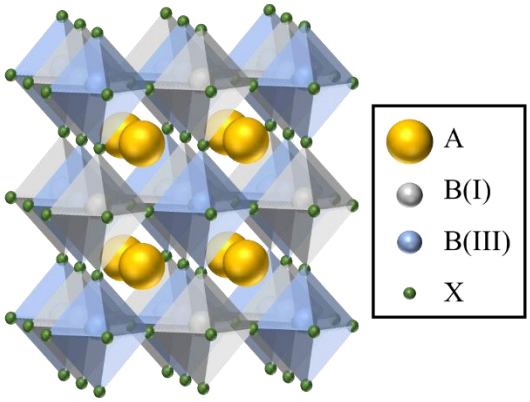

Figure 1.8 Crystal structure of double perovskite

In 3D perovskite structure, Ag^{+} and Bi^{3+} combine with halogen X- forming octahedron, connecting to face-centered cubic structure, the Cs^{+} fill in the space between the octahedrons. $Cs_2AgSbCl_6$, $Cs_2AgSbBr_6$ and $Cs_2AgInCl_6$ double perovskites show similar structure.[75,76]

1.3.2 The optical properties of $Cs_2AgInCl_6$ double perovskites

Metal halide double perovskites are popular owing to the corner-shared octahedron cubic structure which is potential in photovoltaic absorbing materials.[77]

Table 1.1 Bandgap types of possible double perovskite A2B'B''X6 structures[77]

B3+ / B+		Group 1 Sc, Y	Group 13 Al, Ga, In3+, Tl3+	Group 15 Sb3+, Bi3+
Group 1	Na, K, Rb, Cs	Direct (All forbidden)	Direct (All forbidden)	Mostly direct (weak transition)
Group 11	Cu, Ag, Au	Indirect	Direct (Partially forbidden)	Indirect
Group 13	In+, Tl+	Direct (weak transition)	Indirect	Direct (Strong transition)

Table 1.1 shows the possible double perovskite combination and their related bandgap properties. By the simulation of electronic structure and bandgap, three types of double perovskite structures show indirect bandgap. However, the direct bandgap is

preferable for application in solar cells, light-emitting diodes, or photodiodes. On the other hand, strong transition state at band edge is ideal for the solar cell, but In^{+}-based perovskite is unstable because the redox effect. [77]

Interestingly, $Cs_2AgInCl_6$ is a quite stable material which is direct bandgap and partially forbidden according to the calculation of energy band. Its valence band maximum is mainly originated from the hybrid orbital of Ag 4d and Cl 3d, while the conduction band minimum is contributed by the dispersion conduction band from the 5s delocalization, and the energy level of Ag 5s is higher than In 5s. However, limited by the forbidden inter-band transition property, the absorption to phonon which is close to bandgap energy is very weak, resulting in the low photoluminescence quantum yield (less than 1%) of $Cs_2AgInCl_6$.

Doping is an effective strategy that can bring new magnetic, electrical, and optical properties to materials.[78] As mentioned above, $Cs_2AgInCl_6$ double perovskites are quite stable materials, but their optical properties are relatively poor compared with lead-based perovskites. The Ag^{+} and In^{3+} could be easily replaced by other cations owing to the octahedron coordination condition of this structure, that makes $Cs_2AgInCl_6$ to the doping main body of various elements. [79] Doping in $Cs_2AgInCl_6$ would realize the break of transition of forbidden band, the change of bandgap and the enhancement in emission properties.[79–81]

1.4 Advances in photodetectors based of lead-free double perovskite

Wu et al. fabricated ITO/SnO_2/$Cs_2AgBiBr_6$/Au heterojunction device for photodetector application.[82] The self-powered device shows two peaks at 350 nm and 435 nm in responsivity, which is preferable in ultraviolet-A (UVA: 320-400 nm) and deep-blue light detecting. Under the irradiation of 350 nm, the champion device shows a high responsivity of 0.11 A/W and a fast response time of less than 3 ms, which is obviously higher than UV detectors based on other semiconductor oxide heterojunctions. It is noted that the photocurrent shows almost no degradation after more than 6 months without any

encapsulation in air. Therefore, the possibility of lead-free double perovskites in practical applications is expectable. In 2019, Yang et al. developed a solution method to deposit $Cs_2AgBiBr_6$ film with high-quality, large grain sizes (~250 nm), low trap densities, and long carrier lifetimes.[83] The photodiode based on the $Cs_2AgBiBr_6$ film exhibited a high detectivity of 3.29 x 10^{12} Jones, a large linear dynamic range of 193 dB, and a fast response time of 17 ns under the irradiation of AM 1.5. $Cs_2AgInCl_6$ single crystal has been applied in the UV detector in 2018.[84] Luo et al. synthesized high-quality $Cs_2AgInCl_6$ single crystals with low trap density, high on-off ratio (~500), the fast response time of 1 ms, and high specific detectivity of 9.6E11 jones were achieved in Au/$Cs_2AgInCl_6$/Au photodetectors. In a word, photodetectors based on perovskites have high efficiency, high stability, and environmental friendliness, and are potential substitutes for future commercial applications.

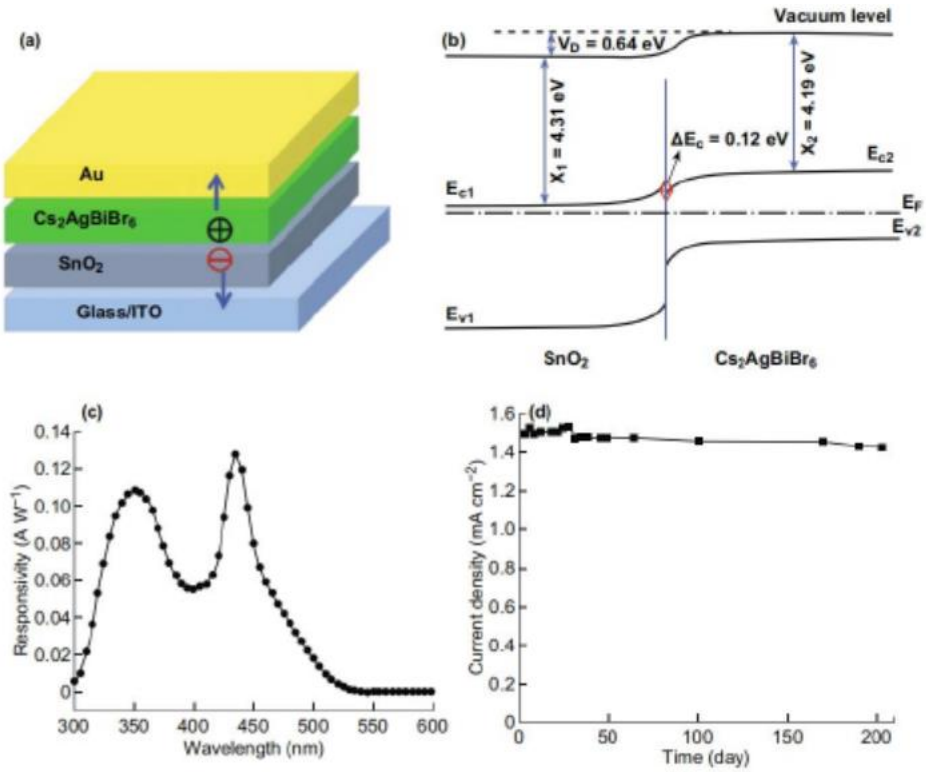

Figure 1.9 (a) Structure of $Cs_2AgBiBr_6$-based photodetector. (b) The energy band structure of $Cs_2AgBiBr_6/SnO_2$ heterojunction is shown. (c) The responsivity of photodetector under zero bias voltage. (d) Long-term stability test of $Cs_2AgBiBr_6$ based photodetector.[82]

Lead-free $Cs_2AgBiCl_6$ double perovskite films with exceptional morphology, highly orientated crystallinity, and an indirect bandgap of 2.41 eV were produced by Wang et al. using successive vapor deposition.[85] To create $Cs_2AgBiCl_6$ double perovskite films, CsCl, $BiCl_3$, and AgCl are vacuum-deposited on the substrates one layer at a time. Figure 1.8(a) provides a schematic representation of the sequential deposition procedure. In the heterojunction UV photodetector, SnO_2 and poly[(9,9-dioctylfluorenyl-2,7-diyl)-co-(4,4′-N)-(4-sec-butylphenyl)]diphenylamine (TFB) were employed as ETL and HTL, respectively. Figure 1.9(b) shows the device setup of the FTO/SnO_2/$Cs_2AgBiCl_6$/TFB/Au photodetector. The excellent wavelength-selectivity in the UV-A region is highlighted by the lead-free double perovskite PD's small responsivity peak, which is centered at 370 nm and has an FWHM of 67 nm (Figure 1.9(c)). The maximum detectivity was calculated to be 1.11 x 10^{12} Jones at 370 nm of incoming light, whereas the peak photoresponsivity was observed to be 9.68 mA/W. There is no energy barrier for carrier collection because the photocurrent rose linearly with the increase in incident light intensity in the 50–2000 $\mu W/cm^2$ range.

In order to enhance the crystalline quality and optoelectronic performance of the double-perovskite film, Yan and colleagues further demonstrated lead-free $Cs_2AgBiBr_6$ double-perovskite films via a one-step spin-coating process.[86] They also modified the surface with an ultrathin atomic-layer-deposited (ALD) metal oxide (MO_x) layer. For the purpose of improving the crystalline quality of the perovskite film, various ALD oxide layers (ALD-Al_2O_3, ALD-TiO_2, and ALD-NiO_x) were utilized. However, ALD being an expensive approach has constraints for the low-cost manufacturing of perovskite PDs. Figure 1.10(e) depicts the schematic illustration of the formation of Bi–O bonds at the interface of ALD-MO_x-modified substrate/$Cs_2AgBiBr_6$ double perovskite films. The bismuth atoms in $Cs_2AgBiBr_6$ lattices create a connection with the oxygen atoms on the surface of oxygen exposed substrates. The schematic configuration of FTO/ALD-MO_x-modified layer/$Cs_2AgBiBr_6$/ETL/Au self-powered PD is shown in Figure 1.10(f). The matching energy band diagram of the heterojunction lead-free perovskite PD is given in

Figure 1.10(g). During light excitation, electron–hole pairs are formed in a photoactive $Cs_2AgBiBr_6$ double perovskite layer further divided by the built-in field, leading the electrons to flow to the Au electrode and the holes to the FTO side. The PD displays good photoresponsivity in the 350–550 nm wavelength range, with the maximum value occurring at 470 nm (Figure 1.10(h)). Figure 1.10(i) displays the dynamic photocurrent response of the PDs with various ALD MO_x layers at 0 V bias with 0.4 mW/cm^2 of laser irradiation. The ALD-NiO_x-equipped device displayed the ideal photocurrent. The device's specific detectivity was measured to be 1.2 x 10^{13} Jones, and its linear dynamic range (LDR) is 165.2 dB.

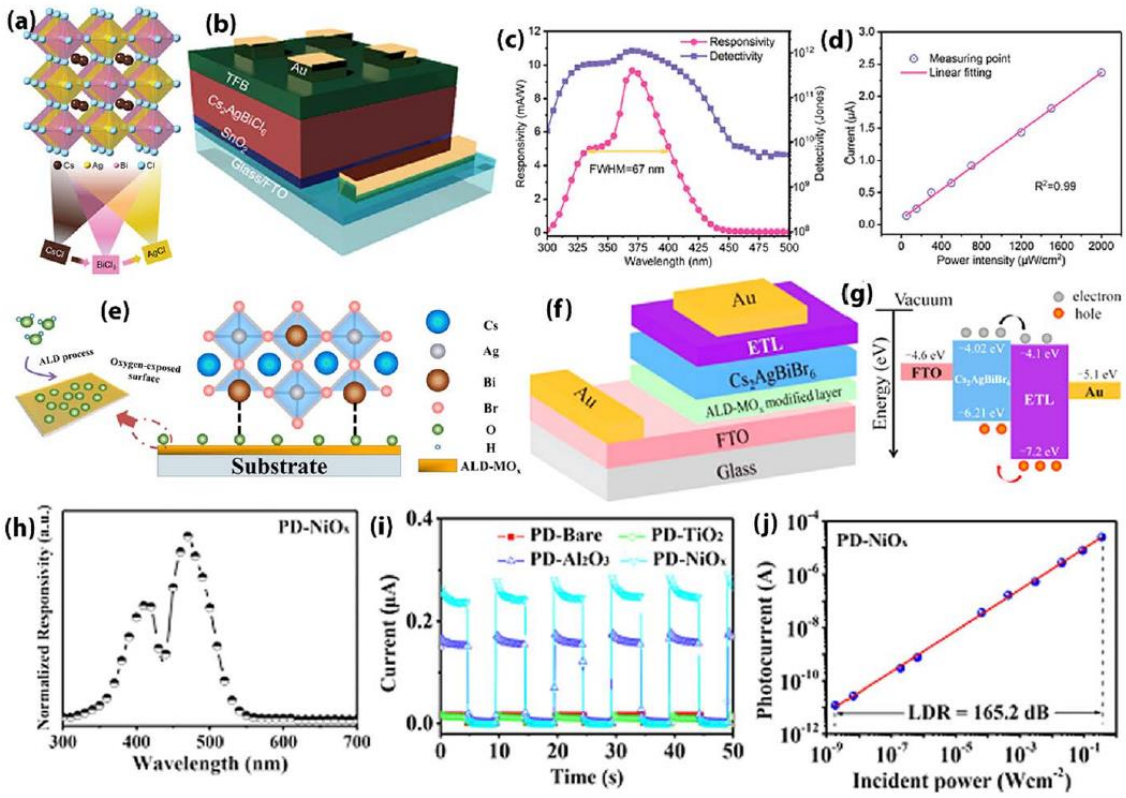

Figure 1.10. (a) Scheme of sequential vapor deposition process for the fabrication of $Cs_2AgBiCl_6$ double perovskite film. (b) Device configuration of $Cs_2AgBiCl_6$ self-powered UV PD. (c) Spectral dependence of photoresponsivity and detectivity of the PD. (d) Variation of photocurrent with the illumination intensity of 365 nm and 0 V of applied bias.[85] (e) Schematic

illustration of the Bi–O interfacial interaction at the ALD-MO_x layer-modified substrate/ $Cs_2AgBiBr_6$ double perovskite interface. (f) Schematic configuration of the $Cs_2AgBiBr_6$ -based heterojunction PD. (g) Energy band structure of the PD. (h) Spectral dependence of normalized responsivity of PD-NiO_x device. (i) Dynamic photoresponse of PDs with different substrates. (j) Linear Dynamic Range of PD-NiO_x PD.[86]

Table 1.2 Summary of the UV photodetector based on lead-free double perovskites

Active materials	Responsivity (mA/W)	Specific detectivity (Jones)	Response range	Year
$Cs_2AgInCl_6$ Single Crystal[84]	13 @ 5 V	9.6E11 @ 5 V	360-480 nm	2018
$Cs_2AgBiBr_6$ 2D layer[82]	110 @ 0 V	2E10 @ 0 V	320-435 nm	2018
$Cs_2AgBiBr_6$ 2D layer[87]	7010 @ 5 V	5.66E11 @ 5 V	300-600 nm	2018
$Cs_2AgBiCl_6$ 2D layer[88]	~10 @ 0 V	~10E12 @ 0 V	300-450 nm	2020
$Cs_2NaBiCl_6$ 2D layer[89]	67.98 @1.5 V	4.17E11 @ 1.5 V	365 nm	2021

1.5 Characterization used in the thesis

In order to understand the characterization and analysis technique in the following chapters, I hereby introduce the structural, optical, and electrical characterization techniques, thereafter I will clarify the measurement and calculation or analytic method of light-emitting diodes and photodiodes.

1.5.1 X-ray diffraction (XRD)

Powder X-ray diffraction is one of the most effective methods to analyze lattice structure, crystal plane direction, and crystal size. As Figure XX shows, the wavelength of the X-ray and the atom distance in the lattice is on the same scale, X-ray exhibit wavability and further produce Bragg's diffraction effect, which means when the pathlength difference is equal to an integer number of X-ray wavelength, the diffraction happens. The relationship of diffraction plane distance d dependent on diffraction angle θ follows Bragg's law: [90]

$$2d\ \sin\theta = n\lambda\ (n = 1,2,3\ \ldots)$$

Where n is the reflet index. The phase of measured sample could be confirmed by compare the XRD data and the standard PDF, and also the crystal direction and crystal structure could be figured out. Furthermore, the crystalline size τ is calculated by the full width at half maximum (FWHM) β of diffraction peak, their relationship can be expressed as Scherrer equation: [91]

$$\tau = \frac{K\lambda}{\beta \cos\theta}$$

Where K is a dimensionless shape factor which has a typical value of about 0.9.

With the XRD data, only the crystal phase information could be obtained. If the parameter of crystalline cell is needed, Rietveld technique is necessary. The powder XRD instrument used in this work is MiniFlex from Rigaku Corporation.

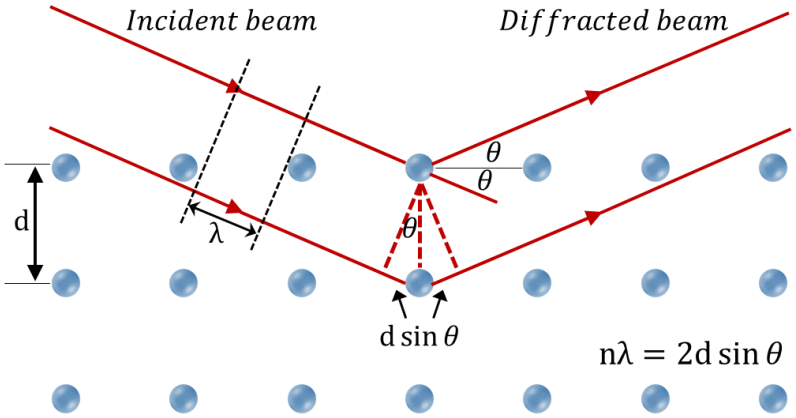

Figure 1.11 The scheme of Bragg's diffraction

1.5.2 Transmission Electroscope Microscope (TEM)

TEMs employ a high voltage electron beam in order to create an image. An electron gun at the top of a TEM emits electrons that travel through the microscope's vacuum tube. Rather than having a glass lens focusing the light (as in the case of light microscopes), the TEM employs an electromagnetic lens which focuses the electrons into a very fine beam. This beam then passes through the specimen, which is very thin, and the electrons either scatter or hit a fluorescent screen at the bottom of the microscope. An image of the specimen with its assorted parts shown in different shades according to its density appears on the screen. Crystal structure can be clearly seen by TEM. The sample for TEM is nanocrystals dispersed in hexane solution, and it is ultrasonicated 20 min, then dropped on the ultrathin carbon substrate, the type of TEM is JEOL 2100F, the voltage is 200 kV.

1.5.3 X-ray photoelectron spectroscopy (XPS)

X-ray photoelectron spectroscopy (XPS) is a technique which analyzes the element composition and chemical bonding state of materials. The detective depth of XPS is very shallow, around several nanometers, the surface information can be obtained. When the X-ray was irradiated on the sample surface, materials and the photoelectron effect occurs, the detector record the energy and amount of escaped electrons.[91] And this instrument is conducted under high vacuum degree because the electron information is detected.

Generally, the energy of index X-ray is known, therefore, the binding energy of electron could be calculated by index X-ray energy substrate to escaped electron energy. Each element has its XPS specific peak at the specific binding energy, so XPS can define the element accurately.

The XPS utilized in this work is Ulvac Quantera SXM produced by ULVAC-PHI Inc.

1.5.4 UV-Visible absorption spectroscopy

UV-Visible absorption spectroscopy is used for measuring the absorption, transmission, scattering or reflectance spectrum of materials (range from 190-900 nm),

the absorbance and bandgap can be obtained by fitting, the formula are as follows:

$$T = e^{-\alpha d}$$

$$\alpha = \frac{\ln(1/T)}{d}$$

Where T is the transmission of sample, α is the absorbance of sample, d indicates the thickness of the sample. According to the basic semiconductor theory, the relationship of absorbance and photon energy follows the law:

$$\alpha h\nu = A(h\nu - E_g)^n$$

For direct bandgap semiconductor materials, n=2; for indirect semiconductor materials, n=0.5; while, for transition forbidden direct bandgap semiconductors, n=1.5. A indicates a constant, the relationship of photon energy and wavelength follows the de Broglie relationship: $h\nu = \frac{1240}{\lambda}$

1.5.5 Steady-state Fluorescence Spectroscopy (PL)

Fluorescence indicates the process that materials are excited after absorb electro magnetron irradiation and then emit electro magnetron wave. PL spectrum is aim to characterize and analyze this process, it is divided into excitation spectrum and emission spectrum. The difference between two spectrums is that, for excitation spectrum, collected wavelength is fixed and excitation wavelength is changed, the change of PL intensities with the adjustable excitation wavelength is recorded; while for emission spectrum, the excitation wavelength is fixed, the change of PL intensities with the adjustable emission wavelength is recorded. PLE spectrum normally reflects the optimal excitation wavelength.

1.5.6 Time-resolved Photoluminescence (TR-PL)

Different from the steady-state fluorescent spectrum, time-resolved PL spectrum indicates that the pulse light source with specific wavelength is used to excite the measured sample, then the decay process of fluorescence signal is recorded and analyzed. The decay process of fluorescence reflects the kinetic mechanism from excited state to

ground state. This process is normally along with the defect recombination, Auger recombination and energy transfer. These processes couldn't be observed in steady-state PL spectrum. PL intensity decay curve at specific wavelength is measured, the PL lifetime is fitted by the exponential function:

$$I(t) = I_0 e^{-t/\tau}$$

Where I_0 is the start PL intensity, τ is the PL lifetime, the meaning of PL lifetime is the time duration of the PL intensity decay to start PL intensity after the excitation leave, the above equation is for single recombination channel, if there are multiple recombination channels, multipin exponential index is used in fitting to get multipin lifetime value.

1.5.7 Photoluminescence Quantum Yield (PLQY)

Photoluminescence quantum yield (PLQY) measurement is used for characterizing the fluorescence efficiency of materials, which means the ratio of the amount of incident photons and the amount of absorbed excited photons. PLQY measurement has two types of methods, relative method and absolute method. The relative method is sensitive to the reference sample and the excitation wavelength, therefore the deviation of PLQY result is large, absolute method is used in this work. The measurement method is as follows, the absorption (A1) and PL emission (P1) of reference sample are measured firstly, then the absorption (A2) and PL emission (P2) of sample are measured, finally the PLQY of measured sample is calculated by the equation:

$$PLQY = \frac{P_2 - P_1}{A_2 - A_1}$$

1.6 Research motivation and thesis organization

Lead-free double perovskite nanocrystals (LDP NCs) are promising materials as an alternative to lead-based perovskite nanocrystals to solve the problem of toxicity and instability. Specifically, replacing two Pb^{2+} ions with a combination of monovalent and trivalent cations could be a solution for forming three-dimensional (3D) perovskite structures, whose chemical formula is $A_2B(I)B(III)X_6$, which is called double-perovskite

structure. LDP NCs have excellent properties such as good stability, long carrier lifetime, long photoluminescence lifetimes, high photoluminescence quantum yield and solution-processability. Therefore, LDP NCs are considered to be promising materials for optoelectronic applications including photodetector, photocatalysts, light-emitting diodes and solar cells.

$Cs_2AgB'X_6$ (B' = In or Bi, X = Cl or Br) has the potential to be applied in optoelectronic devices. While it owns a high absorption coefficient, good stability and low toxicity, there is still a challenge in improving its performance to reach or exceed that of lead-based perovskites. For example, the defects introduced by indium can create trap states in the bandgap of $Cs_2AgInCl_6$ thus affecting the material properties. Therefore, the thesis focuses on the composition tuning of LDP NCs for photodiode application by B-site doping strategies as well as the bandgap engineering by X-site anion composition tuning in LDP NCs to realize efficient wavelength-selective photodiodes.

In Chapter 1, a general background about lead-free double perovskites and a simple overview of ultraviolet photodiodes are introduced. In particular, the process and purpose of the research which lead to the conception of the research topic were clarified.

In Chapter 2, Na-alloyment and Bi-doping were employed in improving the optical properties of $Cs_2AgInCl_6$ NCs. We synthesized $Cs_2Ag_{0.65}Na_{0.35}InCl_6$ NCs doped with bismuth (Bi^{3+}) ions and investigated their photophysical properties to reveal the role of the dopant on the enhanced photoemission properties. Specifically, it was found that the photoluminescence quantum yield (PL QY) increased up to 33.2% by 2% Bi-doping. The optical bandgap of the NCs decreased from 3.47 eV to 3.41 eV as the amount of the dopant increased from 2% to 15%. To find out the effect of Bi-doping, the temperature-dependent PL properties of the undoped and doped NCs were investigated by utilizing steady-state and time-resolved PL spectroscopy. With increasing the temperature from 20 K to 300 K, the PL intensities of the doped NCs decreased slower than the undoped ones. The correlated average PL lifetimes of both the bismuth-doped and undoped NCs decreased with increasing temperature. The experimental results revealed that all the NC samples

showed thermal quenching with the temperature increasing, and the PL quenching was suppressed in bismuth-doped NCs. Importantly, the exciton binding energy value was estimated according to the temperature-dependent PL intensities, which act as the guidance of the work in the following chapter.

In Chapter 3, we first demonstrated the highly responsive lead-free perovskite photodiode based on $Cs_2Ag_{0.35}Na_{0.65}InCl_6$ nanocrystals. The composition tuning strategy is introduced to enhance the device performance of photodiodes. Employed with a device structure composed of ZnO: Al electron-transport layer and Poly[(9,9-dioctylfluorenyl-2,7-diyl)-co-(4,4'-(N-(4-sec-butylphenyl)diphenylamine)] (TFB) hole transport layer, lead-free perovskite nanocrystal photodiodes exhibit a high responsivity of 3.03 A/W and specific detectivity of 1.29 x 10^{11} Jones under the illumination of a 340 nm light source. Moreover, the ultraviolet (UV) photodiodes show good performance under the self-powered mode, which exhibits a responsivity of 0.07 A/W and specific detectivity of 5.04 x 10^{10} Jones. Our work verifies the great potential of the $Cs_2Ag_{0.35}Na_{0.65}InCl_6$ nanocrystals in the application of environmentally friendly and high-performance UV photodiodes, which also demonstrates that the nanocrystals with proper exciton binding energy are preferable in the photodiode application.

In Chapter 4, we studied on Cs_2AgBiX_6 (X = Cl or Br) NCs, which replaces In^{3+} by Bi^{3+} to avoid the generation of indium-caused defects and obtain strong absorption for the photodiode application. The band gap engineering was conducted through the composition tuning from $Cs_2AgBiCl_6$ to $Cs_2AgBiBr_6$. We fabricated lead-free double perovskite photodiodes response to UV-Visible range. Specifically, the $Cs_2AgBiBr_6$-based photodiode exhibits a characteristic detection peak at 340 nm with a responsivity of 3.21 mA/W, a specific detectivity up to 8.91 x 10^{10} Jones and a fast response speed with rise/fall time of 30/35 ms. The excellent performance of self-driven photodiodes lights up the prospect of lead-free double perovskite nanocrystals in highly efficient optoelectronic devices without external power sources.

In Chapter 5, we clarify the conclusions and propose the outlook on the efficacy

and future potential of the lead-free double perovskite nanocrystals.

References

1. Gong, S. *et al.* A wearable and highly sensitive pressure sensor with ultrathin gold nanowires. *Nat. Commun.* **5**, 3132 (2014).
2. Nozaki, K. *et al.* Femtofarad optoelectronic integration demonstrating energy-saving signal conversion and nonlinear functions. *Nat. Photonics* **13**, 454–459 (2019).
3. Zhao, R., Gu, Z., Li, P., Zhang, Y. & Song, Y. Flexible and Wearable Optoelectronic Devices Based on Perovskites. *Adv. Mater. Technol.* **7**, 2101124 (2022).
4. Ricciardi, A. *et al.* Integrated Optoelectronic Devices Using Lab-On-Fiber Technology. *Adv. Mater. Technol.* **7**, 2101681 (2022).
5. Cui, Q. *et al.* Efficient Eco-Friendly Flexible X-ray Detectors Based on Molecular Perovskite. *Nano Lett.* **22**, 5973–5981 (2022).
6. Fang, X. *et al.* New Ultraviolet Photodetector Based on Individual Nb2O5 Nanobelts. *Adv. Funct. Mater.* **21**, 3907–3915 (2011).
7. Mancebo, S. E. & Wang, S. Q. Skin cancer: role of ultraviolet radiation in carcinogenesis. *Rev. Environ. Health* **29**, 265–273 (2014).
8. Su, L., Yang, W., Cai, J., Chen, H. & Fang, X. Self-powered ultraviolet photodetectors driven by built-in electric field. *Small* **13**, 1701687 (2017).
9. Zhou, J. *et al.* An overview on emerging photoelectrochemical self-powered ultraviolet photodetectors. *Nanoscale* **8**, 50–73 (2016).
10. Peng, L., Hu, L. & Fang, X. Low-dimensional nanostructure ultraviolet photodetectors. *Adv. Mater.* **25**, 5321–5328 (2013).
11. Peng, L., Hu, L. & Fang, X. Energy harvesting for nanostructured self-powered photodetectors. *Adv. Funct. Mater.* **24**, 2591–2610 (2014).
12. Wang, H. *et al.* Low-dimensional metal halide Perovskite photodetectors. *Adv. Mater.* **33**, 2003309 (2021).

13. Chen, J., Ouyang, W., Yang, W., He, J. & Fang, X. Recent progress of heterojunction ultraviolet photodetectors: materials, integrations, and applications. *Adv. Funct. Mater.* **30**, 1909909 (2020).

14. Al Fattah, M. F. *et al.* Sensing of ultraviolet light: a transition from conventional to self-powered photodetector. *Nanoscale* **13**, 15526–15551 (2021).

15. Barnes, P. W. *et al.* Ozone depletion, ultraviolet radiation, climate change and prospects for a sustainable future. *Nat. Sustain.* **2**, 569–579 (2019).

16. Wang, M. *et al.* Self-powered UV photodetectors and imaging arrays based on NiO/IGZO heterojunctions fabricated at room temperature. *Opt. Express* **30**, 27453–27461 (2022).

17. Schefer, R. W., Kulatilaka, W. D., Patterson, B. D. & Settersten, T. B. Visible emission of hydrogen flames. *Combust. Flame* **156**, 1234–1241 (2009).

18. Monroy, E., Omnès, F. & Calle, F. Wide-bandgap semiconductor ultraviolet photodetectors. *Semicond. Sci. Technol.* **18**, R33 (2003).

19. Zhang, K. *et al.* A flexible p-CuO/n-MoS 2 heterojunction photodetector with enhanced photoresponse by the piezo-phototronic effect. *Mater. Horizons* **4**, 274–280 (2017).

20. Chen, H., Liu, H., Zhang, Z., Hu, K. & Fang, X. Nanostructured photodetectors: from ultraviolet to terahertz. *Adv. Mater.* **28**, 403–433 (2016).

21. Esopi, M. R., Calcagno, M. & Yu, Q. Organic ultraviolet photodetectors exhibiting photomultiplication, low dark current, and high stability. *Adv. Mater. Technol.* **2**, 1700025 (2017).

22. Ouyang, B., Zhang, K. & Yang, Y. Self-powered UV photodetector array based on P3HT/ZnO nanowire array heterojunction. *Adv. Mater. Technol.* **2**, 1700208 (2017).

23. Zhang, Y. *et al.* Lead-Free Perovskite Photodetectors: Progress, Challenges, and Opportunities. *Adv. Mater.* **33**, 2006691 (2021).

24. Zhou, J. & Huang, J. Photodetectors Based on Organic–Inorganic Hybrid Lead Halide Perovskites. *Adv. Sci.* **5**, 1700256 (2018).

25. Guo, R. *et al.* Advances in colloidal quantum dot-based photodetectors. *J. Mater. Chem. C* **10**, 7404–7422 (2022).

26. Xie, C., Liu, C.-K., Loi, H.-L. & Yan, F. Perovskite-Based Phototransistors and Hybrid Photodetectors. *Adv. Funct. Mater.* **30**, 1903907 (2020).

27. Li, X. *et al.* Healing All-Inorganic Perovskite Films via Recyclable Dissolution–Recyrstallization for Compact and Smooth Carrier Channels of Optoelectronic Devices with High Stability. *Adv. Funct. Mater.* **26**, 5903–5912 (2016).

28. Yang, B. *et al.* Ultrasensitive and Fast All-Inorganic Perovskite-Based Photodetector via Fast Carrier Diffusion. *Adv. Mater.* **29**, 1703758 (2017).

29. Zhang, L. *et al.* Toward Highly Sensitive Polymer Photodetectors by Molecular Engineering. *Adv. Mater.* **27**, 6496–6503 (2015).

30. García de Arquer, F. P., Armin, A., Meredith, P. & Sargent, E. H. Solution-processed semiconductors for next-generation photodetectors. *Nat. Rev. Mater.* **2**, 16100 (2017).

31. Xie, Y. *et al.* A self-powered UV photodetector based on TiO 2 nanorod arrays. *Nanoscale Res. Lett.* **8**, 1–6 (2013).

32. Zhao, B. *et al.* An Ultrahigh Responsivity (9.7 mA W−1) Self-Powered Solar-Blind Photodetector Based on Individual ZnO–Ga2O3 Heterostructures. *Adv. Funct. Mater.* **27**, 1700264 (2017).

33. Wang, Z. L., Chen, J. & Lin, L. Progress in triboelectric nanogenerators as a new energy technology and self-powered sensors. *Energy Environ. Sci.* **8**, 2250–2282 (2015).

34. Wang, Y. *et al.* All-Oxide NiO/Ga2O3 p–n Junction for Self-Powered UV Photodetector. *ACS Appl. Electron. Mater.* **2**, 2032–2038 (2020).

35. Zheng, W. *et al.* A self-powered ultraviolet photodetector driven by opposite Schottky junction. *J. Alloys Compd.* **712**, 425–430 (2017).

36. Yang, X. *et al.* Boosting Photoresponse of Self-Powered InSe-Based Photoelectrochemical Photodetectors via Suppression of Interface Doping. *ACS Nano*

16, 8440–8448 (2022).

37. Deka Boruah, B. Zinc oxide ultraviolet photodetectors: rapid progress from conventional to self-powered photodetectors. *Nanoscale Adv.* **1**, 2059–2085 (2019).

38. Ren, X. *et al.* Environmentally Robust Black Phosphorus Nanosheets in Solution: Application for Self-Powered Photodetector. *Adv. Funct. Mater.* **27**, 1606834 (2017).

39. Christians, J. A., Miranda Herrera, P. A. & Kamat, P. V. Transformation of the Excited State and Photovoltaic Efficiency of CH3NH3PbI3 Perovskite upon Controlled Exposure to Humidified Air. *J. Am. Chem. Soc.* **137**, 1530–1538 (2015).

40. Huang, H. *et al.* Spontaneous Crystallization of Perovskite Nanocrystals in Nonpolar Organic Solvents: A Versatile Approach for their Shape-Controlled Synthesis. *Angew. Chemie Int. Ed.* **58**, 16558–16562 (2019).

41. Min, H. *et al.* Perovskite solar cells with atomically coherent interlayers on SnO2 electrodes. *Nature* **598**, 444–450 (2021).

42. Protesescu, L. *et al.* Nanocrystals of Cesium Lead Halide Perovskites (CsPbX3, X = Cl, Br, and I): Novel Optoelectronic Materials Showing Bright Emission with Wide Color Gamut. *Nano Lett.* **15**, 3692–3696 (2015).

43. Li, X. *et al.* Lead-Free Halide Perovskites for Light Emission: Recent Advances and Perspectives. *Adv. Sci.* **8**, 2003334 (2021).

44. Saparov, B. & Mitzi, D. B. Organic–Inorganic Perovskites: Structural Versatility for Functional Materials Design. *Chem. Rev.* **116**, 4558–4596 (2016).

45. Li, W. *et al.* Chemically diverse and multifunctional hybrid organic–inorganic perovskites. *Nat. Rev. Mater.* **2**, 16099 (2017).

46. Schmidt, L. C. *et al.* Nontemplate Synthesis of CH3NH3PbBr3 Perovskite Nanoparticles. *J. Am. Chem. Soc.* **136**, 850–853 (2014).

47. Li, X. *et al.* CsPbX3 Quantum Dots for Lighting and Displays: Room-Temperature Synthesis, Photoluminescence Superiorities, Underlying Origins and White Light-Emitting Diodes. *Adv. Funct. Mater.* **26**, 2435–2445 (2016).

48. Akkerman, Q. A. *et al.* Solution Synthesis Approach to Colloidal Cesium Lead

Halide Perovskite Nanoplatelets with Monolayer-Level Thickness Control. *J. Am. Chem. Soc.* **138**, 1010–1016 (2016).

49. Bekenstein, Y., Koscher, B. A., Eaton, S. W., Yang, P. & Alivisatos, A. P. Highly Luminescent Colloidal Nanoplates of Perovskite Cesium Lead Halide and Their Oriented Assemblies. *J. Am. Chem. Soc.* **137**, 16008–16011 (2015).

50. Sichert, J. A. *et al.* Quantum Size Effect in Organometal Halide Perovskite Nanoplatelets. *Nano Lett.* **15**, 6521–6527 (2015).

51. Weidman, M. C., Goodman, A. J. & Tisdale, W. A. Colloidal Halide Perovskite Nanoplatelets: An Exciting New Class of Semiconductor Nanomaterials. *Chem. Mater.* **29**, 5019–5030 (2017).

52. Malgras, V. *et al.* Observation of Quantum Confinement in Monodisperse Methylammonium Lead Halide Perovskite Nanocrystals Embedded in Mesoporous Silica. *J. Am. Chem. Soc.* **138**, 13874–13881 (2016).

53. Li, W. *et al.* Ethanol–water-assisted room temperature synthesis of CsPbBr3/SiO2 nanocomposites with high stability in ethanol. *J. Mater. Sci.* **54**, 3786–3794 (2019).

54. Zhong, Q. *et al.* One-Pot Synthesis of Highly Stable CsPbBr3@SiO2 Core–Shell Nanoparticles. *ACS Nano* **12**, 8579–8587 (2018).

55. Li, Z.-J. *et al.* Photoelectrochemically Active and Environmentally Stable CsPbBr3/TiO2 Core/Shell Nanocrystals. *Adv. Funct. Mater.* **28**, 1704288 (2018).

56. Akkerman, Q. A., Rainò, G., Kovalenko, M. V & Manna, L. Genesis, challenges and opportunities for colloidal lead halide perovskite nanocrystals. *Nat. Mater.* **17**, 394–405 (2018).

57. Brandt, R. E., Stevanović, V., Ginley, D. S. & Buonassisi, T. Identifying defect-tolerant semiconductors with high minority-carrier lifetimes: beyond hybrid lead halide perovskites. *MRS Commun.* **5**, 265–275 (2015).

58. Kang, J. & Wang, L.-W. High Defect Tolerance in Lead Halide Perovskite CsPbBr3. *J. Phys. Chem. Lett.* **8**, 489–493 (2017).

59. Liu, F. *et al.* Highly Luminescent Phase-Stable CsPbI3 Perovskite Quantum Dots

Achieving Near 100% Absolute Photoluminescence Quantum Yield. *ACS Nano* **11**, 10373–10383 (2017).

60. Zhu, H. *et al.* Screening in crystalline liquids protects energetic carriers in hybrid perovskites. *Science.* **353**, 1409–1413 (2016).

61. Boles, M. A., Ling, D., Hyeon, T. & Talapin, D. V. The surface science of nanocrystals. *Nat. Mater.* **15**, 141–153 (2016).

62. De Roo, J. *et al.* Highly Dynamic Ligand Binding and Light Absorption Coefficient of Cesium Lead Bromide Perovskite Nanocrystals. *ACS Nano* **10**, 2071–2081 (2016).

63. Liu, S. *et al.* Precipitation and tunable emission of cesium lead halide perovskites (CsPbX3, X = Br, I) QDs in borosilicate glass. *Ceram. Int.* **44**, 4496–4499 (2018).

64. Babayigit, A., Ethirajan, A., Muller, M. & Conings, B. Toxicity of organometal halide perovskite solar cells. *Nat. Mater.* **15**, 247–251 (2016).

65. Giustino, F. & Snaith, H. J. Toward Lead-Free Perovskite Solar Cells. *ACS Energy Lett.* **1**, 1233–1240 (2016).

66. McCall, K. M., Stoumpos, C. C., Kostina, S. S., Kanatzidis, M. G. & Wessels, B. W. Strong Electron–Phonon Coupling and Self-Trapped Excitons in the Defect Halide Perovskites A3M2I9 (A = Cs, Rb; M = Bi, Sb). *Chem. Mater.* **29**, 4129–4145 (2017).

67. Slavney, A. H., Hu, T., Lindenberg, A. M. & Karunadasa, H. I. A Bismuth-Halide Double Perovskite with Long Carrier Recombination Lifetime for Photovoltaic Applications. *J. Am. Chem. Soc.* **138**, 2138–2141 (2016).

68. Volonakis, G. *et al.* Lead-Free Halide Double Perovskites via Heterovalent Substitution of Noble Metals. *J. Phys. Chem. Lett.* **7**, 1254–1259 (2016).

69. Hoefler, S. F., Trimmel, G. & Rath, T. Progress on lead-free metal halide perovskites for photovoltaic applications: a review. *Monatshefte für Chemie - Chem. Mon.* **148**, 795–826 (2017).

70. Saparov, B. *et al.* Thin-Film Preparation and Characterization of Cs3Sb2I9: A Lead-Free Layered Perovskite Semiconductor. *Chem. Mater.* **27**, 5622–5632 (2015).

71. Lehner, A. J. *et al.* Crystal and Electronic Structures of Complex Bismuth Iodides

A3Bi2I9 (A = K, Rb, Cs) Related to Perovskite: Aiding the Rational Design of Photovoltaics. *Chem. Mater.* **27**, 7137–7148 (2015).

72. Fan, Q. *et al.* Lead-Free Halide Perovskite Nanocrystals: Crystal Structures, Synthesis, Stabilities, and Optical Properties. *Angew. Chemie Int. Ed.* **59**, 1030–1046 (2020).

73. Wu, X. *et al.* Synthesis of Lead-free CsGeI3 Perovskite Colloidal Nanocrystals and Electron Beam-induced Transformations. *Chem. – An Asian J.* **13**, 1654–1659 (2018).

74. Yang, B. *et al.* Lead-Free Silver-Bismuth Halide Double Perovskite Nanocrystals. *Angewandte Chemie* vol. 130 5457–5461 (2018).

75. Locardi, F. *et al.* Colloidal Synthesis of Double Perovskite Cs2AgInCl6 and Mn-Doped Cs2AgInCl6 Nanocrystals. *J. Am. Chem. Soc.* **140**, 12989–12995 (2018).

76. Yang, B. *et al.* Colloidal Synthesis and Charge-Carrier Dynamics of Cs2AgSb1−yBiyX6 (X: Br, Cl; 0 ≤y ≤1) Double Perovskite Nanocrystals. *Angew. Chemie Int. Ed.* **58**, 2278–2283 (2019).

77. Meng, W. *et al.* Parity-Forbidden Transitions and Their Impact on the Optical Absorption Properties of Lead-Free Metal Halide Perovskites and Double Perovskites. *J. Phys. Chem. Lett.* **8**, 2999–3007 (2017).

78. Mir, W. J., Sheikh, T., Arfin, H., Xia, Z. & Nag, A. Lanthanide doping in metal halide perovskite nanocrystals: spectral shifting, quantum cutting and optoelectronic applications. *NPG Asia Mater.* **12**, 9 (2020).

79. Liu, Y., Nag, A., Manna, L. & Xia, Z. Lead-Free Double Perovskite Cs2AgInCl6. *Angew. Chemie Int. Ed.* **60**, 11592–11603 (2021).

80. Luo, J. *et al.* Efficient and stable emission of warm-white light from lead-free halide double perovskites. *Nature* **563**, 541–545 (2018).

81. Li, S. *et al.* Self-Trapped Exciton to Dopant Energy Transfer in Rare Earth Doped Lead-Free Double Perovskite. *Adv. Opt. Mater.* **7**, 1901098 (2019).

82. Wu, C. *et al.* Highly Efficient and Stable Self-Powered Ultraviolet and Deep-Blue Photodetector Based on Cs2AgBiBr6/SnO2 Heterojunction. *Adv. Opt. Mater.* **6**,

1800811 (2018).

83. Yang, J. *et al.* Stable, High-Sensitivity and Fast-Response Photodetectors Based on Lead-Free Cs2AgBiBr6 Double Perovskite Films. *Adv. Opt. Mater.* **7**, 1801732 (2019).

84. Luo, J. *et al.* Cs2AgInCl6 Double Perovskite Single Crystals: Parity Forbidden Transitions and Their Application For Sensitive and Fast UV Photodetectors. *ACS Photonics* **5**, 398–405 (2018).

85. Wang, M., Zeng, P., Wang, Z. & Liu, M. Vapor-Deposited Cs2AgBiCl6 Double Perovskite Films toward Highly Selective and Stable Ultraviolet Photodetector. *Adv. Sci.* **7**, 1903662 (2020).

86. Yan, G. *et al.* Importance of Bi–O Bonds at the Cs2AgBiBr6 Double-Perovskite/Substrate Interface for Crystal Quality and Photoelectric Performance. *ACS Appl. Mater. Interfaces* **12**, 6064–6073 (2020).

87. Lei, L.-Z. *et al.* High-efficiency and air-stable photodetectors based on lead-free double perovskite Cs 2 AgBiBr 6 thin films. *J. Mater. Chem. C* **6**, 7982–7988 (2018).

88. Wang, M., Zeng, P., Wang, Z. & Liu, M. Vapor-Deposited Cs 2 AgBiCl 6 Double Perovskite Films toward Highly Selective and Stable Ultraviolet Photodetector. *Adv. Sci.* **7**, 1903662 (2020).

89. Li, H. *et al.* A Highly Stable Photodetector Based on a Lead-Free Double Perovskite Operating at Different Temperatures. *J. Phys. Chem. Lett.* **12**, 5682–5688 (2021).

90. Elton, L. R. B. & Jackson, D. F. X-Ray Diffraction and the Bragg Law. *Am. J. Phys.* **34**, 1036–1038 (1966).

91. Holzwarth, U. & Gibson, N. The Scherrer equation versus the'Debye-Scherrer equation'. *Nat. Nanotechnol.* **6**, 534 (2011).

Chapter 2 Impact of Bismuth-Doping on the Enhanced Radiative Recombination in Lead-Free Double Perovskite Nanocrystals

2.1 Introduction

Perovskite nanocrystals (NCs) $APbX_3$ ($A = Cs^+$, $CH_3NH_3^+$ or $NH_2HCNH_2^+$, $X = Cl^-$, Br^- or I^-) have become up-and-coming in various optoelectronic applications including light-emitting devices,[1–6] solar cells,[7–12] photodetectors,[13–17] photocatalysis[18–20] and lasers,[21–23] which is attributed to their distinguished optical and electrical properties such as high defect tolerance,[24,25] high photoluminescence (PL) quantum yield (QY),[26–28] tunable bandgap,[29,30] high color purity,[31,32] high carrier mobility, large diffusion length,[33] high absorption coefficient[34] as well as solution-processability.[35,36] Even though there are many advantages mentioned above, the toxicity and instability of lead halide perovskite NCs are still concerned as non-negligible hindrances toward practical application.[37,38]

To surmount the obstacles, stable and environmentally friendly perovskite composition is urgently desired. To replace Pb^{2+}, the obvious approach is to use Sn^{2+} and Ge^{2+} because of their similar electronic properties.[39,40] However, Sn^{2+} and Ge^{2+}-based halide perovskites are quite unstable, and are easily oxidized to Sn^{4+} and Ge^{4+}. Additionally, trivalent cations Bi^{3+} and Sb^{3+} halide perovskites have also been studied,[41] but the compounds with chemical formula $A_3B_2X_9$ have shown unfavorable properties such as large bandgap and low defect tolerance.[42] In particular, replacing two Pb^{2+} ions with a combination of monovalent and trivalent cations could be one solution for forming a three-dimensional perovskite structure, whose chemical formula is $A_2B(I)B(III)X_6$, which is called double perovskite structure. For instance, $Cs_2AgBiCl_6$ and $Cs_2AgInCl_6$ compounds have shown good photophysical characteristics after effective alloying or doping engineering.[43,44]

Among the reported lead-free double perovskite materials, it has been reported recently that the bulk crystals of alloyed $Cs_2Ag_xNa_{1-x}InCl_6$: Bi double perovskites show a high PLQY of 86 ± 5% with self-trapped exciton (STE) emitting warm-white light.[45] STE is normally formed by fast self-trapped excitons in materials that possess soft lattice and strong exciton-coupling characteristics such as halide crystals[46] and organic molecular crystals,[47] wherein excitons relax back to the ground state by emitting photons with broadband and large stokes shifts after being trapped, therefore the emission energy of STE is smaller than the bandgap, as shown in Scheme 1.[48] In 2022, Bi^{3+}-doped $Cs_2Ag_{0.4}Na_{0.6}InCl_6$ microcrystals (~10 μm) with a remarkably high PLQY of 97.33% were achieved by Peng et al. through a precipitation approach.[43] Since then double perovskite NCs could also become a potential material for single-emitter layers applied in optical applications.[49]

Colloidal perovskite NCs terminated with surfactant ligands for high dispersibility in non-polar solvents are promising for optoelectronic applications, due to their convenient deposition on substrates based on solution processes.[50] Thereafter, for further enhancing the practicality in applications, there are efforts for the colloidal synthesis of the double perovskite NCs.[51-53] More recently, Hu et al. synthesized the white-light emitting $Cs_2Ag_{0.17}Na_{0.83}In_{0.88}Bi_{0.12}Cl_6$ NCs with PLQY of 64% by elemental ratio optimization and ligand passivation.[54] In the double perovskites structure system, it was reported that Bi-doping was responsible for the increased PLQY.[51,55,56] For the underlying mechanism of improved PLQY through doping bismuth, there are several reported viewpoints, one is defect passivation proved by the comparison of PL lifetimes, and another is that exciton localization is promoted after Bi-doping which is concluded from theoretical simulation.[45] Theory predicts the radiative recombination of photogenerated carriers in the Bi-Ag centers provided that the Bi cations are at a small amount.[53] However, the experimentally fundamental photophysical properties of Bi-doped double perovskite NCs, which could be favorable of understanding the doping effect, are still one of the challenging themes.

Temperature-dependent PL study is established to discuss the nonradiative relaxation processes and electron-phonon interactions in the quantum dots of semiconductors.[57-59] In the present study, we used the temperature-dependent PL approach to reveal the possible excitation and emission mechanism arising from the doping of Bi^{3+} ions in $Cs_2Ag_{0.65}Na_{0.35}InCl_6$ NCs. Changes in PL intensity and linewidth as a function of temperature were measured to gain the insights into the carrier relaxation and electron-phonon coupling processes. Additionally, temperature-dependent time-resolved PL spectra of the NCs were measured. Furthermore, the structural characterization of NCs at different temperature were analyzed by low-temperature X-ray diffraction (LT-XRD) technique to clarify the crystal phase condition as the temperature varies.

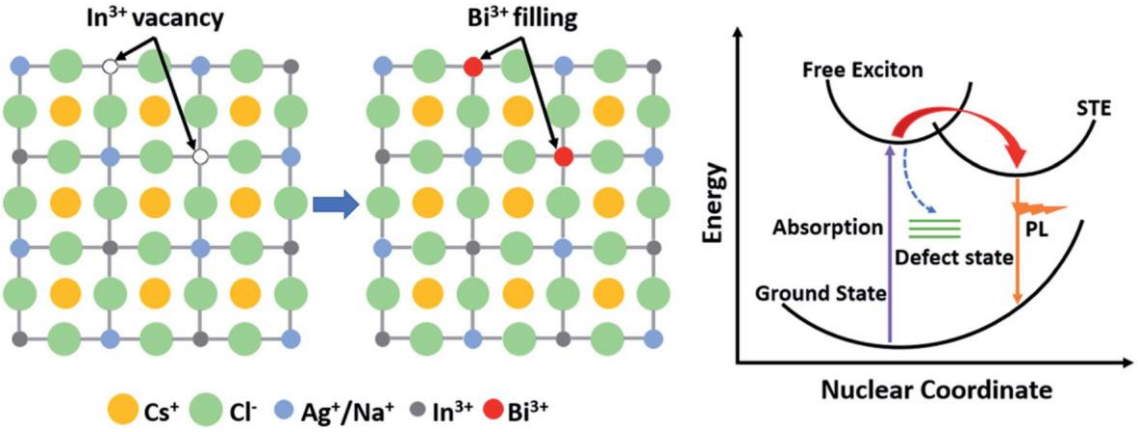

Scheme 2.1 Schematic diagram of the Bi-doping effect and proposed self-trapped emission.

2.2 Experimental

2.2.1 Reagents and chemicals

All reagents were used without further purification. Cesium acetate (CsOAc, 99.99%), silver acetate (AgOAc, 99%), sodium acetate (NaOAc, 99.99%), indium(III) acetate ($In(OAc)_3$, 99.99%), bismuth(III) acetate ($Bi(OAc)_3$, 99.99%), chlorotrimethylsilane (TMSCl, 98%), oleic acid (OA, 90%) and 1-octadecence (ODE, 95%) were purchased from Sigma-Aldrich. Oleylamine (OAm, 80-90%) was purchased from Kanto Kagaku. Toluene (99.5%), hexane (96%) and ethyl acetate (99.5%) were

purchased from Wako Chemicals.

2.2.2 Preparation of $Cs_2Ag_{0.65}Na_{0.35}In_{1-x}Bi_xCl_6$ NCs

The NCs were fabricated following the modified version of the hot-injection method reported by Han and co-workers.[52] In a typical synthesis, 1.3 mmol CsOAc, 0.36 mmol AgOAc, 0.54 mmol NaOAc, 1.98 mmol $In(OAc)_3$ and 0.02 mmol $Bi(OAc)_3$ were loaded in a 50 mL three-neck flask containing 5.6 mL OA, 1.4 mL OLA and 20 mL ODE, after degassed 1 hour at 110 ºC, heated to 165 ºC in 12 min under N_2 flow. A 0.8 mL TMSCl was injected quickly, with temperature increasing 2 min longer, and the production was rapidly cooled down to 25 ºC by the ice-water bath. The resultant NCs were centrifuged at 9000 rpm for 20 min and washed with toluene to remove unreacted precursors. Then the collected precipitate was further dispersed in hexane, thereafter the resultant solution was centrifuged at 6000 rpm for 15 min and the supernatant was collected. The same volume of ethyl acetate was added for the final centrifugation, the final precipitate was collected and vacuum-dried for further characterization.

2.2.3 Characterization

The powder samples with different Bi-doping amounts were analyzed by using a JASCO V-650 UV-visible spectrometer. High-resolution transmission electron microscopy (HR-TEM) characterization was performed using JEM-2100F2 (JEOL) at 200 kV acceleration voltage. Scanning transmission electron microscopy energy dispersive spectroscopy (STEM-EDS) was utilized for the element analysis. Samples for TEM analysis were prepared by drop-casting of the 0.1 mg mL-1 hexane solution of NCs on the carbon-coated copper grids. PLQYs were measured at room temperature using the absolute PLQY spectrometer C11347-11 from Hamamatsu Photonics Co. Ltd with a 150 W xenon light source coupled to a monochromator for wavelength discrimination, an integrating sphere as a sample chamber, and a multichannel spectroscope for signal detection. The powder-form specimens of NCs were used for the characterization of

PLQY. PL properties were measured with the powder samples pressed and coated on the interlayer between two 1 cm x 1 cm quartz glasses. Measurements were conducted using a modular double-grating Czerny-Turner monochromator and an iHR 320 emission monochromator (1200 lines mm-1 of gratings) coupled to a photodetector on a NanoLog Horiba Jobin Yvon spectrofluorometer with a 450 E Xe arc lamp. The value of photon power for excitation estimated using a power meter (PD 300, Ophir Optronics Solutions Ltd., And NOVA II display) was 0.014 mW cm-2. To measure the temperature-dependent PL spectra, the samples were placed inside a cryostat holder connected to a Gifford-McMahon cooler and controlled by a Mercury iTC temperature controller. The temperature was tuned from 3 K to 300 K with 20 K/step. The LT-XRD characterization in the temperature range between 5 K and 300 K, was carried out using Rigaku SmartLab (9 kW, Cu Kα1) equipped with a cryostat attachment, the sample was tightly attached using Apiezon-N grease on copper sample holder.

2.3 Results and discussion

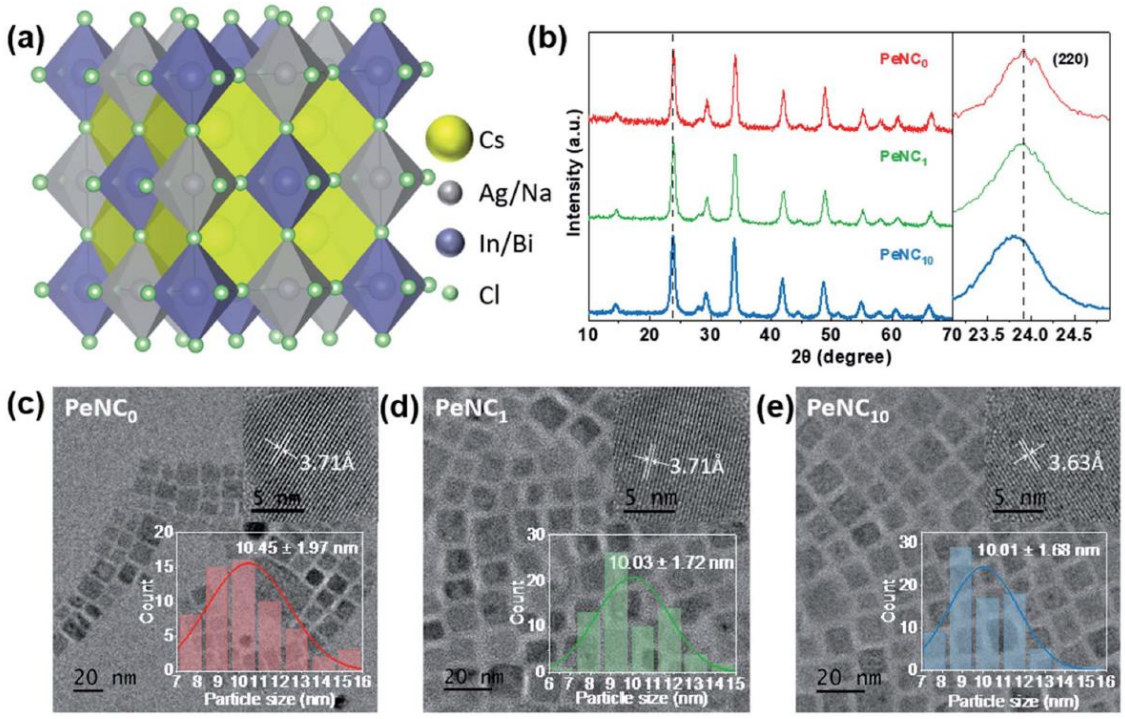

Figure 2.1 Crystal structure of $Cs_2Ag_{1-x}Na_xIn_{1-y}BiyCl_6$ double perovskite. Yellow, silver, purple, and green spheres represent Cs, Ag/Na, In/Bi, and Cl atoms, respectively. (b) X-ray diffraction

(XRD) patterns measured at room temperature of $PeNC_x$ ($Cs_2Ag_{0.65}Na_{0.35}In_{1-x}Bi_xCl_6$, x =0, 1%, 10%) and the enlarged XRD patterns of the samples. Transmission electron microscopy (TEM) images of (c) $PeNC_0$, (d) $PeNC_1$, and (e) $PeNC_{10}$. The scale bar is 20 nm. The inset in the top-right corner is the high-resolution TEM image, whose scale bar is 5 nm. The inset in the bottom right corner is the size-distribution histogram.

Table 2.1 STEM-EDS elemental analysis on Bi-doped and undoped NCs.

EDS/atom ratio	Cs/In	Ag/(Ag+Na)	Na/(Ag+Na)	In/(In+Bi)	Bi/(In+Bi)	Cl/In
$PeNC_0$	2.32	0.66	0.35	1	0	5.61
$PeNC_1$	2.39	0.65	0.35	0.98	0.02	5.50
$PeNC_{10}$	2.48	0.63	0.37	0.85	0.15	4.86

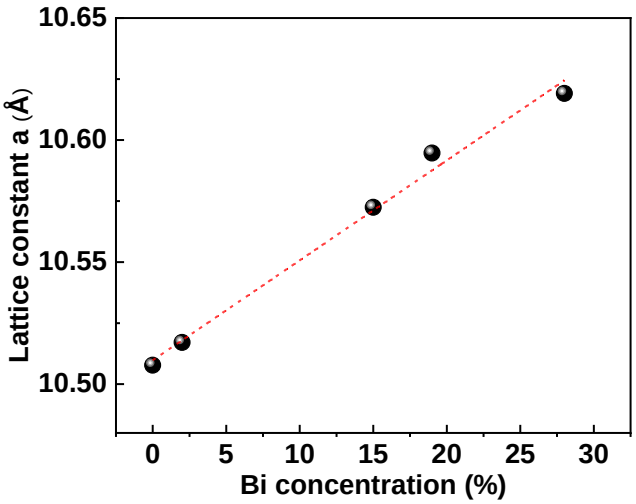

Figure 2.2 The lattice constant as function of Bi concentration in $Cs_2Ag_{0.65}Na_{0.35}InCl_6$ NCs.

Bi-doped and undoped $Cs_2Ag_{0.65}Na_{0.35}InCl_6$ NCs were synthesized by the modified hot-injection method.[52] Here, $PeNC_0$, $PeNC_1$, and $PeNC_{10}$ represent $Cs_2Ag_{0.65}Na_{0.35}InCl_6$ double perovskite NCs with 0%, 1%, and 10% Bi in precursor concentration, respectively. The STEM-EDS analysis revealed that the final product of $PeNC_1$ and $PeNC_{10}$ have 2% and 15% Bi. It should be noted that all the composition values stand for the actual value for the results which we obtained from STEM-EDS listed in Table 2.1. The atom ratio of Cs/In and Cl/In shows the range of 2.32-2.48 and 4.86-5.61, respectively. This deviation with the feeding ratio is reasonable compared with other double perovskite

nanocrystals.[60,61] On one hand, the large ratio of Cs/In might be caused by the indium vacancies in this structure, and this ratio decreased with the increasing bismuth amount. Meanwhile, the elemental ratio deviation was also found in $Cs_2AgBiCl_6$, whereas the ratio of 2.25 and 20 for Cs/Ag and Cl/Ag, respectively.[60] However, the cause of the large ratio of Cl/In has not been clearly clarified yet, which needs to be investigated in future work. HR-TEM images of $Cs_2Ag_{0.65}Na_{0.35}InCl_6$ NCs show that the crystals had a cubic structure. As shown in Figure 2.1(c)-(e), the average sizes of $PeNC_0$, $PeNC_1$, and $PeNC_{10}$ were 10.45 ± 1.97 nm, 10.03 ± 1.72 nm, and 10.01 ± 1.68 nm, respectively. Their sizes are quite close to each other. Based on that, the particle size difference is not considered in the subsequent discussion of optical properties. Additionally, the corresponding measured lattice distances are 3.71, 3.71 and 3.63 Å, which are in accord with the (220) planes in $Cs_2Ag_{0.65}Na_{0.35}InCl_6$ NCs where XRD showed in the following part. XRD patterns of $Cs_2Ag_{0.65}Na_{0.35}InCl_6$ NCs matched well with the cubic double perovskite structure ($Cs_2AgInCl_6$ ICSD code 1546186, $Cs_2NaInCl_6$ ICSD code 4003575) in all three samples, and no impurity phases were observed (see Figure 2.1(b)), which demonstrates the good phase stability of $Cs_2Ag_{0.65}Na_{0.35}InCl_6$ double perovskite. Comparing the XRD pattern of $PeNC_1$ with that of $PeNC_{10}$, we see a small shift of the 220 peak from 23.9° to 23.8° with increasing the bismuth amount from 2% to 15%, possibility due to the lattice expansion resulting from the substitution of Bi^{3+} ions (117 pm) for In^{3+} ions (92 pm) in the cubic lattice.[62] $Cs_2Ag_{0.65}Na_{0.35}InCl_6$ NCs with a higher concentration of Bi-dopant were also synthesized, and the lattice parameters of NCs as a function of Bi-dopant concentration (see Figure 2.2), which shows that when Bi amount increases, the crystal structure of NCs abbey Vegard's law,[63] and there is no impurity phase or phase separation.

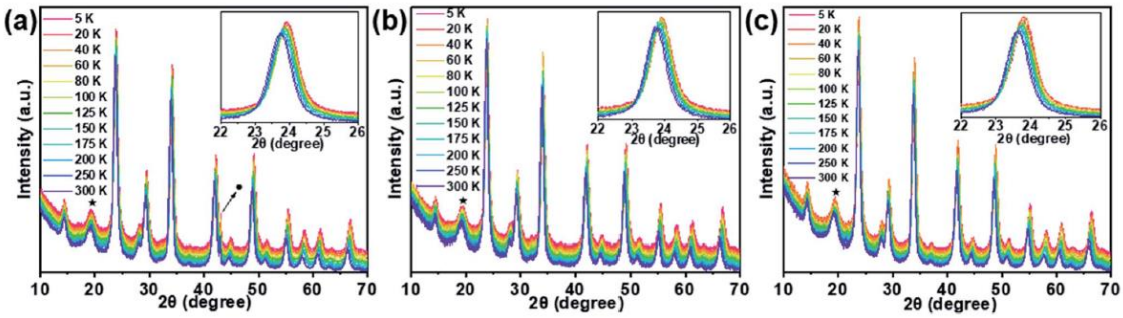

Figure 2.3 LT-XRD patterns of (a) $PeNC_0$, (b) $PeNC_1$, and (c) $PeNC_{10}$ in the temperature range from 5–300 K. Peaks ★ and ● indicate the signals from the X-ray window materials of the cryostat and from the Cu sample holder, respectively.

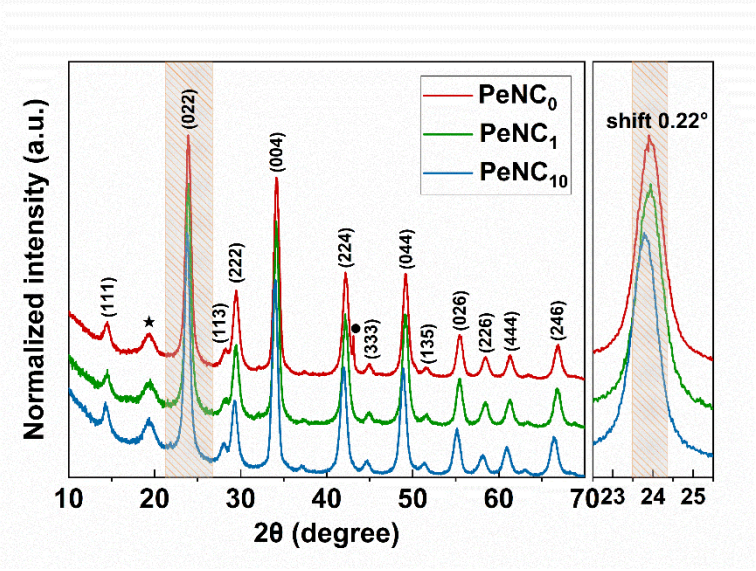

Figure 2.4 XRD patterns of $PeNC_0$, $PeNC_1$ and $PeNC_{10}$ measured at 5 K. The peaks indicating as ★ and ● are from the X-ray window materials of the cryostat and from Cu sample holder, respectively.

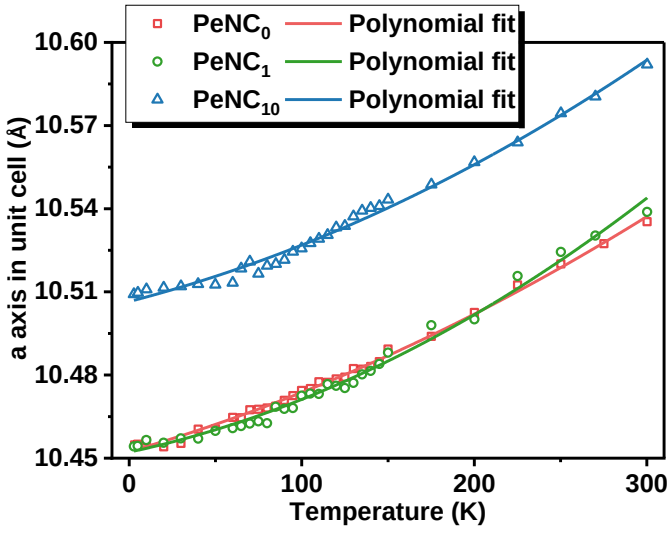

Figure 2.5 Thermal expansion coefficient fitting of $PeNC_0$, $PeNC_1$ and $PeNC_{10}$.

It is common that structural phase transition happens in lead halide perovskite NCs under low temperatures, which is caused by the size effect or doping effect.[64,65,66] A phase transition from tetragonal- to cubic structures has been observed at 122 K for the $Cs_2AgBiBr_6$ which is one of the double perovskite crystals.[67] Such a temperature-dependent phase transition influences adversely the device performance in some cases. To investigate the structural stability of the $Cs_2Ag_{0.65}Na_{0.35}InCl_6$ NCs when temperature varies, LT-XRD measurements were performed. For the LT-XRD measurements between 5 K and 300 K, the $PeNC_0$, $PeNC_1$, and $PeNC_{10}$ samples were selected. (see Figure 2.3(a)-(c)). All the LT-XRD patterns of the doped samples showed similar to that of the undoped sample. The absence of additional peaks appeared over the whole temperature range for the doped samples. This indicates that the phase stayed in the cubic phase, implying good crystallinity and purity. At 5 K, when the Bi amount increased to 2%, the diffraction lines of the $PeNC_1$ has a relative shift compared to that of the $PeNC_0$, while the 15% Bi-doped $PeNC_{10}$ shows 0.22° smaller than $PeNC_0$, which is consistent with the characteristics shown at room temperature (see Figure 2.4). On the temperature dependence, all the XRD peaks shifted toward a small diffraction angle with increasing temperature possibly due to a lattice expansion. The experimental data of the lattice constant were fitted by a second-order polynomial as shown in Figure 2.5. The linear coefficient of thermal expansion for $PeNC_0$, $PeNC_1$, and $PeNC_{10}$ was found to be 1.71×10^{-5}/K, 1.27×10^{-5}/K, and 1.52×10^{-5}/K, respectively. The results of the calculation indicate that the doped sample changes slowly with temperature which permits high thermal stability for their target applications.

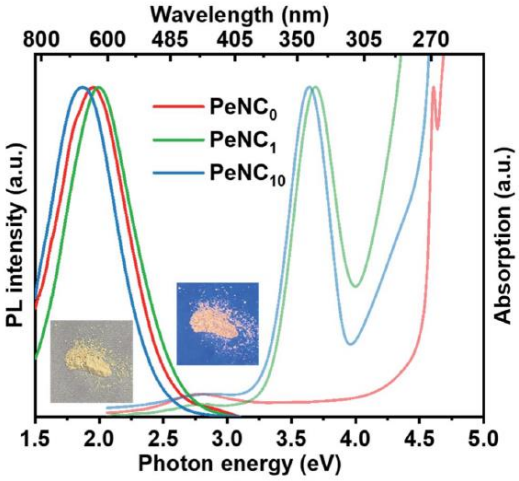

Figure 2.6 UV-Vis absorption and PL spectra of $PeNC_0$ (ex. 275 nm), $PeNC_1$ (ex. 330 nm), and $PeNC_{10}$ (ex. 330 nm) with nanocrystals in the powder form. Photographs showing the $PeNC_1$ powder sample under room illumination (left) and UV irradiation (right).

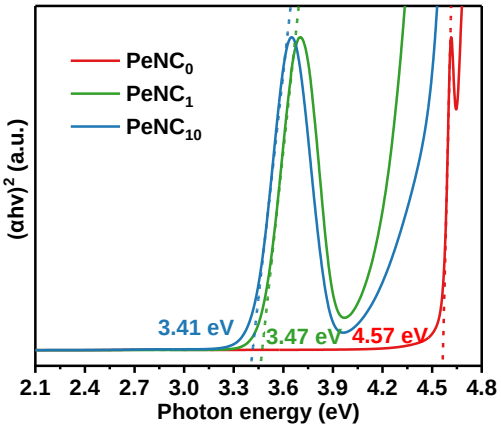

Figure 2.7 $(\alpha h\nu)^2$- $h\nu$ plots of $PeNC_0$ (red), $PeNC_1$ (green) and $PeNC_{10}$ (blue). The values of E_g extracted from extrapolations to $\alpha = 0$.

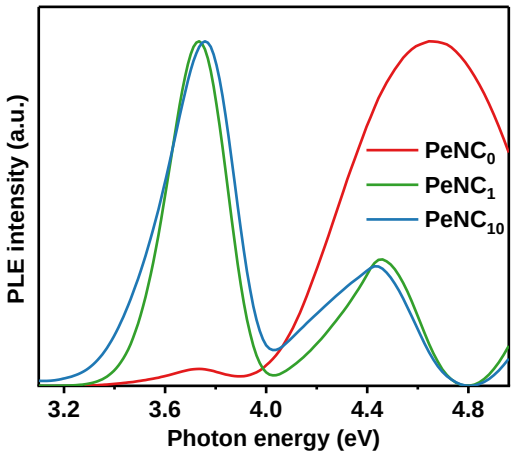

Figure 2.8 Excitation spectra of photoluminescence measured for $PeNC_0$ (634 nm-emission peak), $PeNC_1$ (592 nm-emission peak) and $PeNC_{10}$ (630 nm-emission peak).

Optical properties of $Cs_2Ag_{0.65}Na_{0.35}InCl_6$ NCs were studied by UV-Vis and PL spectroscopies. And the resultant optical absorption and PL spectra of the $Cs_2Ag_{0.65}Na_{0.35}InCl_6$ NC samples were shown in Figure 2.6. Cation doping has complicated impacts on the perovskite nanocrystals because even a very small substitution of In^{3+} by Bi^{3+} would greatly affect the bandgap and excitons radiation channel. For undoped sample $PeNC_0$, the conduction band minimum (CBM) is mainly contributed by In-5s and Cl-3p, and the valence band maximum (VBM) is contributed by Ag-4d and Cl-3p.45 When Bi^{3+} ions doped into the NCs, it is noted that an additional excitonic absorption peak presented near 3.7 eV, which is attributed to band-edge absorption where Bi could be the localization center for electrons at conduction band edges.[55,68] With incremental addition of Bi ions from 2% to 15%, the optical bandgap estimated by the Tauc plots (Figure 2.7) was narrowed from 3.47 eV to 3.41 eV, which is caused by the lower CBM of p-orbital derived from Bi cations.[69] The excitation energy was obtained from the photoluminescence excitation (PLE) peak value (Figure 2.8). The PL spectrum of the $PeNC_0$ was observed by excitation with 4.51 eV while PL spectra of the $PeNC_1$ and $PeNC_{10}$ were obtained by excitation with 3.76 eV. The redshift in PL spectra of $PeNC_{10}$ compared to $PeNC_1$ is corresponding to the narrowed bandgap. The highest PLQY of 33.2% was observed for $PeNC_1$, while 3% for $PeNC_0$ and 15.5% for $PeNC_{10}$.

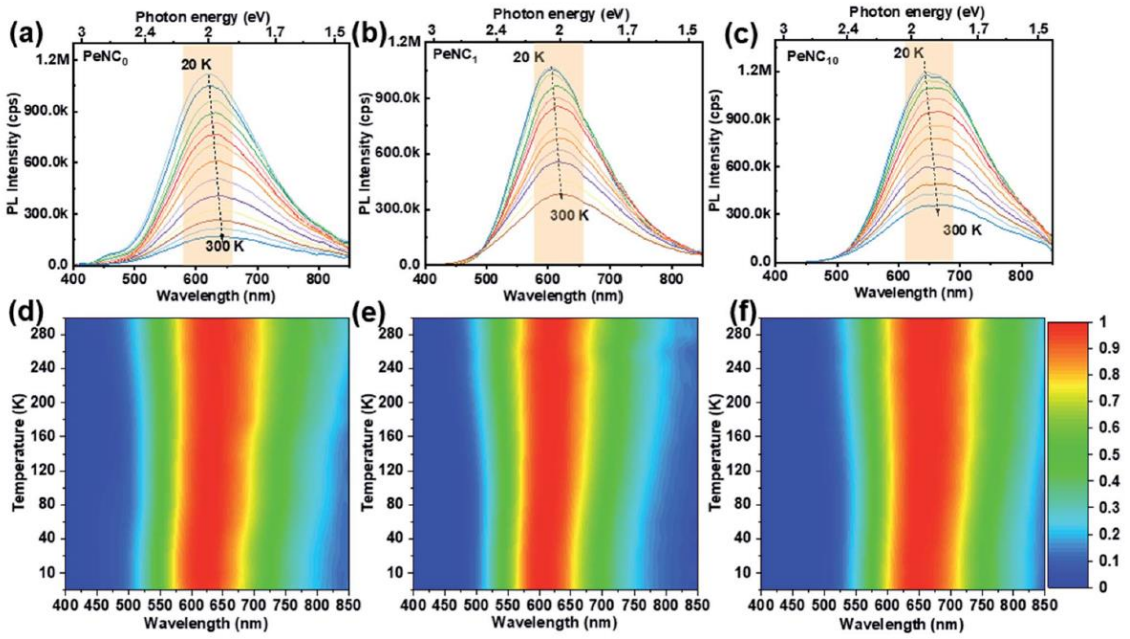

Fig. 2.9 Temperature-dependent PL spectra of (a) $PeNC_0$ (ex. 275 nm), (b) $PeNC_1$ (ex. 330 nm), and (c) $PeNC_{10}$ (ex. 330 nm) from 20 to 300 K. Normalized PL intensity mapped with the emission wavelength and temperature for (d) $PeNC_0$ (e) $PeNC_1$, and (f) $PeNC_{10}$.

To discuss a possible mechanism of the doping effect on the PL performance, the PL spectra of the $PeNC_0$, $PeNC_1$, and $PeNC_{10}$ in powder form were measured in the temperature range between 20 K to 300 K. Figure 4 shows the variation in PL spectra of $PeNC_0$, $PeNC_1$, and $PeNC_{10}$ photoexcited at 4.51 eV, 3.76 eV, and 3.76 eV, respectively. It is worth mentioning that there is a weak peak at around 2.76 eV for the $PeNC_0$ (see Figure 2.9(a)), which could be attributed to the free-exciton emission.[45] Figure 2.9(a)-(c) shows the decreasing trend in PL intensity of all three samples with the rise in temperature. Meanwhile, the samples exhibit a redshift in the PL peak when the temperature increases from 20 K to 100 K. Interestingly, this behavior is opposite to most of the reported perovskite NCs.[64,70-72] There are a few papers showing a redshift trend, but those crystals are known to show the temperature-dependent phase transition or halide-type effect.[63,73] However, the result of the LT-XRD measurement showed that all three samples keep ideal cubic perovskite structure and unchanged crystal phase in the temperature range between 5 K and 300 K. As we mentioned before, the broad emission of the $Cs_2Ag_{0.65}Na_{0.35}InCl_6$ NCs originated from STE emission. Herein we propose that the redshift of the PL peak is

attributed to the narrowing emission bandgap of the self-trapped state with the temperature increasing, which results from the lattice dilatation and electron-phonon interaction similar to conventional semiconductor materials.[74]

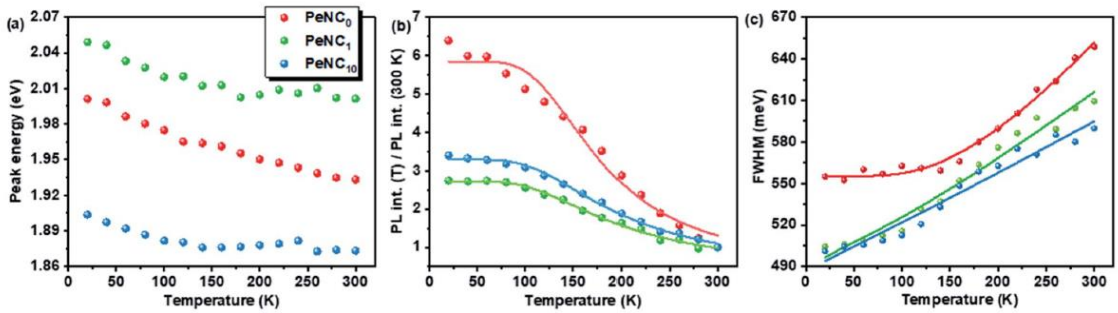

Fig. 2.10 Temperature-dependent PL (a) emission peak energy, (b) peak intensity, and (c) FWHM of $PeNC_0$, $PeNC_1$, and $PeNC_{10}$.

The variation in PL peak energy with temperature from 20 K to 300 K for the three samples is shown in Figure 2.10(a). The PL peak energies of the NC powders for $PeNC_0$, $PeNC_1$, and $PeNC_{10}$ are determined to be 2.00 eV, 2.05 eV, and 1.90 eV at 20 K and 1.93 eV, 2.00 eV, and 1.87 eV at 300 K, respectively. It is seen that the PL peak energy of $PeNC_0$ decreases significantly (0.25 meV/K) while the other two doped samples (i.e., $PeNC_1$ and $PeNC_{10}$) exhibit show a smaller shift of 0.18 and 0.11 meV/K with increasing temperature. On the other hand, the integrated PL intensities for $PeNC_0$, $PeNC_1$, and $PeNC_{10}$ samples slightly decrease with increasing temperature as shown in Figure 2.10(b), yielding PL quenching. The successive decreasing behaviors of the PL intensity with the rise in temperature appear due to the thermal activation of nonradiative channels present in the NCs. According to this context, the $PeNC_0$ contains the largest amounts of defects as nonradiative channels whereas the $PeNC_1$ has the smallest defect density (Scheme 2.1), consistent with the difference in PLQY. The temperature-dependent PL intensities were fitted well according to the Arrhenius formula:[75]

$$I(T) = \frac{I_0}{1 + Aexp\left(-\frac{E_A}{K_B T}\right)}$$

where I_0 is the PL intensity at 20 K, A is the proportional constant, E_A is the activation energy, and K_B is the Boltzmann constant. The estimated values of thermal activation energy were 55.8 meV, 46.3 meV, and 48.8 meV for the $PeNC_0$, $PeNC_1$, and $PeNC_{10}$ samples.

It can be seen from Figure 2.9(d)-(f) that the PL full-width at half maximum (FWHM) is broaden for each sample with the temperature increases, which is attributed to the strong exciton-phonon coupling. As shown in Figure 2.10(c), the PL-FWHM is fitted by adapting the independent Boson model:[76]

$$\boldsymbol{\Gamma(T) = \Gamma_0 + \sigma\Gamma + \frac{\Gamma_{OP}}{\exp\left(\frac{\hbar\omega_{OP}}{K_B T}\right) - 1}}$$

where Γ_0 is the inhomogeneous broadening contribution, σ and Γ_{OP} describe the interactions of the exciton-acoustic phonon interaction and exciton-optical phonon interaction contributions to the FWHM broadening, respectively, and $\hbar\omega_{OP}$ is the optical phonon energy. The fitted optical phonon energy of $PeNC_0$, $PeNC_1$ and $PeNC_{10}$ are 47.9 meV, 41.2 meV and 42.0 meV, respectively. Smaller optical phonon energy values of the doped samples imply that much phonons are produced, which would serve as a scattering center,[77] possibly due to strained crystalline lattice by doped ions. Electron-phonon coupling is also crucial to the formation of STEs. Because if the "soft" lattice nature of octahedral halide coordination in the double perovskite structure, strong electron-phonon coupling results in elastic structural distortion, leading to broadband STE emission.[48] A highly efficient radiative recombination process thus requires a suitable electron-phonon coupling effect. The electron-phonon coupling could be quantitatively characterized by Huang-Rhys factor *S*. *S* value is normally small in free-exciton materials such as CdSe[79] and $CsPbBr_3$,[80] but larger than 10 in STE materials. As shown in Figure 2.11, the fitted *S* values for $PeNC_0$, $PeNC_1$ and $PeNC_{10}$ are 24.1, 27.7 and 26.7, respectively, which are smaller than bulk crystals (~40)[45] but larger than reported NCs (15.5).[54] It demonstrated that $Cs_2Ag_{0.65}Na_{0.35}InCl_6$ NCs possesses enough electron-phonon coupling which is beneficial to the formation of STE emission, to achieve high PLQY.

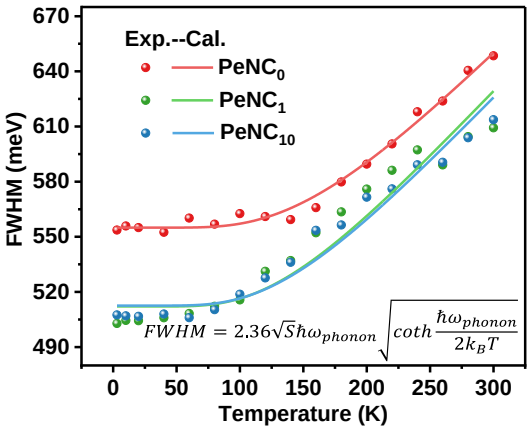

Figure 2.11 Temperature-dependent PL FWHM of $PeNC_0$, $PeNC_1$ and $PeNC_{10}$.

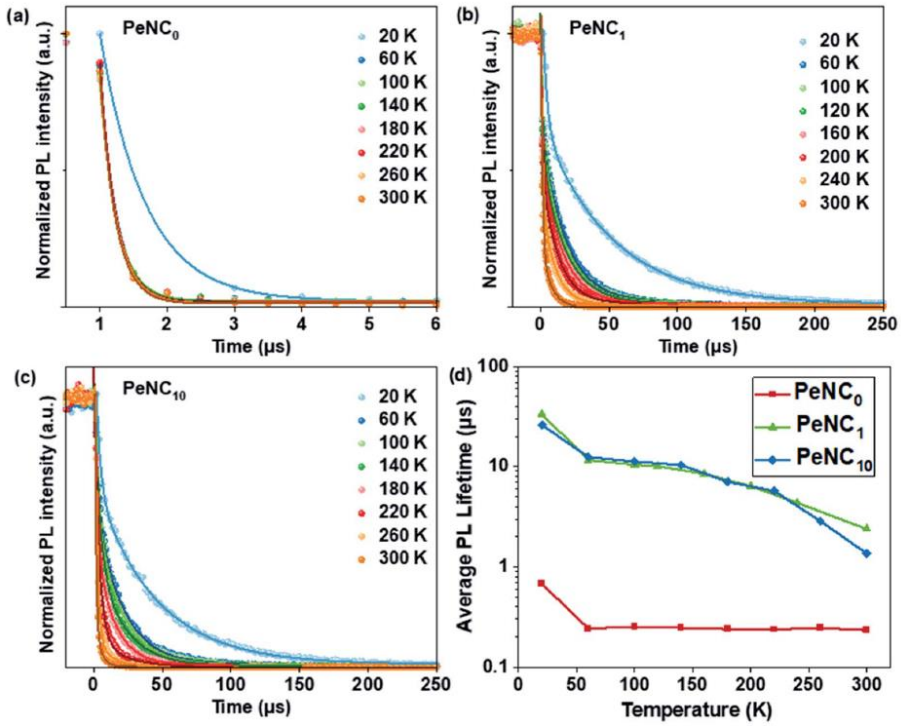

Fig. 2.12 TR-PL curves of (a) $PeNC_0$ (b) $PeNC_1$, (c) $PeNC_{10}$ from 20 to 300 K and (d) their average lifetimes extracted from biexponential fitting at various temperatures.

Besides broad-band and large Stokes shift emission, a long radiative PL lifetime is also a specific property of STEs which is shown in Figure 2.12(a)-(c). To study the effect of doped Bi on the charge carrier lifetime as a function of temperature, we measured time-resolved PL as a function of temperature for sample $PeNC_0$, $PeNC_1$ and $PeNC_{10}$ between 20 K and 300 K. As shown in Figure 6d, the average lifetimes of $PeNC_1$ and $PeNC_{10}$ are

longer than that of $PeNC_0$ at all the temperatures, while the short lifetime component is ascribed to trap-assisted nonradiative recombination channel, combined with the calculated nonradiative recombination rate, it can be concluded that the Bi doping passivates the defects and suppressed the nonradiative recombination rate. The temperature-dependent average lifetime of exciton decay for Bi-doped samples were calculated by fitting the data to a biexponential fit (Table 2.2) with a long-lived component (3-50 μs) and a less long-lived component (0.8-3 μs), while the PL decay of undoped NCs was fitted by a mono-exponential function with a less-long lived component (0.23 μs). The R-square values of three plots were larger than 0.97, indicating a good of fit. As shown in Figure 2.12(d), all the three samples exhibit that the changes of lifetime are shortened a lot from 20 K to 60 K, but quite mild in the range from 60 K to 300 K, which could be described as Boltzmann distribution,[81] in accordance with the reported broadband-emission double perovskites.[52] The proportion of less long-lived component versus temperature are shown in Figure 2.13, and this contribution became prominent when temperature increases in both of $PeNC_1$ and $PeNC_{10}$. Combined with the decreased PL intensity when temperature increases, the less-long lived component could be ascribed to fast nonradiative losses likely due to the defects, while the long-lived part is contributed by the recombination of the STE. This phenomenon was also observed in other double perovskite nanocrystals.[53] As a result, the average PL lifetimes decrease with the increasing temperature due to the increasing contribution of faster nonradiative decay channels.

Table 1. Decay Parameters of PeNCs at room temperature[a]

Sample	PLQY (%)	τ_1 (μs) (A_1%)	τ_2 (μs) (A_2%)	τ_{avg} (μs)	τ_r (μs)	τ_{nr} (μs)	τ_r/τ_{nr}	R-square
$PeNC_0$	3%	0.23	-	0.23	7.67	-	-	0.998
$PeNC_1$	33.2%	1.10 (79%)	7.26 (21%)	2.40	7.23	3.59	2.01	0.973
$PeNC_{10}$	15.5%	0.81 (80%)	3.53 (20%)	1.36	8.77	1.61	5.45	0.999

[a]PLQY: photoluminescence quantum yield; τ_1-short and τ_2-long lifetime; A_1 and A_2 are the contributions for τ_1 and τ_2, respectively; τ_{avg}: average lifetime, which is calculated by $\tau_{avg} = \tau_1*A_1 +$

τ_2*A_2; τ_r-radiative recombination lifetime and τ_{nr}-nonradiative recombination lifetime, which are calculated by $\tau_r = \tau_{avg}$/PLQY and $\tau_{nr} = \tau_{avg}$/(1-PLQY), respectively.

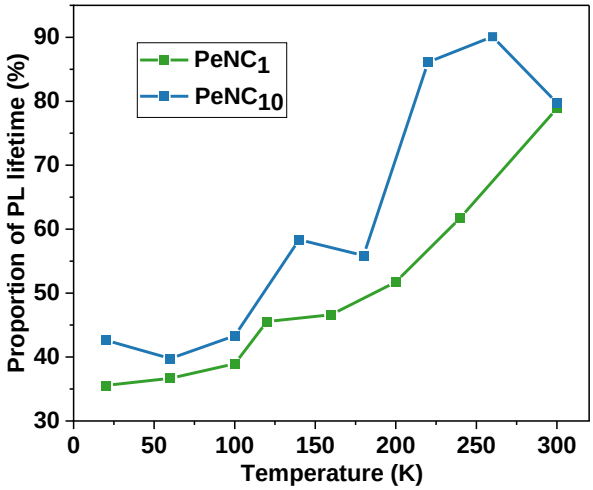

Figure 2.13 The proportion of less-long lived PL lifetime for $PeNC_1$ (green) and $PeNC_{10}$ (blue) dependent on temperature.

2.4 Conclusion

We have synthesized the undoped and bismuth-doped $Cs_2Ag_{0.65}Na_{0.35}InCl_6$ double perovskite NCs to investigate the role of the dopant on the enhanced PL performance through the LT-XRD and low-temperature PL spectroscopic studies. The LT-XRD characterization indicated the successful doping and no phase transition between 5 K and 300 K. The absolute value of PLQY was as high as 33.2% which was obtained by the 2% bismuth doping. The temperature-dependent PL study suggested that the diminished nonradiative channels brought the increase of PLQY. PL linewidth broadening from 20 K to 300 K of NCs were explained by electron-phonon coupling.

Reference

1 J. Song, J. Li, X. Li, L. Xu, Y. Dong and H. Zeng, Adv. Mater., 2015, 27, 7162–7167.

2 H. Huang, L. Polavarapu, J. A. Sichert, A. S. Susha, A. S. Urban and A. L. Rogach, NPG Asia Mater., 2016, 8, e328–e328.

3 L. Zhao, Y.-W. Yeh, N. L. Tran, F. Wu, Z. Xiao, R. A. Kerner, Y. L. Lin, G. D. Scholes, N. Yao and B. P. Rand, ACS Nano, 2017, 11, 3957–3964.

4 F. Yan, J. Xing, G. Xing, L. Quan, S. T. Tan, J. Zhao, R. Su, L. Zhang, S. Chen, Y. Zhao, A. Huan, E. H. Sargent, Q. Xiong and H. V. Demir, Nano Lett., 2018, 18, 3157–3164.

5 Y. Wei, Z. Cheng and J. Lin, Chem. Soc. Rev., 2019, 48, 310–350.

6 Y. Hassan, J. H. Park, M. L. Crawford, A. Sadhanala, J. Lee, J. C. Sadighian, E. Mosconi, R. Shivanna, E. Radicchi, M. Jeong, C. Yang, H. Choi, S. H. Park, M. H. Song, F. De Angelis, C. Y. Wong, R. H. Friend, B. R. Lee and H. J. Snaith, Nature, 2021, 591, 72–77.

7 J. Yuan, X. Ling, D. Yang, F. Li, S. Zhou, J. Shi, Y. Qian, J. Hu, Y. Sun, Y. Yang, X. Gao, S. Duhm, Q. Zhang and W. Ma, Joule, 2018, 2, 2450–2463.

8 Q. A. Akkerman, M. Gandini, F. Di Stasio, P. Rastogi, F. Palazon, G. Bertoni, J. M. Ball, M. Prato, A. Petrozza and L. Manna, Nat. Energy, 2017, 2, 16194.

9 J. Kim, B. Koo, W. H. Kim, J. Choi, C. Choi, S. J. Lim, J.-S. Lee, D.-H. Kim, M. J. Ko and Y. Kim, Nano Energy, 2019, 66, 104130.

10 J. Xi, C. Piao, J. Byeon, J. Yoon, Z. Wu and M. Choi, Adv. Energy Mater., 2019, 9, 1901787.

11 L. Hu, Q. Zhao, S. Huang, J. Zheng, X. Guan, R. Patterson, J. Kim, L. Shi, C.-H. Lin, Q. Lei, D. Chu, W. Tao, S. Cheong, R. D. Tilley, A. W. Y. Ho-Baillie, J. M. Luther, J. Yuan and T. Wu, Nat. Commun., 2021, 12, 466.

12 Y. Wang, J. Yuan, X. Zhang, X. Ling, B. W. Larson, Q. Zhao, Y. Yang, Y. Shi, J. M. Luther and W. Ma, Adv. Mater., 2020, 32, 2000449.

13 P. Ramasamy, D.-H. Lim, B. Kim, S.-H. Lee, M.-S. Lee and J.-S. Lee, Chem. Commun., 2016, 52, 2067–2070.

14 L. Zhou, K. Yu, F. Yang, J. Zheng, Y. Zuo, C. Li, B. Cheng and Q. Wang, Dalt. Trans., 2017, 46, 1766–1769.

15 C. Bi, S. V. Kershaw, A. L. Rogach and J. Tian, Adv. Funct. Mater., 2019, 29, 1902446.

16 T. Zou, X. Liu, R. Qiu, Y. Wang, S. Huang, C. Liu, Q. Dai and H. Zhou, Adv. Opt. Mater., 2019, 7, 1801812.

17 L. Jin, Y. Zhang, M. Cao, Y. Yu, Z. Chen, Y. Li, Z. Zhong, X. Hua, L. Xu, C. Cai, Y. Hu, X. Tong and J. Yao, Nanotechnology, 2021, 32, 235203.

18 L. Wu, Y. Mu, X. Guo, W. Zhang, Z. Zhang, M. Zhang and T. Lu, Angew. Chemie Int. Ed., 2019, 58, 9491–9495.

19 A. Pan, X. Ma, S. Huang, Y. Wu, M. Jia, Y. Shi, Y. Liu, P. Wangyang, L. He and Y. Liu, J. Phys. Chem. Lett., 2019, 10, 6590–6597.

20 Z. Chen, Y. Hu, J. Wang, Q. Shen, Y. Zhang, C. Ding, Y. Bai, G. Jiang, Z. Li and N. Gaponik, Chem. Mater., 2020, 32, 1517–1525.

21 C.-Y. Huang, C. Zou, C. Mao, K. L. Corp, Y.-C. Yao, Y.-J. Lee, C. W. Schlenker, A. K. Y. Jen and L. Y. Lin, ACS Photonics, 2017, 4, 2281–2289.

22 J. Chen, W. Du, J. Shi, M. Li, Y. Wang, Q. Zhang and X. Liu, InfoMat, 2020, 2, 170–183.

23 W. Gao, T. Wang, J. Xu, P. Zeng, W. Zhang, Y. Yao, C. Chen, M. Li and S. F. Yu, Small, 2021, 17, 2103065.

24 S. Mandal, S. Mukherjee, C. K. De, D. Roy, S. Ghosh and P. K. Mandal, J. Phys. Chem. Lett., 2020, 11, 1702–1707.

25 J. Kang and L.-W. Wang, J. Phys. Chem. Lett., 2017, 8, 489–493.

26 J.-W. Lee, Y. J. Choi, J.-M. Yang, S. Ham, S. K. Jeon, J. Y. Lee, Y.-H. Song, E. K. Ji, D.-H. Yoon, S. Seo, H. Shin, G. S. Han, H. S. Jung, D. Kim and N.-G. Park, ACS Nano, 2017, 11, 3311–3319.

27 B. A. Koscher, J. K. Swabeck, N. D. Bronstein and A. P. Alivisatos, J. Am. Chem. Soc., 2017, 139, 6566–6569.

28 N. Mondal, A. De and A. Samanta, ACS Energy Lett., 2019, 4, 32–39.

29 I. Levchuk, A. Osvet, X. Tang, M. Brandl, J. D. Perea, F. Hoegl, G. J. Matt, R. Hock, M. Batentschuk and C. J. Brabec, Nano Lett., 2017, 17, 2765–2770.

30 H. Huang, J. Raith, S. V. Kershaw, S. Kalytchuk, O. Tomanec, L. Jing, A. S. Susha,

R. Zboril and A. L. Rogach, Nat. Commun., 2017, 8, 996.

31 S. Y. Lee, G. Lee, D. Y. Kim, S. H. Jang, I. Choi, J. Park, H.-K. Park, J. W. Jung, K. H. Cho and J. Choi, APL Photonics, 2021, 6, 056104.

32 X. Wang, W. Li, X. Zhao, J. Fu, G. Zhang, W. Ma, W.-H. Zhang and H. W. Choi, Appl. Phys. Lett., 2022, 120, 011903.

33 G. R. Yettapu, D. Talukdar, S. Sarkar, A. Swarnkar, A. Nag, P. Ghosh and P. Mandal, Nano Lett., 2016, 16, 4838–4848.

34 J. Maes, L. Balcaen, E. Drijvers, Q. Zhao, J. De Roo, A. Vantomme, F. Vanhaecke, P. Geiregat and Z. Hens, J. Phys. Chem. Lett., 2018, 9, 3093–3097.

35 C.-S. Jo, K. Noh, S. H. Noh, H. Yoo, Y. Kim, J. Jang, H. H. Lee, Y.-J. Jung, J.-H. Lee, J. Han, J. Lim and S.-Y. Cho, ACS Appl. Nano Mater., 2020, 3, 11801–11810.

36 Y. Wang, X. Li, V. Nalla, H. Zeng and H. Sun, Adv. Funct. Mater., 2017, 27, 1605088.

37 Q. A. Akkerman, G. Rainò, M. V. Kovalenko and L. Manna, Nat. Mater., 2018, 17, 394–405.

38 J. Ye, M. M. Byranvand, C. O. Martínez, R. L. Z. Hoye, M. Saliba and L. Polavarapu, Angew. Chemie Int. Ed., 2021, 60, 21636–21660.

39 L.-J. Chen, RSC Adv., 2018, 8, 18396–18399.

40 Q. Liu, J. Yin, B.-B. Zhang, J.-K. Chen, Y. Zhou, L.-M. Zhang, L.-M. Wang, Q. Zhao, J. Hou, J. Shu, B. Song, N. Shirahata, O. M. Bakr, O. F. Mohammed and H.-T. Sun, J. Am. Chem. Soc., 2021, 143, 5470–5480.

41 K. M. McCall, C. C. Stoumpos, S. S. Kostina, M. G. Kanatzidis and B. W. Wessels, Chem. Mater., 2017, 29, 4129–4145.

42 B. Saparov, F. Hong, J.-P. Sun, H.-S. Duan, W. Meng, S. Cameron, I. G. Hill, Y. Yan and D. B. Mitzi, Chem. Mater., 2015, 27, 5622–5632.

43 K. Peng, L. Yu, X. Min, M. Hu, Y. Yang, S. Huang, Y. Zhao, Y. Deng and M. Zhang, J. Alloys Compd., 2022, 891, 161978.

44 H. Yin, Q. Kong, R. Zhang, D. Zheng, B. Yang and K. Han, Sci. China Mater., 2021, 64, 2667–2674.

45 J. Luo, X. Wang, S. Li, J. Liu, Y. Guo, G. Niu, L. Yao, Y. Fu, L. Gao, Q. Dong, C. Zhao, M. Leng, F. Ma, W. Liang, L. Wang, S. Jin, J. Han, L. Zhang, J. Etheridge, J. Wang, Y. Yan, E. H. Sargent and J. Tang, Nature, 2018, 563, 541–545.

46 W. B. Fowler, M. J. Marrone and M. N. Kabler, Phys. Rev. B, 1973, 8, 5909–5919.

47 R. Scholz, A. Y. Kobitski, D. R. T. Zahn and M. Schreiber, Phys. Rev. B - Condens. Matter Mater. Phys., 2005, 72, 1–18.

48 S. Li, J. Luo, J. Liu and J. Tang, J. Phys. Chem. Lett., 2019, 10, 1999–2007.

49 Y. Zhang, Z. Zhang, W. Yu, Y. He, Z. Chen, L. Xiao, J. Shi, X. Guo, S. Wang and B. Qu, Adv. Sci., 2022, 9, 2102895.

50 H. Zhao, R. Sun, Z. Wang, K. Fu, X. Hu and Y. Zhang, Adv. Funct. Mater., 2019, 29, 1902262.

51 Y. Liu, Y. Jing, J. Zhao, Q. Liu and Z. Xia, Chem. Mater., 2019, 31, 3333–3339.

52 P. Han, X. Mao, S. Yang, F. Zhang, B. Yang, D. Wei, W. Deng and K. Han, Angew. Chem. Int. Ed., 2019, 58, 17231–17235.

53 F. Locardi, E. Sartori, J. Buha, J. Zito, M. Prato, V. Pinchetti, M. L. Zaffalon, M. Ferretti, S. Brovelli, I. Infante, L. De Trizio and L. Manna, ACS Energy Lett., 2019, 4, 1976–1982.

54 Q. Hu, G. Niu, Z. Zheng, S. Li, Y. Zhang, H. Song, T. Zhai and J. Tang, Small, 2019, 15, 1903496.

55 D. Manna, T. K. Das and A. Yella, Chem. Mater., 2019, 31, 10063–10070.

56 M. Gray, J. Majher, T. A. Strom and P. Woodward, Inorg. Chem., 2019, 58, 13403–13410.

57 N. Shirahata, J. Nakamura, J. Inoue, B. Ghosh, K. Nemoto, Y. Nemoto, M. Takeguchi, Y. Masuda, M. Tanaka and G. A. Ozin, Nano Lett., 2020, 20, 1491–1498.

58 P. Jing, J. Zheng, M. Ikezawa, X. Liu, S. Lv, X. Kong, J. Zhao and Y. Masumoto, 2009, 13545–13550.

59 K. Wei, Z. Xu, R. Chen, X. Zheng, X. Cheng and T. Jiang, Opt. Lett., 2016, 41, 3821.

60 S. E. Creutz, E. N. Crites, M. C. D. Siena and D. R. Gamelin, Nano Lett. 2018, 18,

1118-1123.

61 P. Han, X. Zhang, C. Luo, W. Zhou, S. Yang, J. Zhao, W. Deng and K Han, ACS Cent. Sci., 2022, 6, 566-572.

62 L. H. Ahrens, Geochim. Cosmochim. Acta, 1952, 2, 155–169.

63 A.R. Denton and N. W. Ashcroft, Phys. Rev. A, 1991, 43, 3161.

64 S. B. Naghadeh, S. Sarang, A. Brewer, A. Allen, Y.-H. Chiu, Y.-J. Hsu, J.-Y. Wu, S. Ghosh and J. Z. Zhang, J. Chem. Phys., 2019, 151, 154705.

65 L. Liu, R. Zhao, C. Xiao, F. Zhang, F. Pevere, K. Shi, H. Huang, H. Zhong and I. Sychugov, J. Phys. Chem. Lett., 2019, 10, 5451–5457.

66 J.-P. Ma, J.-K. Chen, J. Yin, B.-B. Zhang, Q. Zhao, Y. Kuroiwa, C. Moriyoshi, L. Hu, O. M. Bakr, O. F. Mohammed and H.-T. Sun, ACS Mater. Lett., 2020, 2, 367–375.

67 L. Schade, A. D. Wright, R. D. Johnson, M. Dollmann, B. Wenger, P. K. Nayak, D. Prabhakaran, L. M. Herz, R. Nicholas, H. J. Snaith and P. G. Radaelli, ACS Energy Lett., 2019, 4, 299–305.

68 J. Luo, S. Li, H. Wu, Y. Zhou, Y. Li, J. Liu, J. Li, K. Li, F. Yi, G. Niu and J. Tang, ACS Photonics, 2018, 5, 398–405.

69 P. Zhang, J. Yang and S.-H. Wei, J. Mater. Chem. A, 2018, 6, 1809–1815.

70 J. Zhang, Y. Yang, H. Deng, U. Farooq, X. Yang, J. Khan, J. Tang and H. Song, ACS Nano, 2017, 11, 9294–9302.

71 Y. Tang, L. Gomez, M. van der Laan, D. Timmerman, V. Sebastian, C.-C. Huang, T. Gregorkiewicz and P. Schall, J. Mater. Chem. C, 2021, 9, 158–163.

72 B. M. Benin, D. N. Dirin, V. Morad, M. Wörle, S. Yakunin, G. Rainò, O. Nazarenko, M. Fischer, I. Infante and M. V. Kovalenko, Angew. Chemie - Int. Ed., 2018, 57, 11329–11333.

73 R. Saran, A. Heuer-Jungemann, A. G. Kanaras and R. J. Curry, Adv. Opt. Mater., 2017, 5, 1–9.

74 Y. P. Varshni, Physica, 1967, 34, 149–154.

75 M. Leroux, N. Grandjean, B. Beaumont, G. Nataf, F. Semond, J. Massies and P.

Gibart, J. Appl. Phys., 1999, 86, 3721–3728.

76 A. Al Salman, A. Tortschanoff, M. B. Mohamed, D. Tonti, F. van Mourik and M. Chergui, Appl. Phys. Lett., 2007, 90, 093104.

77 H. C. Woo, J. W. Choi, J. Shin, S. H. Chin, M. H. Ann and C. L. Lee, J. Phys. Chem. Lett., 2018, 9, 4066–4074.

78 L. Wang, W. Zheng, F. Vitale, X. Zhang, X. Li, Y. Ji, Z. Liu, O. Ghaebi, C. T. Plass, R. Domes, T. Frosch, G. Soavi, E. Wendler, Y. Zhang and Carsten Ronning, Adv. Funct. Mater. 2022, 2111338.

79 V. Türck, S. Rodt, O. Stier, R. Heitz, R. Engelhardt, U. W. Phol, D. Bimberg, and R. Steingrüber. Phys. Rev. B, 2000, 61, 9944-9947.

80 X. Lao, Z. Yang, Z. Su, Z. Wang, H. Ye, M. Wang, X. Yao and S. Xu, Nanoscale, 2018, 10, 9949-9956.

81 J. E, Parks, Department of Physics and Astronomy, The University of Tennessee, Tech. Rep., 2013.

Chapter 3 Enhanced performance on ultraviolet photodiodes by composition tuning in lead-free double perovskite nanocrystals

3.1 Introduction

It is generally known that ultraviolet (UV) radiation has a far-reaching impact on human life and production development. For instance, appropriate exposure to UV light is beneficial to the generation of vitamin D in the human body, while overexposure to UV radiation causes skin cancers and eye diseases.[1] UV photodetectors, which capture incident UV light signal and convert it into electric signal, are fundamental units of various applications including UV radiation monitoring, flame detecting, biomedical imaging, UV disinfecting, UV curing, as well as advanced optical communication.[2–5] The widely-used photosensitive materials in commercial UV photodetectors are Si and III-V compound semiconductors including SiC, GaN, and (In, Al)GaN. These types of devices exhibit superior performance.[6,7] However, high cost, complicated and strict production process make them indispensable for exploring new material-based photodetectors. Furthermore, the tunable spectral responses in photodetectors are important for a variety of applications such as spectral sensing, optical communications, biomedical imaging and spectroscopy. While it is difficult to realize by traditional semiconductor materials. Halide perovskites have emerged in recent decades due to their excellent properties such as strong light absorption, high carrier-transport efficiency, tunable bandgap, long carrier diffusion length, and being easily processed in solution.[8–12] On this basis, photodetectors based on halide perovskite have made great strides in performance enhancement and cost reduction.[13,14] Nevertheless, there are still two obstacles that hinder the application of perovskite photodetectors in human life and their commercialization in the industry: one is the instability towards moisture and heat, and another is the toxicity of lead elements.[15,16]

Recently, lead-free double perovskites such as $Cs_2AgBi(Br/Cl)_6$ and $Cs_2AgInCl_6$ have been employed in the application of photodetectors as promising candidates owing to their environmental stability and long carrier recombination lifetime.[17–19] In 2018, photodetectors based on $Cs_2AgBiBr_6$ thin films were first investigated by using the spin-coating method, the device performance of high responsivity (7.01 A/W) and specific detectivity of 5.66 x 10^{11} Jones were achieved, along with the response speed of 956/995 μs.[17] Meanwhile, $Cs_2AgInCl_6$ single crystals with low trap density were synthesized by hydrothermal method and photodetectors based on that showed a high detectivity of ~10^{12} Jones.[18] Besides solution-processed method, the vapor deposition technique was utilized in the preparation of $Cs_2AgBiCl_6$ thin film in self-powered photodetectors in 2020. And the corresponding device exhibits excellent detectivity of ~10^{12} Jones and responsivity around 10 mA/W.[19] These lead-free double perovskite photodetectors are environmentally stable and their device performance are comparable with reported UV photodetectors based on other semiconductor materials.[20–23]

Given in the easy solution processability of nanocrystals compared with thin film and bulk state, in this work, in this work, we demonstrate a high-performance photodiode based on $Cs_2Ag_{0.35}Na_{0.65}InCl_6$ perovskite nanocrystals enabled by the all-solution process. By carefully tuning the bismuth doping in nanocrystals, we achieve nanocrystals film with a stronger absorption peak. The UV photodiodes are designed and fabricated based on the spin-coated DP NC films, showing high selectivity centered at 340 nm. The device exhibits high performance with high photoresponsivity of 3.03 A/W and detectivity of ~10^{11} Jones, large light/dark current density ratio (32), and self-powered function (70 mA/W of responsivity and ~10^9 Jones of detectivity under zero bias, which compare favorably with UV photodiodes based on other double perovskite reported in the literature.[24-26]

3.2 Experimental

3.2.1 Materials and synthesis

Reagents and materials

Cesium acetate (CsOAc, 99.99%, Aldrich), silver acetate (AgOAc, 99%, Aldrich), sodium acetate (NaOAc, 99.99%, Supelco), indium(III) acetate [$In(OAc)_3$, 99.99%, Aldrich], bismuth(III) acetate [$Bi(OAc)_3$, 99.99%, Aldrich], 1-octadecene (ODE, 90%, TCI), oleylamine (OLA, 70%, Aldrich), oleic acid (OA, 90%, Aldrich), chlorotrimethylsilane (TMSCl, 98%, Aldrich), hexane (96%, Wako) and ethyl acetate (99.5%, wako) were used without further purification.

Aluminium-doped zinc oxide ink (conductivity: 10^{-3}-10^{-4} S/cm), Poly[(9,9-dioctylfluorenyl-2,7-diyl)-co-(4,4'-(N-(4-sec-butylphenyl)diphenylamine)] (TFB, M_w > 30000, Aldrich), chlorobenzene (CB, 99.5%, Aldrich) and aluminium wires (Al, φ0.50mm 99.999%, Nilaco) were used for the device preparation.

Synthesis of Bi-doped $Cs_2Ag_{0.35}Na_{0.65}InCl_6$ NCs

The synthesis of perovskite nanocrystals was performed using a reported protocol.[27,28] 1 mmol cesium acetate, 0.18 mmol silver acetate, 0.27 mmol sodium acetate, 0.5 mmol indium acetate, and bismuth acetate (0.005 mmol for DP-1, 0.025 mmol for DP-2) are were mixed with 10 mL octadecene, 0.7 mL oleylamine, and 2.8 mL oleic acid in a 50 mL three-neck flask. The flask was connected to Schlenk line, then the mixture was heated to 110 °C and degassed at 110 °C for one hour. Then the heating temperature was raised by the speed of 6 °C per minute, and when the temperature reached 165 °C, 0.4 mL TMSCl was injected into the precursor solution. After 2 minutes of continuous heating, the reaction was stopped by an ice water bath. When the temperature reached 30 °C, the reaction mixture was transferred into a centrifuge tube and centrifuged at 9000 rpm for 20 min. The supernatant was removed. Then the precipitate was dispersed in 5 mL hexane and centrifuged at 6000 rpm for 15 min, then the precipitate was discarded

and the supernatant was mixed with ethyl acetate at the volume ratio of 1:1. Following a centrifugation process at 10000 rpm for 5 min. Finally, the precipitate was redispersed in hexane at the concentration of 25 mg/mL for the device fabrication and characterization. All the centrifugations were conducted at 25 °C.

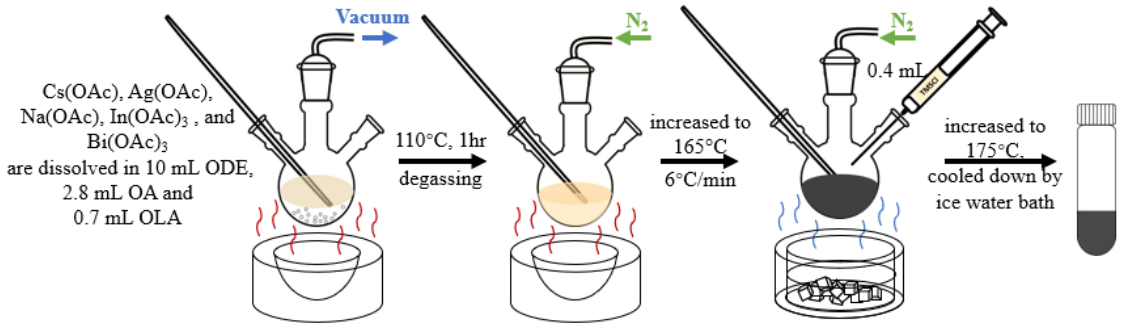

Scheme 3.1 The synthetic routine of lead-free double perovskite nanocrystals.

3.2.2 Materials characterization

The crystallinity was investigated by X-ray diffraction (XRD, MiniFlex 600 Rigaku, CuKα), where the liquid sample was dropped on the silicon plate and the solvent was evaporated. Samples were measured with the power of 0.6 kW (40 kV, 15 mA) at a step width of 0.02° (5 ° /min). Transmission electron microscopy (TEM) characterization was performed using a JEM-2100F2 instrument (JEOL) at 200 kV acceleration voltage. Scanning transmission electron microscopy coupled with energy dispersive spectroscopy (STEM-EDS, JEM-2100F2) was utilized for the element analysis. Samples for the TEM analysis was prepared by drop-casting the 0.1 mg/mL hexane solution of NCs onto carbon-coated copper grids. Elemental analysis and chemical bonding were studied by X-ray photoelectron spectroscopy (XPS, ThermoFisher), the samples for the XPS analysis are drop-casted on the silicon substrate. The absorption spectra was acquired with a JASCO V-650 UV-visible spectrometer. The highest occupied molecular orbital (HOMO) and lowest unoccupied molecular orbital (LUMO) of nanocrystals were measured by ultraviolet photoelectron spectroscopy (UPS, ThermoFisher), the samples were prepared same with the XPS samples. The work function of indium tin oxide (ITO)-coated glass

was measured by Photoelectron Yield Spectroscopy (PYS) at a photon power of 500 nW.

3.2.3 Device fabrication

A 10 × 20 mm^2 rectangle soda-lime glass covered with 150 nm thick ITO with a sheet resistance of 10~14 Ω/sq was used as the substrate. The ITO film was patterned to into a narrow strip about 2 mm wide and 20 mm long. ITO glasses were cleaned by the detergent, deionized water, isopropanol, and acetone in ultrasonic cleaner successively (30 min for each step). Next, organic contaminations on the substrate surface were removed exposure to vacuum ultraviolet (VUV) light (Ushio Inc., Japan, λ = 172 nm and 10 mW/cm^2) for 30 min under a reduced pressure of 1 kPa and N_2 flow, resulting in a super hydrophilic surface due to oxidation.[29] Then the substrates were transferred into the Ar-filled glove box where the oxygen and water levels are continuously monitored to maintain both O2 < 1 ppm and H2O <1 ppm. 70 μL of an Al-doped ZnO solution was spin-coated on ITO glassed at a rate of 1500 rpm for 45 s and annealed at 160 ºC for 30 min. The nanocrystal solution (DP-1 or DP-2) was spin-coated onto Al-doped ZnO films at 1500 rpm for 45 s and annealed at 180 ºC for 10 min. TFB solution was spin-coated onto nanocrystal films at 2500 rpm for 45 s and heated at 120 ºC for 10 min. Finally, Al electrode with a thickness of 170 nm was thermally evaporated onto TFB films under the pressure of 5 x 10^{-5} ~ 1 x 10^{-4} Pa.

3.2.4 Device measurement

The electrical characterization was done using Keithly 2425 SourceMeter and KickStart software. Compact Xenon light source (300 W, Asahi Spectra Co., Ltd, MAX-301) combined with narrow bandpass filters (310 nm, 340 nm, 365 nm and 380 nm) was used as light sources for different wavelengths. The power of UV light at different intensities was recorded using a Laser power & energy meter (Ophir Optronics Solutions Ltd, NOVA II). For the I-V test, the dark current was measured without illumination for each device, the light current was measured after each scan of dark current under the

illumination of a specific wavelength (310 nm, 340 nm, 365 nm or 380 nm) at a specific power intensity (range from 2~20 mW/cm^2) as needed. No obvious difference when we compared the dark current which was measured before the light current to that measured after the light current for same device. For the dynamic response measurement, the anode and cathode of the device were connected to a 1 GΩ load resistor and a digital oscilloscope (Iwatsu Electric Co., Ltd, DS-5624A) combined with an optical chopper (#55-783, Edmund Optics). The dynamic response displayed on the oscilloscope and the response time was extracted according to the record. All the device measurements were conducted in air and at room temperature.

3.3 Results and discussion

A schematic illustration of the hot-injection method for the synthesis of $Cs_2Ag_{0.35}Na_{0.65}InCl_6$ DP NCs is shown in **Scheme 3.1**. **Figure 3.1(a)** shows the X-ray diffraction (XRD) patterns of DP-1 and DP-2 which contain 3% and 6% molar ratios of Bi-dopant, respectively. The presence of multiple diffraction peaks exhibits the structural characteristics of the nanocrystal films. For DP-1, domain diffraction peaks at 23.9°, 29.42°, 34.06°, 42.00°, and 48.92° are assigned to (022), (222), (004), (224) and (044) diffraction planes of standard cubic double perovskite structure with a space group of Fm-3m and a lattice parameter of 10.53 Å. Other peaks are consistent with the simulated values obtained for the $Cs_2NaInCl_6$ powder and previous literature reports, confirming the formation of Bi-doped $Cs_2Ag_{0.35}Na_{0.65}InCl_6$ double perovskite via the modified hot-injection method.[27–29] Meanwhile, the careful analysis of the XRD pattern reveals a shift of all diffraction peaks towards a lower diffraction angle of DP-2 compared to DP-1. For example, the (044) diffraction peak is shifted from 48.92° to 48.82°. The shifts in diffraction peak indicate that the larger amount of the incorporation of bigger Bi^{3+} ion (1.03 Å) in place of smaller In^{3+} ion (0.8 Å) induces the lattice expansion. The lattice parameter expanded from 10.53 Å to 10.56 Å. The transmission electron microscopy (TEM) image ang with the size distribution of both DP-1 and DP-2 are supplied in **Figure**

3.1(b, (c), the average sizes are 13.52 ± 2.5 nm and 14.16 ± 2.7 nm for DP-1 and DP-2, respectively. It could be observed that the nanocrystals show a clear cubic shape and uniform distribution, which is consistent with the XRD results. The crystalline size is also appropriate for the preparation of thin film and is potentially further applied in optoelectronic devices.

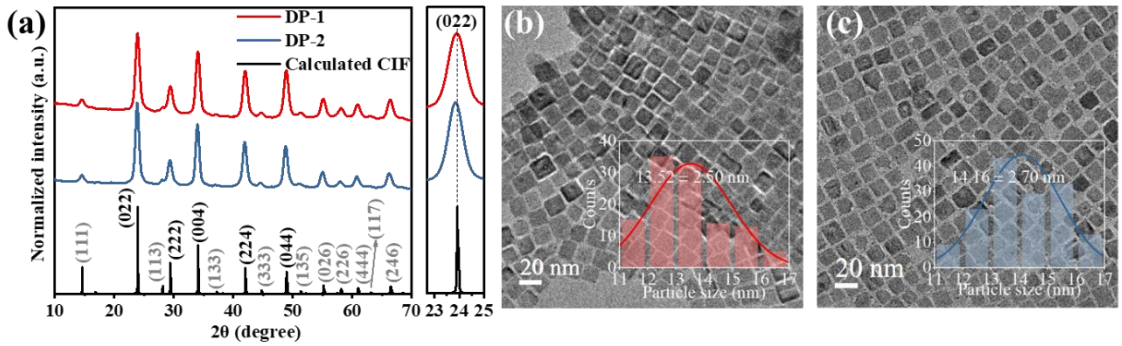

Figure 3.1. (a) The X-ray diffraction (XRD) pattern of DP-1 and DP-2 with thin-film from, and the enlarged XRD patterns for clear visualization of (044) diffraction peak. Transmission electron microscopy (TEM) images of (b) DP-1 and (c) DP-2. The scale bar is 20 nm. The inset figures are the size distribution histogram of DP-1 and DP-2.

Quantitative analysis of the electronic structures and chemical properties of Bi-doped $Cs_2Ag_{0.35}Na_{0.65}InCl_6$ double perovskite nanocrystals has been performed by the combination of XPS and STEM-EDS analysis, and the binding energies of XPS spectra were calculated after calibrating the shift in the binding energy of C 1s edge as the reference. XPS analysis has been conducted to understand the occupancy of the elements more accurately in the doped double perovskite materials. **Figure 3.2** illustrate the survey and high-resolution XPS spectra of DP-1 and DP-2. As shown, the peaks corresponding to cesium [Cs 3d], silver [Ag 3d], indium [In 3d], bismuth [Bi 4f], and chlorine [Cl 2p] appear in the DP-1 and DP-2, while the signal of sodium [Na 1s] is too weak to detect by this instrument. In **Figure 3.2(b)**, two strong peaks were observed for the narrow spectra of Cs-3d. For DP-1, the peak at 738.7 eV is due to Cs 3d3/2 and the peak at 724.6 eV is due to Cs 3d5/2 consistent with the standard Cs element. The two peaks have an energy difference of 14.1 eV. The spectra of Ag 3d consist of two peaks at 374.3 eV and 368.5

eV associated with Ag 3d3/2 and Ag 3d5/2, respectively. The In 3d spectra are composed of two peaks at 453.7 eV and 446.1 eV originating from In 3d3/2 and In 3d5/2, respectively (**Figure 3.2(d)**). **Figure 3.2(e)** shows that Bi 4f has two peaks with binding energies of 159.1 eV and 153.4 eV which are related to Bi 4f5/2 and 4f7/2, respectively. Compared DP-2 to DP-1, the peak of Cs 3d, In 3d, Bi 4f, and Cl 2p have a slight shift or no shift, while the peak of Ag 3d shifts toward lower binding energy, and the offset is 1.1 eV for Ag 3d5/2, which means the higher doping amount of Bi^{3+} induces the weaker Ag-Cl interaction in the $[AgCl_6]^{5-}$ octahedra. These results confirm the effective doping of bismuth in DP-1 and DP-2.

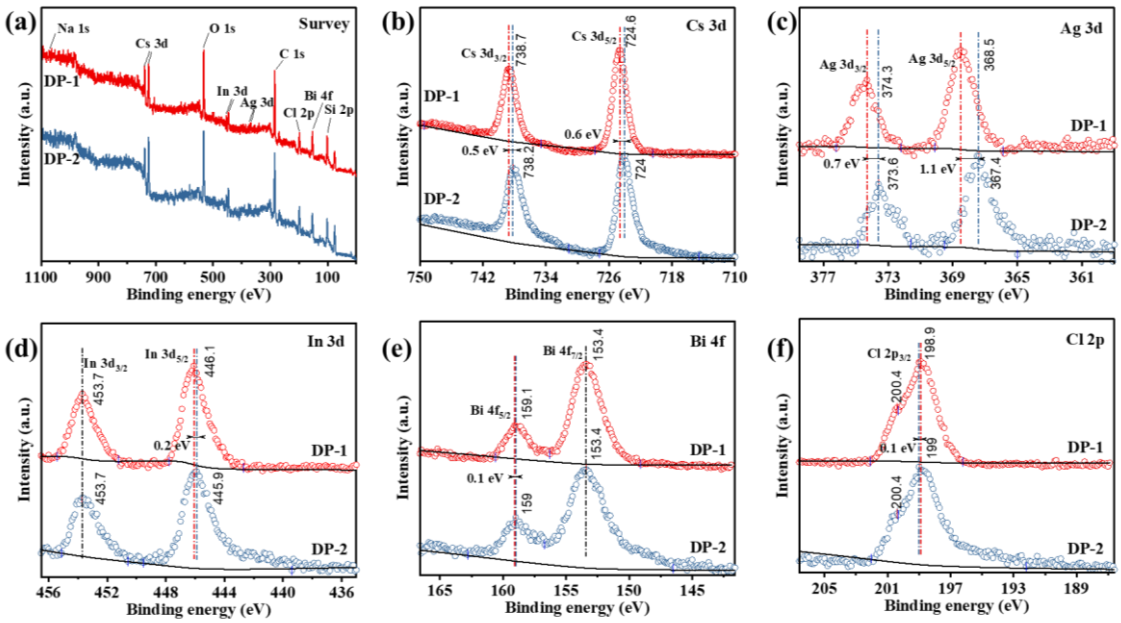

Figure 3.2. XPS spectra of (a) wide scan, (b) Cs 3d, (c) Ag 3d, (d) In 3d, (e) Bi 4f and (f) Cl 2p core level obtained for DP-1 (red) and DP-2 (blue). All the spectra are calibrated to 285 eV, corresponding to a C 1s peak.

The ultraviolet-visible (UV-Vis) absorption is measured to evaluate the optical properties and light absorption capability of the spin-coated DP nanocrystal film. The spectrum was characterized by one typical absorption peak and a photo-response range between 320 and 380 nm for both DP-1 and DP-2, as shown in **Figure 3.3(a)**. The sharp absorption peak accounts for the effective absorption of photons, which is responsible for

the capture of large photocurrents of the photodetectors based on DP-1 and DP-2. The exciton peak at around 340 nm is originated from the band-edge absorption and it was proved that the intensity of this exciton peak could be enhanced by the increase in bismuth doping concentration.[30] The optical bandgaps of the DP-1 and DP-2 film are 3.35 and 3.29 eV which are estimated from the absorption spectra by using Tauc's plot method,[31,32] as shown in the inset of **Figure 3.3(a)**, red and blue dash lines are the tangent lines of the $(\alpha hv)^{1/n}$, where α is the absorption coefficient, h is Plank's constant, v is the frequency of light, and the index n = 1/2 is related to the bandgap of directly allowed transition semiconductors. The decrease in band gap of DP-2 suggests that DP-2 is more suitable for photodiode applications. We further determine the valence band minimum (VBM) and conduction band maximum (CBM) of the materials using ultraviolet photoelectron spectroscopy (UPS). We measure the binding energy of 0.84 eV and cutoff energy of 16.18 eV (**Figure 3.3(b)**), from which we estimate the VBM and CBM of DP-1 to be 5.88 and 2.53 eV, and that of DP-2 to be 5.68 and 2.39 eV, respectively (as shown in **Figure 3.4**). The photoluminescence (PL) and PL excitation (PLE) spectrum of DP-1 and DP-2 are shown in **Figure 3.5**, the PL peak of DP-2 is red-shifted from that of DP-1. The time-resolved photoluminescence (TRPL) traces at 368 nm excitation wavelength are shown in **Figure 3.5(c)**, and the average lifetimes for the DP-1 and DP-2 are 0.08 and 0.37 μs, which is consistent with our previous study.[28]

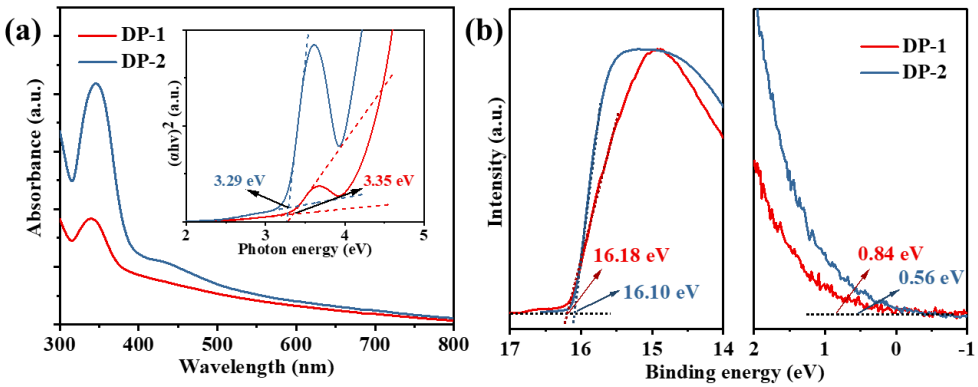

Figure 3.3 (a) UV-Vis spectra and Tauc plot of DP-1 and DP-2 thin film. (b) UPS spectra of DP-1 and DP-2 thin film measured under the bias voltage of -10 V. The left shows the cutoff of

energy, and the right figure shows the enlarged spectral parts near the Fermi edge.

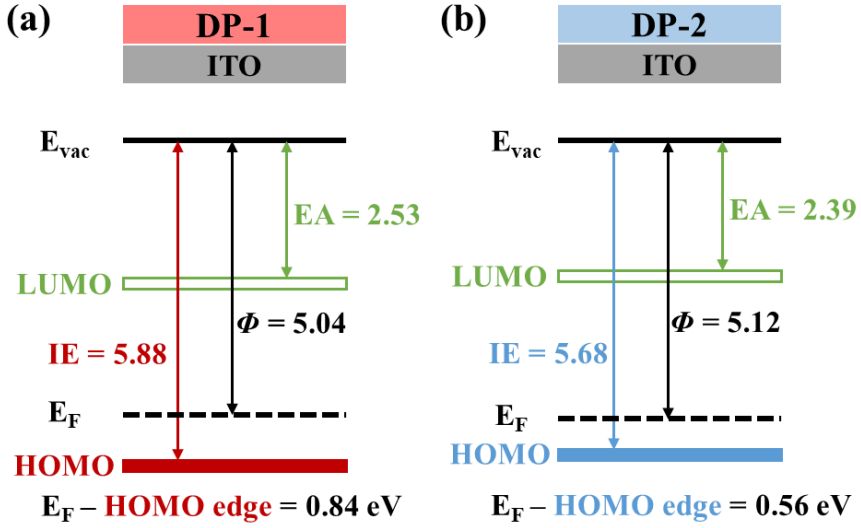

Figure 3.4. Energy level diagrams showing the results of UPS for DP-1 (a) and DP-2 (b) on an ITO substrate.

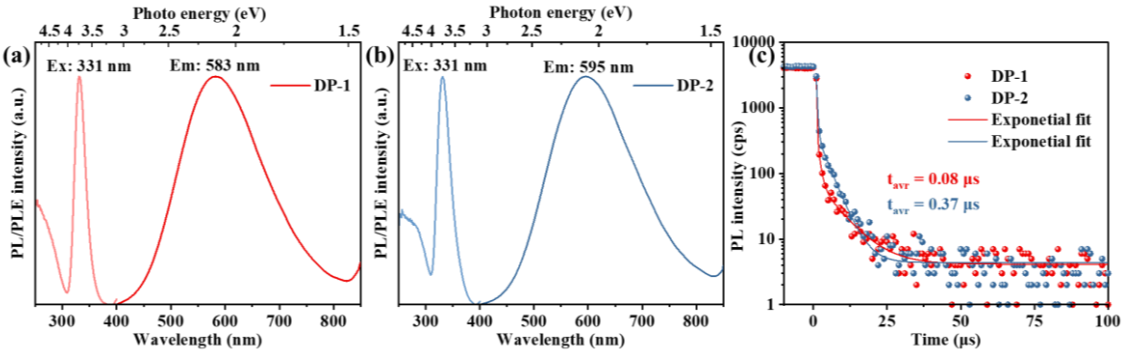

Figure 3.5. Photoluminescence (PL) and PL excitation (PLE) spectra of DP-1 (a) and DP-2 (b) thin film. The optimal excitation wavelength for both samples is 331 nm. (c) PL lifetime of DP-1 (red) and DP-2 (blue) thin film.

Table 3.1 Decay parameters of DP-1 and DP-2 at room temperature [a]

Sample	τ_1 (a_1)	τ_2 (a_2)	τ_{avg}	R-square
DP-1	0.78 μs (87.32%)	13.65 μs (12.68%)	0.89 μs	0.985

DP-2	0.97 μs (78.34%)	6.55 μs (21.66%)	1.18 μs	0.981

[a]PL lifetime was biexponential fitted by the following formula:

$$I(t) = A_1 e^{-t/\tau_1} + A_2 e^{-t/\tau_2}$$

where t indicates time, $I(t)$ is the PL intensity at t μs, A_1 and A_2 are the amplitude of component 1 and 2, τ_1 and τ_2 are the lifetime of component 1 and 2. a_1 and a_2 are the fractional for component 1 and 2, which are calculated by $a = \frac{A_i\tau_i}{\sum A_i\tau_i}$; τ_{avg} indicates the amplitude average lifetime, which is calculated by $\tau_{ave} = A_1\tau_1 + A_2\tau_2$.

In order to explore the ultraviolet sensing potential of the $Cs_2Ag_{0.3}5Na_{0.65}InCl_6$: Bi nanocrystals, we have fabricated UV photodiodes using the double perovskite nanocrystals. The device architecture of ITO/ZnO: Al/DP-1 or DP-2/TFB/Al is employed for further investigation, as shown in **Figure 3.6**, as well as the corresponding energy level of each functional layer. In this device structure, the built-in electric field is generated and both electrons and holes would extract and transported efficiently through the interface layer. To verify the formation of each layer, cross-section SEM images are shown in **Figure 3.6**, so that the thickness of the device is confirmed, which is close between the two devices based on DP-1 and DP-2. Then we evaluate the performance of UV photodiodes based on DP-1 and DP-2.

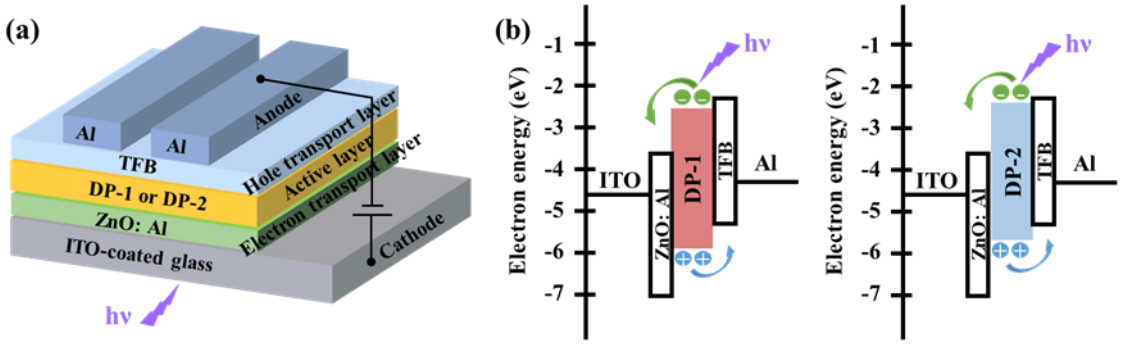

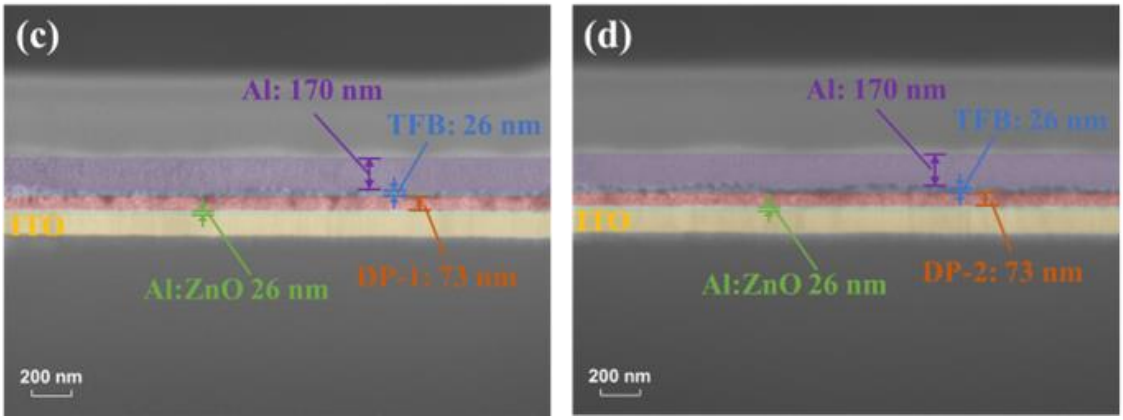

Figure 3.6 (a) Device configuration of photodiodes based on DP-1 and DP-2. (b) The energy level which is corresponding to the device structure in the left. The green and blue arrows indicate the moving direction of electron and hole, respectively. Cross-sectional SEM images of the photodiodes based on DP-1 (c) and DP-2 (d).

Figure 3.7(a)-(d) represent the current density-voltage (J-V) characteristics of the device based on DP-1 and DP-2 under dark and light illumination of 20 mW/cm^2, respectively. The current density increases with the relatively small bias (less than 0.5 V). Under a bias voltage (V) of 0 V, the DP-1 based device shows a light/dark current density ratio of 3.37, while the device based on DP-2 exhibits a light/dark current density ratio of 32. The data clearly show that there is a significant increase in the photocurrent generated from the device upon light illumination. The result indicated that the separated electrons and holes in the DP-2-based device can be much more effectively extracted to form the photocurrent, which is consistent with stronger absorption of DP-2 at 340 nm compared with DP-1.

Device responsivity and detectivity are figure of merit of photodiode devices, the photoresponsivity (R) is closely related to the quantum yield of photodiodes and is defined as follows,[38,39]

$$R = (I_{light}-I_{dark})/P_{in}A \quad (1)$$

Where I_{light}, I_{dark}, P_{in}, and A are photocurrent, dark current, incident light density and

active area, respectively. Meanwhile, the detectivity (D) reflects the ability of detecting weak signals. When the dark current is dominated by shot noise, it can be related to the responsivity by the following formula,[38,39]

$$D = R/(2qJ_{dark})^{1/2} \quad (2)$$

Where R is the responsivity, q is the unit charge, and J_{dark} is the dark current density. **Figure 3.7(b), (e)** show the responsivity and the detectivity of the devices as a function of the incident light intensity of the 340 nm UV source. With a constant 0.5 V bias across the devices, the peak responsivity of PD based on DP-1 and DP-2 are determined to be 0.58 A/W and 3.03 A/W when the light intensity is 3.5 mW/cm^2. And the corresponding specific detectivities are 1.68 x 10^{10} and 1.29 x 10^{11} Jones for PD based on DP-1 and DP-2, respectively, which are calculated from formula (2). For both two devices, their responsivities and detectivities decrease as the incident light intensity increases, which might be attributed to that more carriers are trapped by defects when photogenerated carriers increase and further resulting in more carriers being wasted.[40] The device exhibits good photoresponsivity between 310 and 380 nm in the UV-A, as shown in **Figure 3.7 (c)(f)**. It shows the wavelength-dependent responsivity and detectivity of PD based on DP-1 and DP-2 with the incident light intensity of 20 mW/cm^2, the characteristic of the curves is well consistent with the absorption spectra of DP-1 and DP-2, respectively. The UV-Vis spectra of each layer in PD are shown in **Figure 3.8**. For the device based on DP-1, we obtained a detectivity of 5.67 x 10^9 Jones as well as a responsivity of 0.21 A/W at 340 nm. After we enhance the absorbance by tuning the bismuth doping concentration, the performance of the device based on DP-2 is enhanced as follows, a detectivity of 3.65 x 10^{10} Jones and the peak responsivity of 1.13 A/W at 340 nm are achieved. We note that this value of responsivity is comparable of the other lead-based perovskite UV photodiodes or photodetectors,[41–43] which demonstrates the advantage of DP NC films in the application of UV detection.

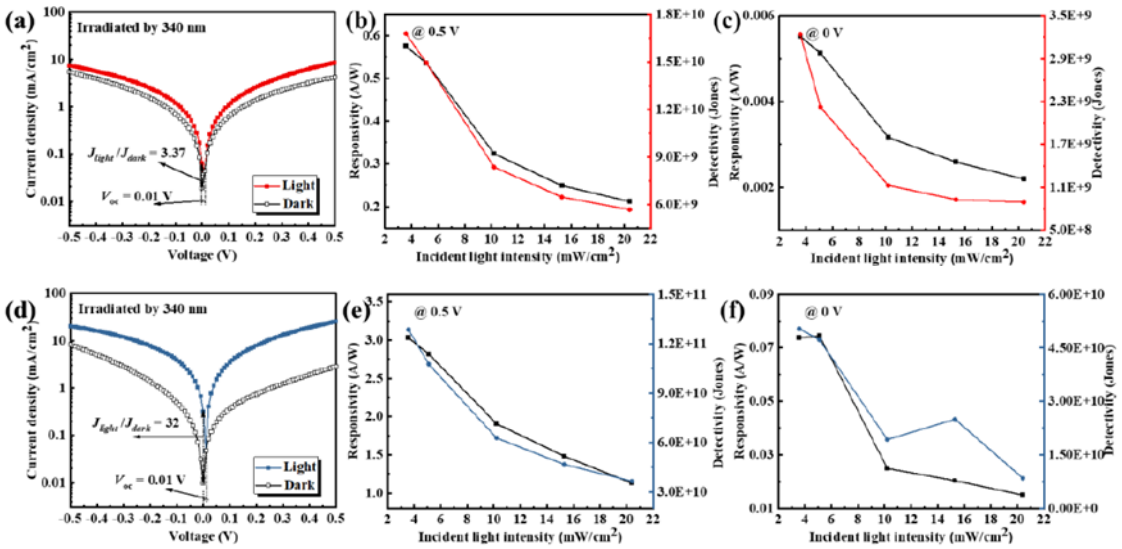

Figure 3.7 The current density versus applied voltage of PD based on DP-1 (a) and DP-2 (b); The responsivity and detectivity as a function of incident light intensity at an applied voltage of 0.5 V of PD based on DP-1 (c) and DP-2 (d) as well as the results at zero voltage of PD based on DP-1 (e) and DP-2 (e).

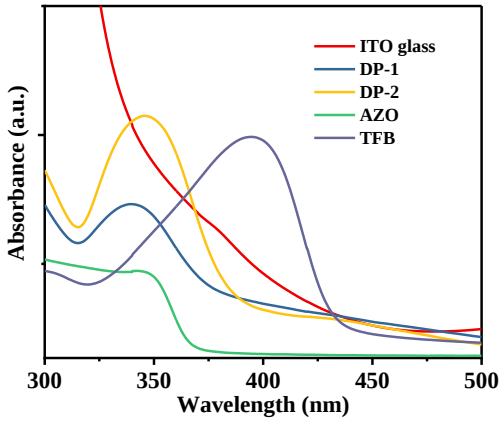

Figure 3.8 UV-Vis of each layer in photodiode.

Specifically, the device performance as shown in **Figure 3.9 (a), (b)** indicates that our device can work efficiently in self-powered mode. **Figure 3.10** shows the dynamic current-time (I-t) response of the photodiodes under the periodical illumination of 340 nm UV light. The ON and OFF states exhibit consistent performance as a reversible and rapid switch from illumination to dark for 2 s. The rise/fall time of the photodiode is

defined as the time taken for the device response to rise/fall from 10%/90% to 90%/10% of its maximum value.[44] It can be extracted that the rise/fall time of PD based on DP-1 and DP-2 are 14/46 ms and 16/13 ms, the fast response times depend that the photodiodes extract photogenerated charge carriers efficiently.[44]

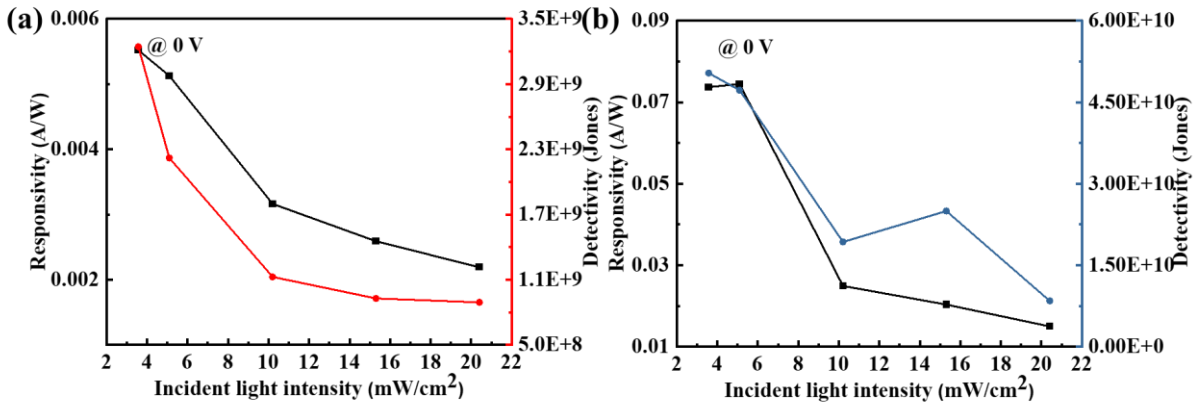

Figure 3.9 Responsivity and detectivity versus incident light intensity of PD based on DP-1 (a) and DP-2 (b) with the applied voltage of 0 V.

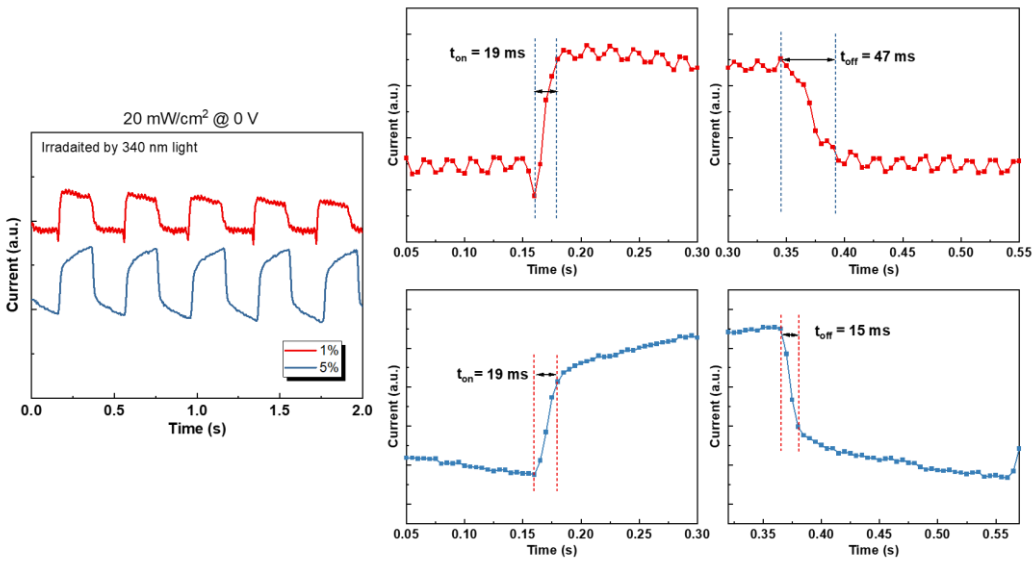

Figure 3.10 The dynamic current-time response of the PD based on DP-1 (red line) and DP-2 (blu-line). The rise and decay time were estimated by the time reaching or dropping the 90% of peak intensity of current.

3.4 Conclusion

Halide perovskites stand out as promising materials for realizing high-performance photodetectors. However, the inherent instability and the lead toxicity are still obstacles facing the wide practical application of photodetectors. In this work, the first highly responsive lead-free perovskite photodiode based on $Cs_2Ag_{0.35}Na_{0.65}InCl_6$ nanocrystals is demonstrated. The composition tuning strategy is introduced to enhance the device performance of photodiodes. Employed with a device structure composed of ZnO: Al electron-transport layer and TFB hole transport layer, lead-free perovskite nanocrystal photodiodes exhibit a high responsivity of 3.03 A/W and specific detectivity of 1.29 x 10^{11} Jones under the illumination of a 340 nm light source. Moreover, UV photodiodes show good performance under the self-powered mode, which exhibits the responsivity of 0.07 A/W and specific detectivity of 5.04 x 10^{10} Jones. Our work verifies the great potential of the $Cs_2Ag_{0.35}Na_{0.65}InCl_6$ nanocrystals in the application of environmentally friendly and high-performance UV photodiodes.

References

1. Gallagher, R. P. & Lee, T. K. Adverse effects of ultraviolet radiation: A brief review. Progress in Biophysics and Molecular Biology vol. 92 119–131 (2006).

2. Zhang, Z. et al. Ultraviolet Photodetectors Based on Polymer Microwire Arrays toward Wearable Medical Devices. ACS Appl. Mater. Interfaces 14, 41257–41263 (2022).

3. Kumar, M., Park, J.-Y. & Seo, H. High-Performance and Self-Powered Alternating Current Ultraviolet Photodetector for Digital Communication. ACS Appl. Mater. Interfaces 13, 12241–12249 (2021).

4. Chen, J., Ouyang, W., Yang, W., He, J. & Fang, X. Recent Progress of Heterojunction Ultraviolet Photodetectors: Materials, Integrations, and Applications. Adv. Funct. Mater. 30, 1909909 (2020).

5. Al Fattah, M. F. et al. Sensing of ultraviolet light: a transition from conventional to

self-powered photodetector. Nanoscale 13, 15526–15551 (2021).

6. Monroy, E., Omn s, F. & Calle, F. Wide-bandgap semiconductor ultraviolet photodetectors. Semicond. Sci. Technol. 18, R33–R51 (2003).

7. Sang, L., Liao, M. & Sumiya, M. A comprehensive review of semiconductor ultraviolet photodetectors: From thin film to one-dimensional nanostructures. Sensors (Switzerland) vol. 13 10482–10518 (2013).

8. Bao, C. et al. High Performance and Stable All-Inorganic Metal Halide Perovskite-Based Photodetectors for Optical Communication Applications. Adv. Mater. 30, 1803422 (2018).

9. Lim, J. et al. Elucidating the long-range charge carrier mobility in metal halide perovskite thin films. Energy Environ. Sci. 12, 169–176 (2019).

10. Ahmed, G. H., Yin, J., Bakr, O. M. & Mohammed, O. F. Successes and Challenges of Core/Shell Lead Halide Perovskite Nanocrystals. ACS Energy Lett. 6, 1340–1357 (2021).

11. Otero-Martínez, C. et al. Fast A-Site Cation Cross-Exchange at Room Temperature: Single-to Double- and Triple-Cation Halide Perovskite Nanocrystals. Angew. Chemie Int. Ed. 61, (2022).

12. Xu, L. et al. Charge-carrier dynamics and regulation strategies in perovskite light-emitting diodes: From materials to devices. Appl. Phys. Rev. 9, 21308 (2022).

13. Yun, Y. et al. A Wide Bandgap Halide Perovskite Based Self-Powered Blue Photodetector with 84.9% of External Quantum Efficiency. Adv. Mater. 34, 2206932 (2022).

14. Liu, Y. et al. High-Performance Self-Powered Photodetectors with Space-Confined Hybrid Lead Halide Perovskite Nanocrystals. Adv. Opt. Mater. 2202215 (2022) doi:10.1002/adom.202202215.

15. Xiao, Z. et al. Thin-film semiconductor perspective of organometal trihalide

perovskite materials for high-efficiency solar cells. Mater. Sci. Eng. R Reports 101, 1–38 (2016).

16. Babayigit, A., Ethirajan, A., Muller, M. & Conings, B. Toxicity of organometal halide perovskite solar cells. Nat. Mater. 15, 247–251 (2016).

17. Lei, L.-Z. et al. High-efficiency and air-stable photodetectors based on lead-free double perovskite Cs2AgBiBr6 thin films. J. Mater. Chem. C 6, 7982–7988 (2018).

18. Luo, J. et al. Cs2AgInCl6 Double Perovskite Single Crystals: Parity Forbidden Transitions and Their Application For Sensitive and Fast UV Photodetectors. ACS Photonics 5, 398–405 (2018).

19. Wang, M., Zeng, P., Wang, Z. & Liu, M. Vapor‐Deposited Cs2AgBiCl6 Double Perovskite Films toward Highly Selective and Stable Ultraviolet Photodetector. Adv. Sci. 7, 1903662 (2020).

20. Gong, M. et al. All-Printable ZnO Quantum Dots/Graphene van der Waals Heterostructures for Ultrasensitive Detection of Ultraviolet Light. ACS Nano 11, 4114–4123 (2017).

21. Peng, W. et al. Enhanced Performance of a Self-Powered Organic/Inorganic Photodetector by Pyro-Phototronic and Piezo-Phototronic Effects. Adv. Mater. 29, 1606698 (2017).

22. Zhao, B. et al. An Ultrahigh Responsivity (9.7 mA W−1) Self-Powered Solar-Blind Photodetector Based on Individual ZnO–Ga2O3 Heterostructures. Adv. Funct. Mater. 27, 1700264 (2017).

23. Dong, Y. et al. Self-powered fiber-shaped wearable omnidirectional photodetectors. Nano Energy 30, 173–179 (2016).

24. Zhang, X. et al. Ultrafast, Self-Powered, and Charge-Transport-Layer-Free Ultraviolet Photodetectors Based on Sequentially Vacuum-Evaporated Lead-Free Cs2AgBiBr6 Thin Films. ACS Appl. Mater. Interfaces 13, 35949–35960 (2021).

25. Li, H. et al. A Highly Stable Photodetector Based on a Lead-Free Double Perovskite

Operating at Different Temperatures. J. Phys. Chem. Lett. 12, 5682–5688 (2021).

26. Shen, W., Jung, U., Xian, Z., Jung, B. & Park, J. Enhanced device performance of Cs2AgBiBr6 double perovskite photodetector by SnO2/ZnO double electron transport layer. J. Alloys Compd. 929, 167329 (2022).

27. Han, P. et al. Lead-Free Sodium–Indium Double Perovskite Nanocrystals through Doping Silver Cations for Bright Yellow Emission. Angew. Chemie - Int. Ed. 58, 17231–17235 (2019).

28. Huang, X., Matsushita, Y., Sun, H.-T. & Shirahata, N. Impact of bismuth-doping on enhanced radiative recombination in lead-free double-perovskite nanocrystals. Nanoscale Adv. 4, 3091–3100 (2022).

29. Shirahata, N., Yonezawa, T., Seo, W.-S. & Koumoto, K. Photoinduced Cleavage of Alkyl Monolayers on Si. Langmuir 20, 1517–1520 (2004).

30. Noculak, A. et al. Bright Blue and Green Luminescence of Sb(III) in Double Perovskite Cs2MInCl6 (M = Na, K) Matrices. Chem. Mater. 32, 5118–5124 (2020).

31. Yang, B. et al. Lead-Free Silver-Bismuth Halide Double Perovskite Nanocrystals. Angew. Chemie Int. Ed. 57, 5359–5363 (2018).

32. Manna, D., Das, T. K. & Yella, A. Tunable and Stable White Light Emission in Bi3+-Alloyed Cs2AgInCl6 Double Perovskite Nanocrystals. Chem. Mater. 31, 10063–10070 (2019).

33. Tauc, J., Grigorovici, R. & Vancu, A. Optical Properties and Electronic Structure of Amorphous Germanium. Phys. status solidi 15, 627–637 (1966).

34. Makuła, P., Pacia, M. & Macyk, W. How To Correctly Determine the Band Gap Energy of Modified Semiconductor Photocatalysts Based on UV–Vis Spectra. J. Phys. Chem. Lett. 9, 6814–6817 (2018).

35. Nemoto, K., Watanabe, J., Yamada, H., Sun, H.-T. & Shirahata, N. Impact of coherent core/shell architecture on fast response in InP-based quantum dot photodiodes. Nanoscale Adv. 5, 907–915 (2023).

36. Han, Y. J., An, K., Kang, K. T., Ju, B.-K. & Cho, K. H. Optical and Electrical Analysis

of Annealing Temperature of High-Molecular Weight Hole Transport Layer for Quantum-dot Light-emitting Diodes. Sci. Rep. 9, 10385 (2019).

37. Yip, H.-L. & Jen, A. K.-Y. Recent advances in solution-processed interfacial materials for efficient and stable polymer solar cells. Energy Environ. Sci. 5, 5994–6011 (2012).

38. Gong, X. et al. High-Detectivity Polymer Photodetectors with Spectral Response from 300 nm to 1450 nm. Science (80-.). 325, 1665–1667 (2009).

39. Xie, Y. et al. Broad-Spectral-Response Nanocarbon Bulk-Heterojunction Excitonic Photodetectors. Adv. Mater. 25, 3433–3437 (2013).

40. Lin, Z. et al. Enhanced Photodetection Range from Visible to Shortwave Infrared Light by ReSe2/MoTe2 van der Waals Heterostructure. Nanomaterials vol. 12 (2022).

41. Wu, C. et al. Highly Efficient and Stable Self-Powered Ultraviolet and Deep-Blue Photodetector Based on Cs 2 AgBiBr 6 /SnO 2 Heterojunction. Adv. Opt. Mater. 6, 1800811 (2018).

42. Zheng, Z. et al. Decorating Perovskite Quantum Dots in TiO2 Nanotubes Array for Broadband Response Photodetector. Adv. Funct. Mater. 27, 1703115 (2017).

43. Zhou, Y. et al. Halide-exchanged perovskite photodetectors for wearable visible-blind ultraviolet monitoring. Nano Energy 100, 107516 (2022).

44. Ward, M. D. et al. Best practices in the measurement of circularly polarised photodetectors. J. Mater. Chem. C 10, 10452–10463 (2022).

45. Bube, R. H. Trap Density Determination by Space-Charge-Limited Currents. J. Appl. Phys. 33, 1733–1737 (1962).

Chapter 4 The influence of electron transport layer in lead-free double perovskite nanocrystals-based ultraviolet photodiodes

4.1 Introduction

Recent years, metal halide perovskites (MHPs) synthesized by a simple solution process have demonstrated suitability in high-performance visible photodetectors [1–5] due to their large light absorption coefficients, high carrier mobility, long carrier diffusion lengths, and broad spectrum of light absorption. [6–10] Despite the great advantages of MHPs, the lead toxicity and poor stability of some compositions have encouraged researchers to find lead-free alternatives. To eliminate the toxicity of MHPs, the $A_2M^+M^{3+}X_6$ chemical formula materials such as $Cs_2AgBiCl_6$, [11] $Cs_2AgBiBr_6$, [12] $Cs_2AgInCl_6$, [13] and $Cs_2AgSbCl_6$ [14] were suggested as a promising strategy to replace two divalent Pb^{2+} ions with one monovalent ion M^+ and a trivalent ion M^{3+}. [15,16] These double perovskites possess tunable band gaps, low carrier effective masses, and high conductivity to efficiently transport and extract charges similar to lead-based perovskites. [17–19] The excellent properties make the double perovskite applied in various research fields, such as LED, photo detection, memory, and solar cell. [11,20–22] Among the suggested double perovskites, $Cs_2AgBiCl_6$ and $Cs_2AgBiBr_6$ has been recognized as favorable candidates for visible absorption layers in photoelectronic devices due to their excellent structural stability, long carrier recombination lifetime with thermal and humidity stability. [23,24] These research results further confirm that lead-free halide perovskites are one of the most popular directions in perovskite- based optoelectronic devices. However, $Cs_2AgBiBr_6$ and $Cs_2AgBiCl_6$ have natural hindrance factors that limit the performance of optoelectronic devices due to their large exciton binding energy of 220 meV, [25] and 333 meV [26] and energy band mismatch with electron transport layer materials, which leads to non-radiative recombination and a large energy loss at the surface. Therefore, it is crucial

to select and adopt proper electron transfer layers (ETLs) with high mobility, low-defect state, and a suitable energy level arrangement for accelerating injection and transport of electrons to enhance the device performances of perovskite-based photodetectors. Until recently, the ETL materials in perovskite photodetectors were generally metal oxides such as ZnO, TiO_2, and SnO_2. [27–29] Zhang et al. reported that modifying the number of layers ZnO to change the hydrophobicity, thereby fabricated the pinhole-free high efficiency perovskite solar cells.[30] Although ZnO is usually used as an ETL material due to its high electron mobility and low fabrication temperature, the hydrophobic surface property of ZnO gives rise to a poor coverage film by creating pinholes.[31,32] In addition, the mismatched energy levels between the perovskite film and the ZnO ETL caused a large energy loss.[33,34] To overcome these challenges, interface engineering at the heterojunction involves the construction of a bilayer or multi- layered ETL as a very critical technique.[35,36] For strategically constructed double ETLs with ZnO, we selected the PCBM, which has better band alignment with the double perovskite absorption layer.[33]

In this study, we fabricated a $Cs_2AgBiBr_6$ NCs-based photodiode with a PCBM/ZnO structure as double ETL layers and investigated the effects of double ETLs on the enhancement of device performance. The insertion of polymer PCBM between ZnO and perovskite nanocrystals allows formation of films with more well-matched energy levels for efficient electron transport. The $Cs_2AgBiBr_6$ NCs-based photodiode with PCBM/ZnO double ETLs exhibited outstanding detection performance compared to that of the single ETL device. The optimized photodiode exhibited a good self-powered performance which acted as the responsivity of 3.1 mA/W when detectivity approached 8.91×10^{10} Jones, and a large light/dark current ratio near 200 was obtained. More importantly, spectral wavelength selectivity of $Cs_2AgBiBr_6$ NCs-based photodetector manifested the potential utilization in ultraviolet detecting.

4.2 Experimental

4.2.1 Synthesis of $Cs_2AgBiCl_6$ and $C_2AgBiBr_6$ nanocrystals

Cesium acetate (CsOAc, 99.99%, Aldrich), silver acetate (AgOAc, 99%, Aldrich), bismuth(III) acetate (Bi(OAc)3, 99.99%, Aldrich), 1-octadecene (ODE, 90%, TCI), oleylamine (OLA, 70%, Aldrich), oleic acid (OA, 90%, Aldrich), chlorotrimethylsilane (TMCS, 98%, Aldrich), trimethylbromosilane (TMBS, 97%, Aldrich), hexane (96%, Wako) and ethyl acetate (99.5%, wako) were used without further purification.

The synthesis of nanocrystals was performed using a reported protocol. [37,38] 1 mmol CsOAc, 0.45 mmol AgOAc and 0.5 mmol $Bi(OAc)_3$ were mixed with 10 mL ODE, 0.7 mL OLA and 2.8 mL OA on a 50 mL three-neck flask. The flask was connected to Schlenk line, then the mixture was heated to 110 °C and degassed for an hour. Then the heating temperature was raised by the speed of 6 °C/min, and when the temperature reached 165 °C, 0.4 mL TMCS was injected into the precursor solution. After 2 min of continuous heating, the reaction was stopped by an ice water bath. When the temperature reached 30 °C, the reaction mixture was transferred into a centrifuge tube and centrifuged at 9000 rpm for 20 min. The supernatant was removed. Then the precipitate was dispersed in 5 mL hexane and centrifuged at 6000 rpm for 15 min, then the precipitate was discarded and the supernatant was mixed with ethyl acetate at the volume ratio of 1:1. Following a centrifugation process at 10000 rpm for 5 min. Finally, the precipitate was redispersed in hexane at the concentration of 25 g/mL for the device fabrication and characterization. All the centrifugatios were conducted at 25 °C.

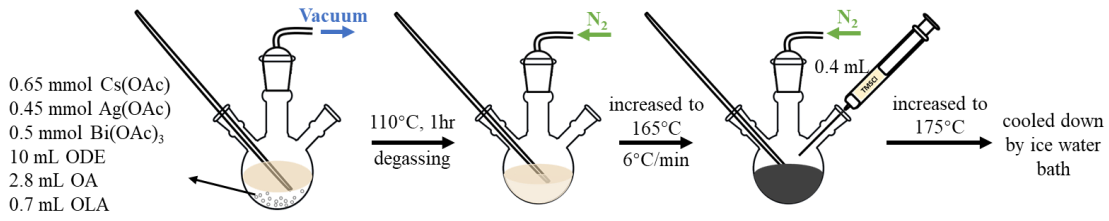

Scheme 4.1 The synthetic routine of $Cs_2AgBiCl_6$ nanocrystals.

4.2.2 Materials characterization

The crystallinity was investigated by X-ray diffraction (XRD, Rigaku, Cu Kα1), where the liquid sample was dropped on the silicon sample holder. Transmission electron microscopy (TEM) characterization was performed using a JEM-2100F2 instrument (JEOL) at 200 kV acceleration voltage. Scanning transmission electron microscopy coupled with energy dispersive spectroscopy (STEM-EDS) was utilized for the element analysis. Samples for the TEM analysis were prepared by drop-casting the 0.1 mg/mL hexane solution of NCs onto carbon-coated copper grids. Elemental analysis and chemical bonding were studied by X-ray photoelectron spectroscopy (XPS, ThermoFisher), the samples for the XPS analysis are drop-casted on the silicon substrate. The absorption spectra was acquired with a JASCO V-650 UV-visible spectrometer. The LUMO and HOMO of nanocrystals were measured by ultraviolet photoelectron spectroscopy (UPS, ThermoFisher), the samples were prepared same with the XPS samples.

4.2.3 Device fabrication

A 10 x 20 mm^2 rectangle soda-lime glass covered with 150 nm thick ITO with a sheet resistance of 10~14 Ω/sq was used as the substrate. The ITO film was patterned to into a narrow strip about 2 mm wide and 20 mm long. ITO glasses were cleaned by the detergent, deionized water, isopropanol, and acetone in ultrasonic cleaner successively (30 min for each step). Next, organic contaminations on the substrate surface were removed exposure to vacuum ultraviolet (VUV) light (Ushio Inc., Japan, λ = 172 nm and 10 mW/cm^2) for 30 min under a reduced pressure of 1 kPa and N_2 flow, resulting in a super hydrophilic surface due to oxidation. [39] Then the substrates were transferred into the Ar-filled glove box where the oxygen and water levels are continuously monitored to maintain both O_2 < 1 ppm and H_2O < 1 ppm.. 70 μL of an PEDOT:PSS solution was spin-coated on ITO glassed at a rate of 3000 rpm for 45 s and annealed at 150 °C for 30 min. The nanocrystal solution ($Cs_2AgBiCl_6$ or $Cs_2AgBiBr_6$ NCs) was spin-coated onto PEDOT:PSS films at

1500 rpm for 45 s and annealed at 180 ^{o}C for 10 min. PCBM solution was spin-coated onto nanocrystal films at 2500 rpm for 45 s and heated at 120 ^{o}C for 10 min. Next, ZnO solution was spin-coated at 2500 rpm for 45 s and heated at 140 ^{o}C for 30 min. Finally, Al electrode with a thickness of 170 nm was thermally evaporated onto ZnO films under the pressure of 5 x 10^{-5} ~ 1 x 10^{-4} Pa.

4.2.4 Device measurement

The electrical characterization was done using Keithly 2425 SourceMeter and KickStart software. Compact Xenon light source (300 W, Asahi Spectra Co., Ltd, MAX-301) combined with narrow bandpass filters (310, 34, 365, 380, 410, 440, 470 and 490 nm) was used as light sources for different wavelengths. The power of UV light at different intensities was recorded using a Laser power & energy meter (Ophir Optronics Solutions Ltd, NOVA II). For the I-V test, the dark current was measured without illumination for each device, the light current was measured after each scan of dark current under the illumination of a specific wavelength (310, 34, 365, 380, 410, 440, 470 and 490 nm) at a specific power intensity (range from 2~20 mW/cm^2) as needed. No obvious difference when we compared the dark current which was measured before the light current to that measured after the light current for same device. For the dynamic response measurement, the anode and cathode of the device were connected to a 1 GΩ load resistor and a digital oscilloscope (Iwatsu Electric Co., Ltd, DS-5624A) combined with an optical chopper (#55-783, Edmund Optics). The dynamic response displayed on the oscilloscope and the response time was extracted according to the record. All the device measurements were conducted in air and at room temperature.

4.3 Result and discussion

A schematic illustration of the synthesis of $Cs_2AgBiCl_6$ nanocrystals is shown in **Scheme 4.1**. **Figure 4.1(a)** shows the X-ray diffraction (XRD) patterns of $Cs_2AgBiCl_6$ and $Cs_2AgBiBr_6$ NCs. The presence of multiple diffraction peaks exhibits the structural

characteristics of the nanocrystals. For $Cs_2AgBiCl_6$ NCs, domain diffraction peaks at 23.28°, 33.21°, 40.96°, and 47.64° are assigned to (022), (004), (224) and (044) diffraction planes of standard cubic double perovskite structure with a space group of Fm-3m and a lattice parameter of 10.78 Å. Other peaks are consistent with the simulated values of $Cs_2AgBiCl_6$_11523 in the literature, [40] confirming the formation of double perovskite structure via the modified hot-injection method. For $Cs_2AgBiBr_6$ NCs, domain diffraction peaks at 15.49°, 22.06°, 27.32°, 31.60°, 39.00°, and 45.32° are assigned to (002), (022), (222), (004), (224) and (044) diffraction planes of standard cubic double perovskite structure with a space group of Fm-3m and a lattice parameter of 11.31 Å. All of the diffraction peaks are consistent with the $Cs_2AgBiBr_6$_18989 in the literature. [41] The XRD results indicate that the diffraction pattern of $Cs_2AgBiBr_6$ NCs shifts to a smaller angle compared to $Cs_2AgBiCl_6$ NCs, wherein the lattice expansion is resulted from the larger ionic radius of Br- (1.96 Å) compared to Cl^- (1.81 Å). The transmission electron microscopy (TEM) images of $Cs_2AgBiCl_6$ and $Cs_2AgBiBr_6$ NCs are supplied in **Figure 4.1(b)-(c)**, the average sizes are 10.83 ± 3.60 nm and 9.88 ± 2.40 nm for $Cs_2AgBiCl_6$ and $Cs_2AgBiBr_6$ NCs, respectively. The inset shows the high-resolution TEM images, it can be seen that the interplanar spacing of (022) is consistent with the XRD results which indicate the lattice expansion when the halide ion in double perovskite changed from Cl^- to Br^-.

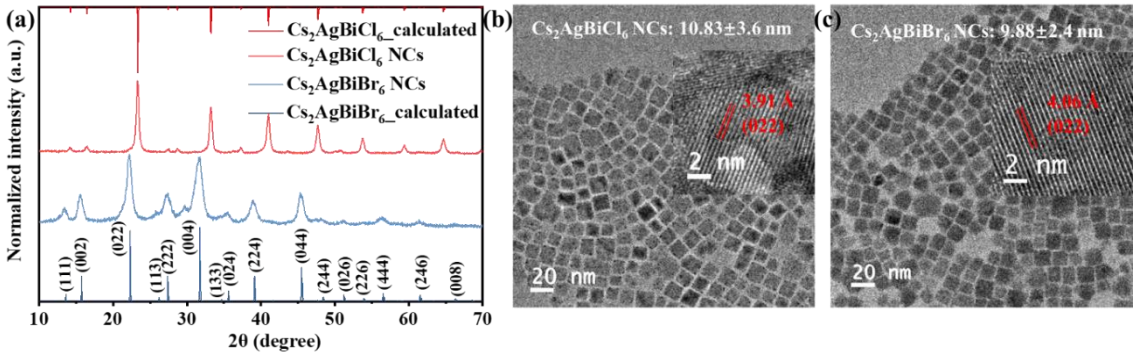

Figure 4.1 (a) X-ray diffraction (XRD) pattern of $Cs_2AgBiCl_6$ and $Cs_2AgBiBr_6$ nanocrystals. TEM images of (b) $Cs_2AgBiCl_6$ NCs and (c) $Cs_2AgBiBr_6$ NCs. The inset figures are high-resolution TEM images that show the lattice distance of the nanocrystals.

Quantitative analysis of the electronic structures and chemical properties of $Cs_2AgBiCl_6$ and $Cs_2AgBiBr_6$ NCs has been performed by the combination of XPS and STEM-EDS analysis, and the binding energies of XPS spectra were calculated after calibrating the shift in the binding energy of C 1s edge as the reference. **Figure 4.2** illustrates the survey and narrow scan XPS spectra of NCs, red line and blue line represent $Cs_2AgBiCl_6$ and $Cs_2AgBiBr_6$ NCs, respectively. **Figure 4.2(a)** confirms the elemental composition of $Cs_2AgBiCl_6$ with the presence of peaks of Cs, Ag, Bi, Cl, and $Cs_2AgBiBr_6$ NCs with the presence of peaks of Cs, Ag, Bi, and Br. In the case of $Cs_2AgBiCl_6$ NCs, the Cs 3d doublet peaks for $Cs_2AgBiCl_6$ NCs detected at 738.0 eV (Cs $3d_{3/2}$) and 724.0 eV (Cs $3d_{5/2}$) correspond to the standard Cs element, as shown in **Figure 4.2(b)**. The two peaks were disjoint with an energy value of 14 eV. **Figure 4.2(c)** exhibits the Ag 3d XPS spectra of $Cs_2AgBiCl_6$ NCs with peaks at 373.8 eV (Ag $3d_{3/2}$) and 367.8 eV (Ag $3d_{5/2}$) associated with the +1 oxidation state of Ag. The two peaks have an energy difference of 6 eV. The Bi $4f_{5/2}$ and Bi $4f_{7/2}$ peaks were located at 164.5 eV and 159.1 eV, as seen in **Figure 4.2(d)**. Additional Bi peaks with lower binding energy were observed at 161.6 eV and 156.5 eV corresponding to the low valence state $Bi^{(3-x)+}$, suggesting the formation of chlorine vacancies. [42] At the binding energy of 199.1 eV and 197.6 eV, the Cl 2p peak can be divided into two peaks originating from Cl $2p_{1/2}$ and Cl $2p_{3/2}$, respectively (**Figure 4.2 (e)**). In the case of $Cs_2AgBiBr_6$ NCs, **Figure 4.2(f)** shows the Br 3d doublet peaks at 68.9 eV and 68.0 eV which are attributed to Br $3d_{3/2}$ and Br $3d_{5/2}$, respectively. Compared $Cs_2AgBiBr_6$ to $Cs_2AgBiCl_6$, the peak of Cs 3d and Ag 3d shift 0.2 eV toward higher binding energy, while the shift of Bi 4f is smaller (0.15 eV), which indicates the X-Br (X = Cs, Ag, Bi) interactions in $Cs_2AgBiBr_6$ are stronger than the X-Cl (X = Cs, Ag, Bi) interactions in $Cs_2AgBiCl_6$, meanwhile, the Bi-Cl interactions are weaker than Cs-Cl and Ag-Cl.

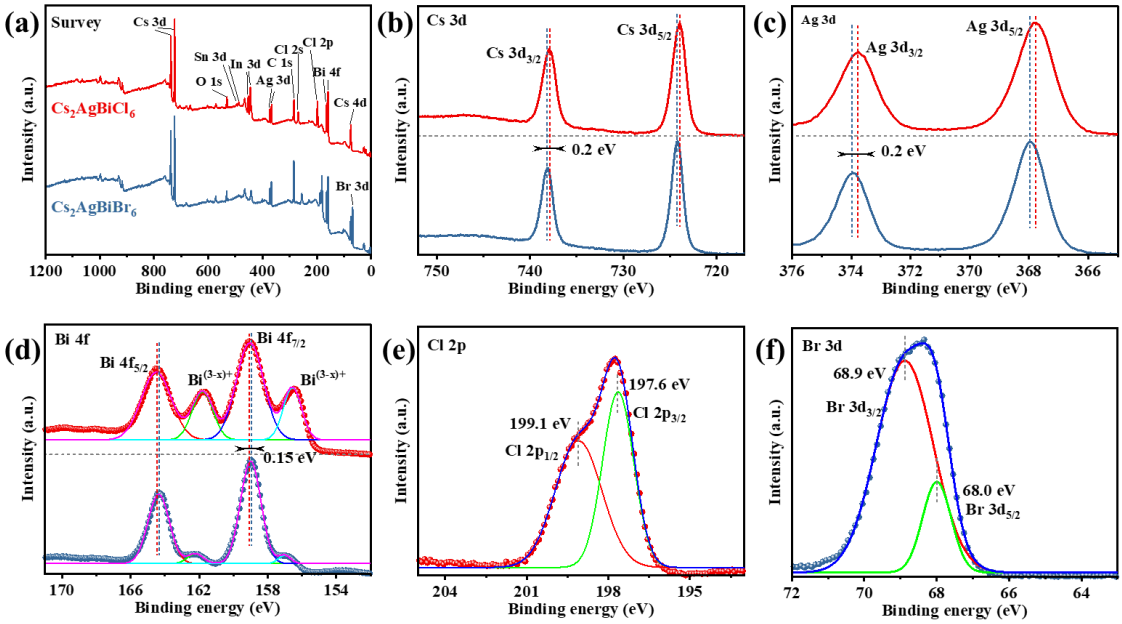

Figure 4.2 XPS spectra of (a) wide scan, (b) Cs 3d, (c) Ag 3d, (d) Bi 4f, (e) Cl 2p, (f) Br 3d core level obtained for $Cs_2AgBiCl_6$ (red line/scatter) and $Cs_2AgBiBr_6$ (blue line/scatter) NCs. All the spectra are calibrated to 284.8 eV, corresponding to a C 1s peak.

The ultraviolet-visible (UV-Vis) spectroscopy was utilized to evaluate the optical properties and light absorption capability of the $Cs_2AgBiCl_6$ and $Cs_2AgBiBr_6$ NCs as shown in **Figure 4.3(a)**. The absorption peaks account for the effective absorption of photons, which is potential for the capture of photocurrents of the photodiodes based on NCs. The sharp absorption peaks at around 368 nm and 425 nm are originated from the hybrid orbital of Bi 6s/Ag 4d defect level. [43] The optical bandgaps were estimated from the absorption spectra by using Tauc's plot method, [44,45] as shown in the inset of **Figure 4.3(a)**, red and blue dash lines are the tangent lines of the $(\alpha h\nu)1/n$, where α is the absorption coefficient, h is Plank's constant, ν is the frequency of light, and the index n = 2 is related to the bandgap of indirect allowed transition semiconductors. The estimated bandgaps of the $Cs_2AgBiCl_6$ and $Cs_2AgBiBr_6$ NCs are 3.17 eV and 2.66 eV, respectively. In order to obtain information on the energy band for further application, the valence band minimum (VBM) and conduction band maximum (CBM) of the NCs were determined by using ultraviolet photoelectron spectroscopy (UPS). The energy

level of $Cs_2AgBiCl_6$ NCs are -2.52 ~ -5.69 eV, and that of $Cs_2AgBiBr_6$ NCs is -3.55 ~ -6.21 eV, as shown in **Figure 4.3(c)**.

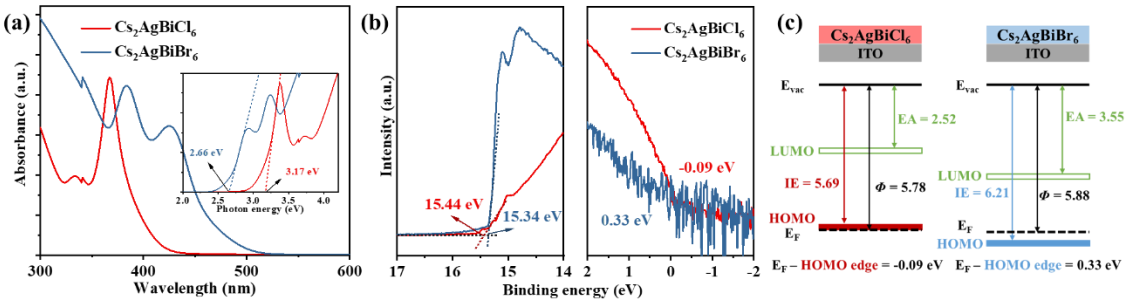

Figure 4.3 (a) UV-Vis spectra and Tauc plot of $Cs_2AgBiCl_6$ and $Cs_2AgBiBr_6$ NCs. (b) UPS spectra of $Cs_2AgBiCl_6$ and $Cs_2AgBiBr_6$ thin film. The left shows the cutoff of energy, and the right figure shows the enlarged spectral parts near the Fermi edge. (c) Energy level diagrams showing the results for $Cs_2AgBiCl_6$ and $Cs_2AgBiBr_6$ NCs on an ITO substrate. All energy values are scaled to eVs, EA: electron affinity, IE: ionization energy, EF: fermi level, Φ: work function.

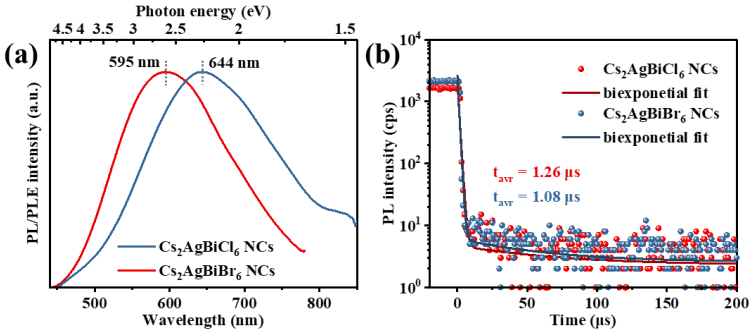

Figure 4.4 (a) Photoluminescence (PL) spectra of $Cs_2AgBiCl_6$ and $Cs_2AgBiBr_6$ NCs thin film. The optimal excitation wavelength for both samples is 404 nm. (b) PL decay of $Cs_2AgBiCl_6$ and $Cs_2AgBiBr_6$ NCs thin film.

Table 4.1 Decay parameters of $Cs_2AgBiCl_6$ and $Cs_2AgBiBr_6$ NCs at room temperature [a]

Sample	τ_1 (a_1)	τ_2 (a_2)	τ_{avg}	R-square
$Cs_2AgBiCl_6$	1.19 μs (94.27%)	62.30 μs (5.73%)	1.26 μs	0.992
$Cs_2AgBiBr_6$	1.01 μs (93.38%)	53.34 μs (6.62%)	1.08 μs	0.992

[a]PL lifetime was biexponential fitted by the following formula:

$$I(t) = A_1 e^{-t/\tau_1} + A_2 e^{-t/\tau_2}$$

where *t* indicates time, *I(t)* is the PL intensity at *t* μs, A_1 and A_2 are the amplitude of component 1 and 2, τ_1 and τ_2 are the lifetime of component 1 and 2. a_1 and a_2 are the fractional for component 1 and 2, which are calculated by $a = \frac{A_i\tau_i}{\sum A_i\tau_i}$; τ_{avg} indicates the amplitude average lifetime, which is calculated by $\tau_{ave} = A_1\tau_1 + A_2\tau_2$.

To examine the optoelectronic properties of photodiodes based on $Cs_2AgBiCl_6$ and $Cs_2AgBiCl_6$ NCs in our work, devices based on $Cs_2AgBiCl_6$, $Cs_2AgBiBr_6$, $Cs_2AgBiCl_6$/PCBM were fabricated and their photo-response were measured using the same procedure. **Figure 4.5(a)-(b)** showed the device configuration and schematic diagram of energy level of photodiodes based on $Cs_2AgBiCl_6$ NCs. Electrons and holes as separated charge carriers are promoted by built-in electric field offered by the energy difference between the functional layers. **Figure 4.5(c)** are the photocurrent curves of PDs when the devices were under 310, 340, 365 and 380 nm illumination. The optimal photocurrent was obtained by 365 nm illumination and photocurrent were the lowest under 310 nm illumination. The photocurrent difference between 385, and 505 nm is owing to the absorbance difference between two wavelengths as shown in **Figure 4.3(a)**. For the $Cs_2AgBiCl_6$ NCs-based PD, the photocurrent under zero bias is around two magnitudes larger than the dark current under the 365 nm illumination. As the

typical figure-of-merits, responsivity (R) and specific detectivity (D^*) identify the ability of a photodetector responding to a light radiation, and which level of light intensity can be detected, respectively. [46] R is expressed by $R = (I_{light} - I_{dark})/P_{in}$, where P_{in} represents the incident light power. [47,48] Detectivities were calculated on account of measured photocurrent, dark current, and incident light intensity which extracted from the equation $D^* = R_\lambda(S/(2qI_{dark}))^{1/2}$, where R_λ is the responsivity at a specific wavelength, the absolute charge value of electron is q, and S represents the effective irradiation area. [49] As shown in **Figure 4.5(e)-(f)**, R_A and D^* of PD were achieved, it showed 0.22 mA/W of responsivity and 1.7×10^9 Jones of detectivity under 365 nm illumination at zero bias.

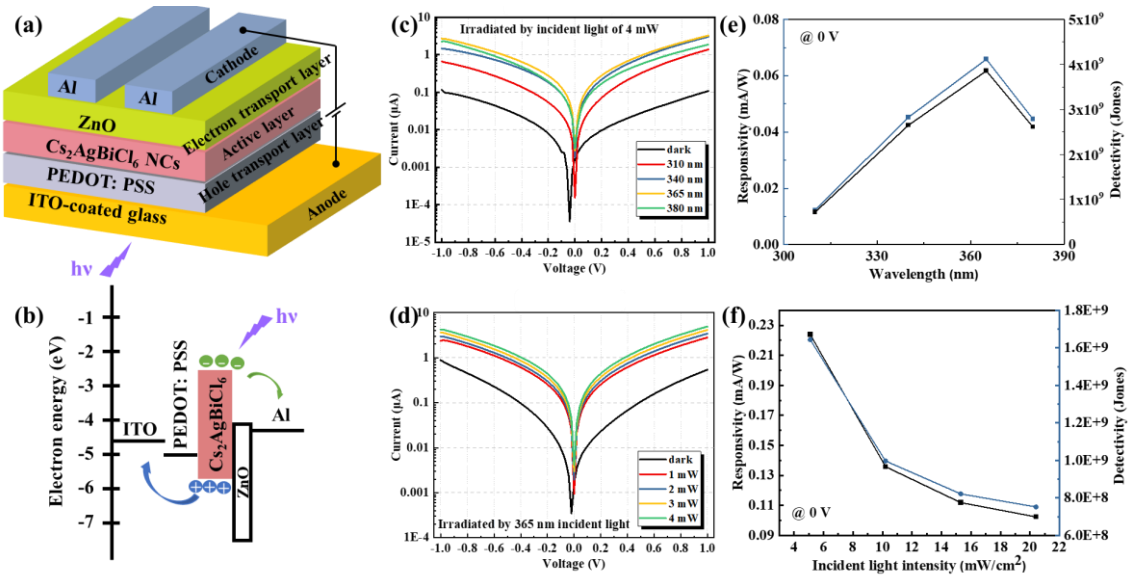

Figure 4.5 (a) Device configuration of photodiodes based on $Cs_2AgBiCl_6$ NCs. (b) The energy level which is corresponding to the device structure. The green and blue arrows indicate the moving direction of electron and hole, respectively. (c) Current versus applied voltage of photodiodes irradiated by incident light with different wavelength. (d) Current versus applied voltage of photodiodes irradiated by 365 nm incident light with different power intensities. (e) Responsivity and detectivity versus the wavelength of incident light under zero bias. (f) Responsivity and detectivity versus incident light intensity of photodiode at zero bias under 365 nm illumination.

The wavelength dependent time-resolved response characters as shown in **Figure 4.6**, which indicates on/off switched properties under radiation of 310, 340, 365 and 380 nm, respectively, at zero bias (a) and 0.5 V bias (b). Rise and decay times are regarded as the period time for dark current increase to the 90% of the maximal photocurrent and photocurrent drop to 10% of the maximal value. The response speed of device shows 25 ms and 25 ms of rise and decay time, respectively.

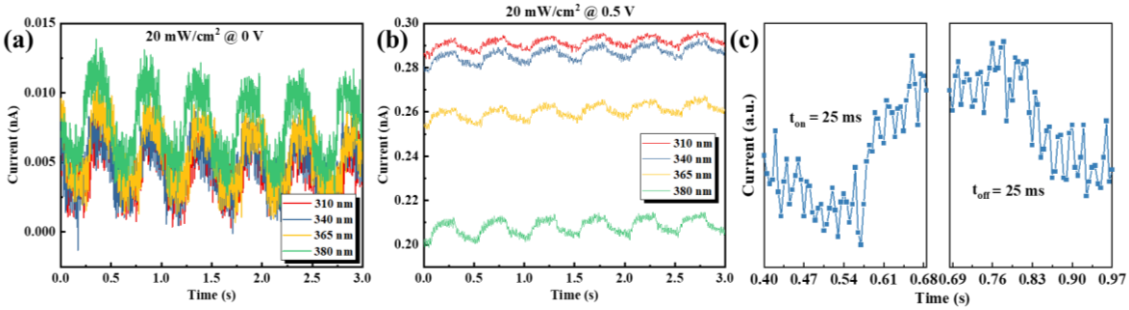

Figure 4.6 Dynamic current-time response of the photodiode under zero bias (a) and 0.5 V (b). (c) Enlarged spectra of the rise time and fall time of the photodiode under the illumination of 365 nm.

When the active layer changed from $Cs_2AgBiCl_6$ NCs to $Cs_2AgBiBr_6$ NCs, the device exhibits different performance. **Figure 4.7(a)-(b)** showed the device configuration and schematic diagram of energy level of photodiodes based on $Cs_2AgBiBr_6$ NCs. **Figure 4.7(c)** are the photocurrent curves of PDs when the devices were under 310, 340, 365, 380, 410, 440, 470, and 490 nm illumination. The optimal photocurrent was obtained by 365 nm illumination and photocurrent were the lowest under 490 nm illumination. The photocurrent difference between 365, and 490 nm is owing to the absorbance difference between two wavelengths as shown in **Figure 4.3(a)**. For the $Cs_2AgBiBr_6$ NCs-based PD, the photocurrent under zero bias is around 50 time larger than the dark current under the 365 nm illumination. As shown in **Figure 4.7(e)-(f)**, R and D^* of PD were achieved, it showed 0.27 mA/W of responsivity and 9.94×10^9 Jones of detectivity under 380 nm illumination at zero bias, both of them are higher than those of $Cs_2AgBiCl_6$ NCs-based PD, which could be attributed to the less

vacancy defect of $Cs_2AgBiBr_6$ NCs and more efficient separation of electron-hole pairs.

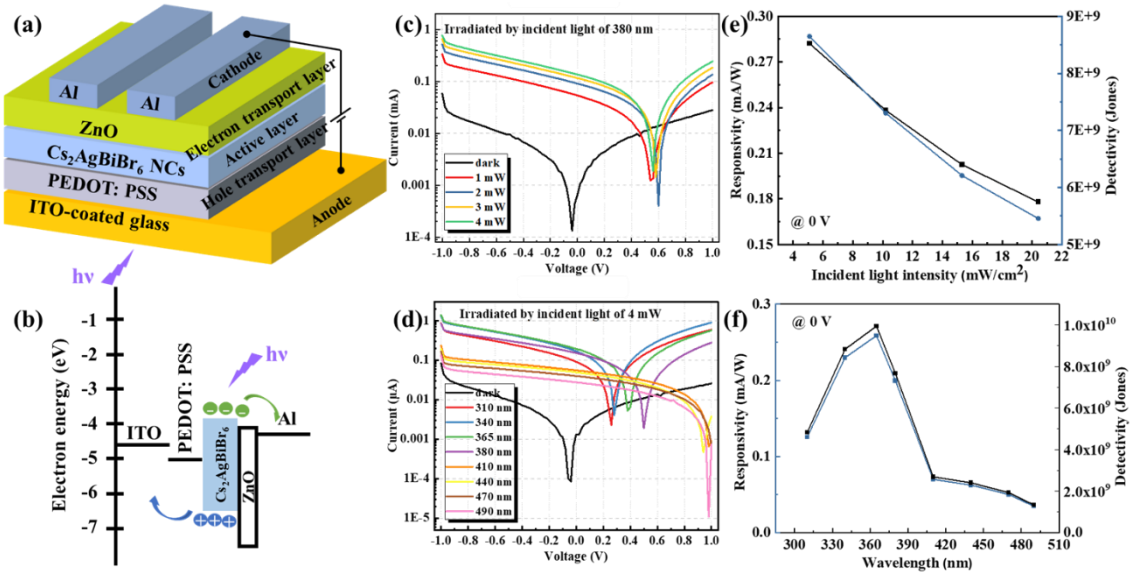

Figure 4.7 (a) Device configuration of photodiodes based on $Cs_2AgBiBr_6$ NCs. (b) The energy level which is corresponding to the device structure. (c) Current versus applied voltage of photodiodes irradiated by 380 nm incident light with different power intensities. (d) Current versus applied voltage of photodiodes irradiated by incident light with different wavelength. (e) Responsivity and detectivity versus incident light intensity of photodiode under zero bias. (f) Responsivity and detectivity versus the wavelength of incident light under zero bias.

The wavelength dependent time-resolved response characters as shown in **Figure 4.8(a)**, which indicates on/off switched properties under radiation of 310, 340, 365, 380, 410, 440, 470 and 490 nm, respectively, at zero bias. The wavelength-dependent response is consistent with the result shown in **Figure 4.8(f)**. **Figure 4.8(c)** exhibits on/off switched properties under radiation of 380 nm with different power intensity under zero bias. The response rise and decay times of device are 50 ms and 45 ms, respectively.

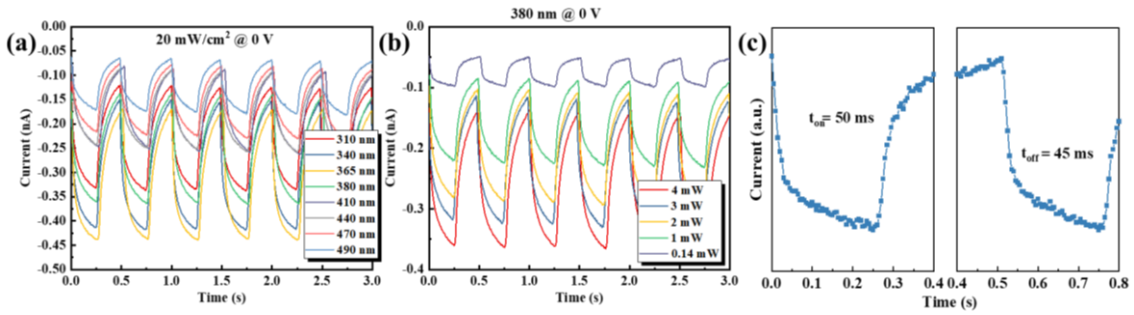

Figure 4.8 (a) Dynamic current-time response of the photodiode under zero bias irradiated by the incident light with different wavelength. (b) Dynamic current-time response of the photodiode under zero bias irradiated by the 380 nm light with different power intensity. (c) Enlarged spectra of the rise time and fall time of the photodiode irradiated by the 0.14 mW of 380 nm light measured under zero bias.

Although the responsivity and detectivity $Cs_2AgBiBr_6$ NCs-based PD was better than that of $Cs_2AgBiCl_6$ NCs-based PD, the response time is slower. Generally, the NCs/NPs has the potential of quenching resulted from the interface defects, thus generating the trap which capture the carriers and slow the response. Interface engineering is an effective tool to modify the interface and enhance the carrier transport efficient. Here the PCBM was used as an interface modifier, [50] which is inserted into $Cs_2AgBiBr_6$ NCs/ZnO interface and enhance the device performance. **Figure 4.9(a)-(b)** showed the device configuration and schematic diagram of energy level of photodiodes based on $Cs_2AgBiBr_6$ NCs/PCBM. **Figure 4.9(c)** are the photocurrent curves of PDs when the devices were under 310, 340, 365, 380, 410, 440, 470, and 490 nm illumination. For the PCBM-modified PD, the photocurrent under zero bias is around 150 time larger than the dark current under the 365 nm illumination. As shown in **Figure 4.9(e)-(f)**, 3.21 mA/W of responsivity and 8.91×10^{10} Jones of detectivity under 340 nm illumination at zero bias, both of them are much higher than those of non-modified $Cs_2AgBiBr_6$ NCs-based PD, which could be attributed to the better $Cs_2AgBiBr_6$/ZnO interface.

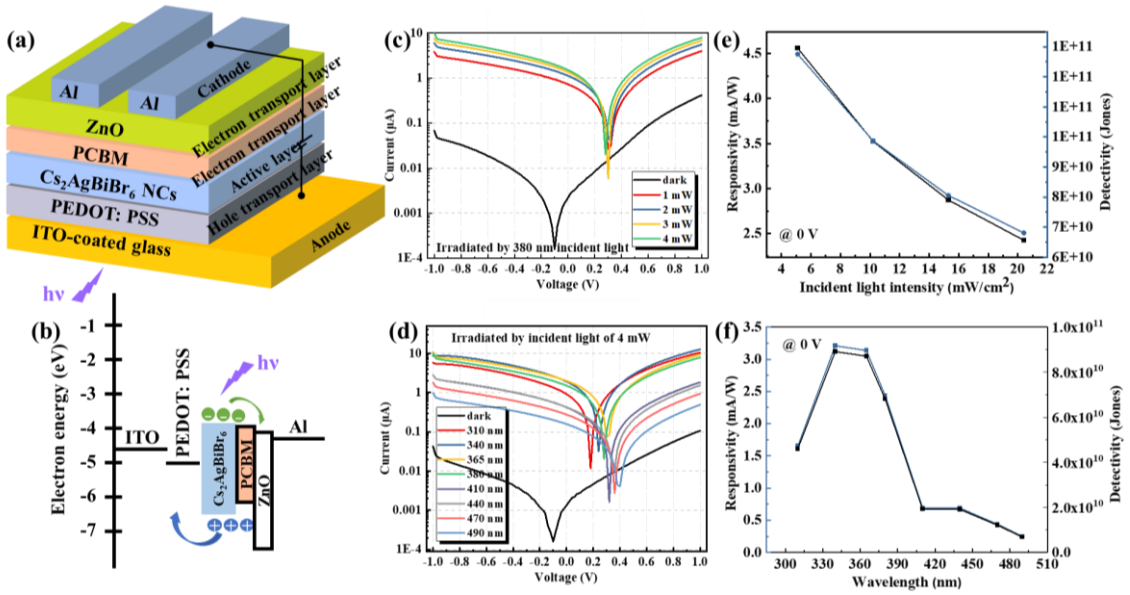

Figure 4.9 (a) Device configuration of photodiodes based on $Cs_2AgBiBr_6$ NCs with PCBM inserting layer. (b) The energy level which is corresponding to the device structure. (c) Current versus applied voltage of photodiodes irradiated by 380 nm incident light with different power intensities. (d) Current versus applied voltage of photodiodes irradiated by 4 mW incident light with different wavelength. (e) Responsivity and detectivity versus incident light intensity of photodiode under zero bias. (f) Responsivity and detectivity versus the wavelength of incident light under zero bias.

Figure 4.10(a) exhibited the dynamic responses, which indicates on/off switched properties under radiation of 310, 340, 365, 380, 410, 440, 470 and 490 nm, respectively, at zero bias. The wavelength-dependent response is consistent with the result shown in **Figure 4.10(f)**. **Figure 4.10(c)** exhibits on/off switched properties under radiation of 380 nm with different power intensity under zero bias. The response rise and decay times of device are 30 ms and 35 ms, respectively, which are faster than non-modified PDs.

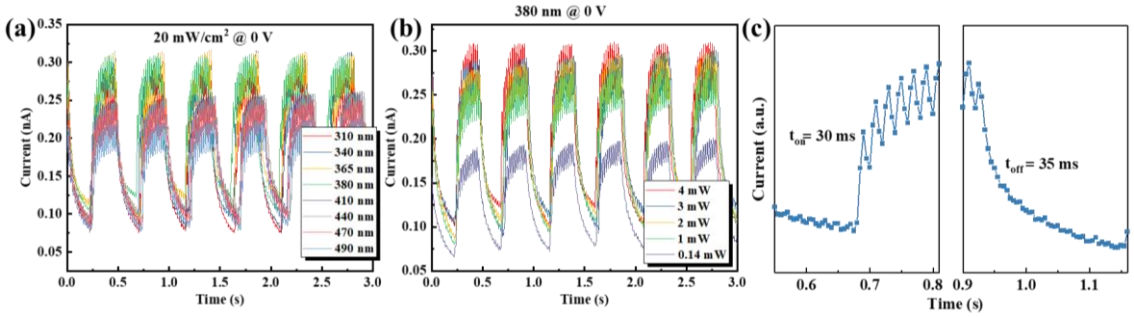

Figure 4.10 (a) Dynamic current-time response of the photodiode under zero bias irradiated by the incident light with different wavelength. (b) Dynamic current-time response of the photodiode under zero bias irradiated by the 380 nm light with different power intensity. (c) Enlarged spectra of the rise time and fall time of the photodiode irradiated by the 0.14 mW of 380 nm light measured under zero bias.

Table 4.2 Summary for the device performance of photodiodes with different structure.

Device structure	Response range (nm)	R (mA/W) @ 1 V	D* (Jones) @ 1 V	R (mA/W) @ 0 V	D* (Jones) @ 0 V	t_{rise} (ms)	t_{fall} (ms)
$Cs_2AgBiCl_6$/ZnO	310-380	3.84	4.12E9	0.07	3.86E9	25	25
$Cs_2AgBiBr_6$/ZnO	310-490	1.06	2.34E9	0.26	9.94E9	50	45
$Cs_2AgBiBr_6$/PCBM /ZnO	310-490	15.46	1.67E10	3.21	8.91E10	30	35

4.4 Conclusion

In summary, the photodiodes based on $Cs_2AgBiCl_6$ lead-free double perovskite NCs were prepared in our work which peculiarities proved to be promising by advantages of the simple composition engineering for halogen atoms to be replaced by the Br atoms from Cl atoms. The $Cs_2AgBiBr_6$ NCs with narrower bandgap were successfully synthesized which achieved the wavelength-selectivity when applied in photodiodes, additionally enhance the device performance. On the other hand, PCBM thin layer was

inserting as an electron transport layer, the optimized photodiode exhibited a good self-powered performance which acted as the responsivity of 3.1 mA/W when detectivity approached 8.91×10^{10} Jones, and a large light/dark current ratio near 200 was obtained. More importantly, spectral wavelength selectivity of $Cs_2AgBiBr_6$ NCs-based photodetector manifested the potential utilization in ultraviolet detecting, which point out potential application of lead-free double perovskite nanocrystals in next-generation photodiodes.

Reference

1. Dou, L. *et al.* Solution-processed hybrid perovskite photodetectors with high detectivity. *Nat. Commun.* **5**, 5404 (2014).
2. Zhang, W., Eperon, G. E. & Snaith, H. J. Metal halide perovskites for energy applications. *Nat. Energy* **1**, 16048 (2016).
3. Chen, Q. *et al.* Planar Heterojunction Perovskite Solar Cells via Vapor-Assisted Solution Process. *J. Am. Chem. Soc.* **136**, 622–625 (2014).
4. Li, X. *et al.* A vacuum flash–assisted solution process for high-efficiency large-area perovskite solar cells. *Science (80-.).* **353**, 58–62 (2016).
5. Leung, S.-F. *et al.* A Self-Powered and Flexible Organometallic Halide Perovskite Photodetector with Very High Detectivity. *Adv. Mater.* **30**, 1704611 (2018).
6. Stranks, S. D. *et al.* Electron-Hole Diffusion Lengths Exceeding 1 Micrometer in an Organometal Trihalide Perovskite Absorber. *Science (80-.).* **342**, 341–344 (2013).
7. De Roo, J. *et al.* Highly Dynamic Ligand Binding and Light Absorption Coefficient of Cesium Lead Bromide Perovskite Nanocrystals. *ACS Nano* **10**, 2071–2081 (2016).
8. Shi, D. *et al.* Low trap-state density and long carrier diffusion in organolead trihalide perovskite single crystals. *Science (80-.).* **347**, 519–522 (2015).

9. Lin, Q., Armin, A., Lyons, D. M., Burn, P. L. & Meredith, P. Low Noise, IR-Blind Organohalide Perovskite Photodiodes for Visible Light Detection and Imaging. *Adv. Mater.* **27**, 2060–2064 (2015).
10. Zhumekenov, A. A. *et al.* Formamidinium Lead Halide Perovskite Crystals with Unprecedented Long Carrier Dynamics and Diffusion Length. *ACS Energy Lett.* **1**, 32–37 (2016).
11. Wang, M., Zeng, P., Wang, Z. & Liu, M. Vapor-Deposited Cs2AgBiCl6 Double Perovskite Films toward Highly Selective and Stable Ultraviolet Photodetector. *Adv. Sci.* **7**, 1903662 (2020).
12. Lei, H., Hardy, D. & Gao, F. Lead-Free Double Perovskite Cs2AgBiBr6: Fundamentals, Applications, and Perspectives. *Adv. Funct. Mater.* **31**, 2105898 (2021).
13. Volonakis, G. *et al.* Cs2InAgCl6: A New Lead-Free Halide Double Perovskite with Direct Band Gap. *J. Phys. Chem. Lett.* **8**, 772–778 (2017).
14. Zhou, J., Rong, X., Molokeev, M. S., Zhang, X. & Xia, Z. Exploring the transposition effects on the electronic and optical properties of Cs2AgSbCl6via a combined computational-experimental approach. *J. Mater. Chem. A* **6**, 2346–2352 (2018).
15. Filip, M. R. & Giustino, F. Computational Screening of Homovalent Lead Substitution in Organic–Inorganic Halide Perovskites. *J. Phys. Chem. C* **120**, 166–173 (2016).
16. Zhao, X.-G. *et al.* Design of Lead-Free Inorganic Halide Perovskites for Solar Cells via Cation-Transmutation. *J. Am. Chem. Soc.* **139**, 2630–2638 (2017).
17. Yan, D.-N. *et al.* Theoretical prediction of double perovskite Cs2AgxCu1-xInyTb1-yCl6 for infrared detection. *J. Phys. D. Appl. Phys.* **53**, 265302 (2020).
18. Lamba, R. S., Basera, P., Singh, S., Bhattacharya, S. & Sapra, S. Lead-Free Alloyed Double-Perovskite Nanocrystals of Cs2(NaxAg1–x)BiBr6 with Tunable Band Gap. *J. Phys. Chem. C* **125**, 1954–1962 (2021).

19. Ning, W. *et al.* Long Electron–Hole Diffusion Length in High-Quality Lead-Free Double Perovskite Films. *Adv. Mater.* **30**, 1706246 (2018).
20. Zheng, Y. *et al.* A facile fabrication of lead-free Cs2NaBiI6 double perovskite films for memory device application. *J. Alloys Compd.* **909**, 164613 (2022).
21. Soni, A., Bhamu, K. C. & Sahariya, J. Investigating effect of strain on electronic and optical properties of lead free double perovskite Cs2AgInCl6 solar cell compound: A first principle calculation. *J. Alloys Compd.* **817**, 152758 (2020).
22. Mo, Q. *et al.* Highly Efficient and Ultra-Broadband Yellow Emission of Lead-Free Antimony Halide toward White Light-Emitting Diodes and Visible Light Communication. *Laser Photon. Rev.* **16**, 2100600 (2022).
23. Yang, X., Wang, W., Ran, R., Zhou, W. & Shao, Z. Recent Advances in Cs2AgBiBr6-Based Halide Double Perovskites as Lead-Free and Inorganic Light Absorbers for Perovskite Solar Cells. *Energy & Fuels* **34**, 10513–10528 (2020).
24. Slavney, A. H., Hu, T., Lindenberg, A. M. & Karunadasa, H. I. A Bismuth-Halide Double Perovskite with Long Carrier Recombination Lifetime for Photovoltaic Applications. *J. Am. Chem. Soc.* **138**, 2138–2141 (2016).
25. Kentsch, R. *et al.* Exciton Dynamics and Electron–Phonon Coupling Affect the Photovoltaic Performance of the Cs2AgBiBr6 Double Perovskite. *J. Phys. Chem. C* **122**, 25940–25947 (2018).
26. Biega, R.-I., Filip, M. R., Leppert, L. & Neaton, J. B. Chemically Localized Resonant Excitons in Silver–Pnictogen Halide Double Perovskites. *J. Phys. Chem. Lett.* **12**, 2057–2063 (2021).
27. Lan, Z. *et al.* Dual-Band Organic Photodetectors for Dual-Channel Optical Communications. *Laser Photon. Rev.* **16**, 2100602 (2022).
28. Yan, G. *et al.* Alkali metal ions induced high-quality all-inorganic Cs2AgBiBr6 perovskite films for flexible self-powered photodetectors. *Appl. Surf. Sci.* **579**, 152198 (2022).
29. Elsinger, L. *et al.* Waveguide-Coupled Colloidal Quantum Dot Light Emitting

Diodes and Detectors on a Silicon Nitride Platform. *Laser Photon. Rev.* **15**, 2000230 (2021).

30. Zhang, J. *et al.* Low-temperature preparation achieving 10.95%-efficiency of hole-free and carbon-based all-inorganic CsPbI3 perovskite solar cells. *J. Alloys Compd.* **862**, 158454 (2021).
31. Sivashanmugan, K., Lin, C.-H., Hsu, S.-H., Guo, T.-F. & Wen, T.-C. Interfacial engineering of ZnO surface modified with poly-vinylpyrrolidone and p-aminobenzoic acid for high-performance perovskite solar cells. *Mater. Chem. Phys.* **219**, 90–95 (2018).
32. Ruankham, P. *et al.* Full coverage of perovskite layer onto ZnO nanorods via a modified sequential two-step deposition method for efficiency enhancement in perovskite solar cells. *Appl. Surf. Sci.* **410**, 393–400 (2017).
33. Lee, H.-J. & Na, S.-I. Investigation of PCBM/ZnO and C60/BCP-based electron transport layer for high-performance p-i-n perovskite solar cells. *J. Alloys Compd.* **921**, 166007 (2022).
34. Liu, G. *et al.* Highly efficient and stable ZnO-based MA-free perovskite solar cells via overcoming interfacial mismatch and deprotonation reaction. *Chem. Eng. J.* **431**, 134235 (2022).
35. Noh, Y. W., Jin, I. S., Kim, K. S., Park, S. H. & Jung, J. W. Reduced energy loss in SnO2/ZnO bilayer electron transport layer-based perovskite solar cells for achieving high efficiencies in outdoor/indoor environments. *J. Mater. Chem. A* **8**, 17163–17173 (2020).
36. Ye, J. *et al.* Doped Bilayer Tin(IV) Oxide Electron Transport Layer for High Open-Circuit Voltage Planar Perovskite Solar Cells with Reduced Hysteresis. *Small* **17**, 2005671 (2021).
37. Huang, X., Matsushita, Y., Sun, H.-T. & Shirahata, N. Impact of bismuth-doping on enhanced radiative recombination in lead-free double-perovskite nanocrystals. *Nanoscale Adv.* **4**, 3091–3100 (2022).

Interfaces **12**, 47714–47720 (2020).

50. Hewlett, R. M. & McLachlan, M. A. Surface Structure Modification of ZnO and the Impact on Electronic Properties. *Adv. Mater.* **28**, 3893–3921 (2016).

Chapter 5 Conclusions and future prospects

5.1 General conclusions

Lead-free double perovskite nanocrystals (LDP NCs) are promising materials as an alternative to lead-based perovskite nanocrystals to solve the problem of toxicity and instability. Specifically, replacing two Pb^{2+} ions with a combination of monovalent and trivalent cations could be a solution for forming three-dimensional (3D) perovskite structures, whose chemical formula is $A_2B(I)B(III)X_6$, which is called double-perovskite structure. LDP NCs have excellent properties such as good stability, long carrier lifetime, long photoluminescence lifetimes, high photoluminescence quantum yield and solution-processability. Therefore, LDP NCs are considered to be promising materials for optoelectronic applications including photodetector, photocatalysts, light-emitting diodes and solar cells.

$Cs_2AgB'X_6$ (B' = In or Bi, X = Cl or Br) has the potential to be applied in optoelectronic devices. While it owns a high absorption coefficient, good stability and low toxicity, there is still a challenge in improving its performance to reach or exceed that of lead-based perovskites. For example, the defects introduced by indium can create trap states in the bandgap of $Cs_2AgInCl_6$ thus affecting the material properties. Therefore, the thesis focuses on the composition tuning of LDP NCs for photodiode application by B-site doping strategies as well as the bandgap engineering by X-site anion composition tuning in LDP NCs to realize efficient wavelength-selective photodiodes.

In Chapter 1, a general background about lead-free double perovskites and a simple overview of ultraviolet photodiodes are introduced. In particular, the process and purpose of the research which lead to the conception of the research topic were clarified.

In Chapter 2, Na-alloyment and Bi-doping were employed in improving the optical properties of $Cs_2AgInCl_6$ NCs. We synthesized $Cs_2Ag_{0.65}Na_{0.35}InCl_6$ NCs doped with bismuth (Bi^{3+}) ions and investigated their photophysical properties to reveal the role of

the dopant on the enhanced photoemission properties. Specifically, it was found that the photoluminescence quantum yield (PL QY) increased up to 33.2% by 2% Bi-doping. The optical bandgap of the NCs decreased from 3.47 eV to 3.41 eV as the amount of the dopant increased from 2% to 15%. To find out the effect of Bi-doping, the temperature-dependent PL properties of the undoped and doped NCs were investigated by utilizing steady-state and time-resolved PL spectroscopy. With increasing the temperature from 20 K to 300 K, the PL intensities of the doped NCs decreased slower than the undoped ones. The correlated average PL lifetimes of both the bismuth-doped and undoped NCs decreased with increasing temperature. The experimental results revealed that all the NC samples showed thermal quenching with the temperature increasing, and the PL quenching was suppressed in bismuth-doped NCs.

In Chapter 3, we first demonstrated the highly responsive lead-free perovskite photodiode based on $Cs_2Ag_{0.35}Na_{0.65}InCl_6$ nanocrystals. The composition tuning strategy is introduced to enhance the device performance of photodiodes. Employed with a device structure composed of ZnO: Al electron-transport layer and Poly[(9,9-dioctylfluorenyl-2,7-diyl)-co-(4,4'-(N-(4-sec-butylphenyl)diphenylamine)] (TFB) hole transport layer, lead-free perovskite nanocrystal photodiodes exhibit a high responsivity of 3.03 A/W and specific detectivity of 1.29 x 10^{11} Jones under the illumination of a 340 nm light source. Moreover, the ultraviolet (UV) photodiodes show good performance under the self-powered mode, which exhibits a responsivity of 0.07 A/W and specific detectivity of 5.04 x 10^{10} Jones. Our work verifies the great potential of the $Cs_2Ag_{0.35}Na_{0.65}InCl_6$ nanocrystals in the application of environmentally friendly and high-performance UV photodiodes.

In Chapter 4, we studied on Cs_2AgBiX_6 (X = Cl or Br) NCs, which replaces In^{3+} by Bi^{3+} to avoid the generation of indium-caused defects and obtain strong absorption for the photodiode application. The band gap engineering was conducted through the composition tuning from $Cs_2AgBiCl_6$ to $Cs_2AgBiBr_6$. We fabricated lead-free double perovskite photodiodes with wavelength-selective properties response to UV-Visible

range. Specifically, the $Cs_2AgBiBr_6$-based photodiode exhibits a characteristic detection peak at 340 nm with a responsivity of 3.21 mA/W, a specific detectivity up to 8.91 x 10^{10} Jones and a fast response speed with rise/fall time of 30/35 ms. The excellent performance of self-driven photodiodes lights up the prospect of lead-free double perovskite nanocrystals in highly efficient optoelectronic devices without external power sources.

5.2 Future prospects

Although self-powered UV PDs with good performance were achieved, there is a long way for the double perovskite NCs to compete with the high-performing conventional lead halide perovskite in terms of optoelectronic performances. The possible way could be the trap passivation and interface engineering and synthesis and doping of new double perovskite with high photoelectric conversion efficiency. Most of the reports are small area SCs based, the reports related to NCs-based PD are very few. The large area fabrication of double perovskite NCs by noble methods is highly desirable for UV range response. Given the pace of development in the field, we are very much optimistic that the current advancements will encourage us to develop better double perovskite nanocrystals with suitable optoelectronic properties for the possible alternative of lead-based perovskite devices.

Acknowledgements

When I suddenly found the cherry blossoms had withered again, three years and nine months had already gone. The experience of Ph.D. study will be one of the most valuable and meaningful pieces in my life. I am truly grateful to have had this opportunity to embark on this journey at Hokkaido University and NIMS in Japan, and I would like to take this moment to acknowledge all those who have played a pivotal role in making this a reality.

First and foremost, I would like to express my sincere gratitude to my supervisor Prof. Dr. Naoto Shirahata for his instruction, encouragement and patience during my studies, and also for his help with my dissertation work. I am honored to have this opportunity to do the Ph.D. work in Nanoparticle group. During this period, Prof. Shirahata gave me lots of suggestions for scientific research. His support has been instrumental in shaping my academic journey. I hope to carry forward the lessons I have learned from my supervisor in my future endeavors.

I sincerely thank Prof. Kei Murakoshi, Prof. Tetsuo Uchikoshi, Prof. Yasuchika Hasegawa and Prof. Masaki Matsui as examiners of my dissertation. They put forward many valuable suggestions and comments, which enabled me to demonstrate and expound my conclusions and viewpoints from a deeper perspective, thus adding a lot of color to my dissertation.

I would also like to extend my heartfelt thanks to Dr. Hong-Tao Sun in our group. Dr. Sun not only gave me important instructions in the research work and taught me how to be more skilled at experiments, but also concerned about my life. He taught me how to think independently. His enthusiasm for science will inspire me in my future work in science research.

Next, I would like to express my grateful thanks to Dr. Bloyet Clarisse Florence, Dr. Ozbilgin Irem Nur Gamze, Dr. Kazuhiro Nemoto and Dr. Hiroyuki Yamada for their

training and help when I join this group. That really means a lot to me. I would also like to extend my gratitude to the former and current members in our group: Mr. Subhashri Chatterjee, Mr. Jiakai Chen, Mr. Binbin Zhang, Mr. Junpei Watanabe, Mr. Cong Zhang, Ms. Masami Soga, Ms. Fumie Takazawa, and Dr. Shilaj Roy. Thank you for your support and help along the way, and wish them all a bright future.

I am also indebted to my classmate and friend Dr. Sijie Li, who has been a constant source of support, inspiration and laughter throughout my Ph.D. journey. We travel, photograph, and experience countless things together. I would like to thank her for her unwavering support, her willingness to listen, and her ability to make me feel better especially on those tough days. I could not make it this far without her friendship.

Finally, I am forever grateful to my parents and sisters for their love, encouragement and support, especially my best Mr. Junjie Duan, for his unwavering emotional support for over nine years, enabling me to chase my dreams and achieve my goals.

Xiaoyu Huang

Tsukuba

March 2023